



PONTIFICIA UNIVERSIDAD CATOLICA DE CHILE
ESCUELA DE INGENIERIA

MULTI-PHYSICS MODEL OF A MAGNETO- RHEOLOGICAL DAMPER AND EXPERIMENTAL VALIDATION

ALAN PHILLIP STERNBERG CUNCHILLOS

Thesis submitted to the Office of Research and Graduate Studies in partial fulfillment of the requirements for the degree of Master of Science in Engineering

Advisor:

JUAN CARLOS DE LA LLERA

Santiago de Chile, April, 2011

© MMXI, Alan Sternberg



PONTIFICIA UNIVERSIDAD CATOLICA DE CHILE
ESCUELA DE INGENIERIA

MULTI-PHYSICS MODEL OF A MAGNETO- RHEOLOGICAL DAMPER AND EXPERIMENTAL VALIDATION

ALAN PHILLIP STERNBERG CUNCHILLOS

Members of the Committee:

JUAN CARLOS DE LA LLERA

JOSÉ FRANCISCO MUÑOZ

MATÍAS HUBE

EDUARDO IZQUIERDO

Thesis submitted to the Office of Research and Graduate Studies in partial fulfillment of the requirements for the Degree of Master of Science in Engineering

Santiago de Chile, April, 2011

© MMXI, Alan Sternberg

(To my family, for their constant support)

ACKNOWLEDGEMENTS

First of all I would like to gratefully thank my family for being always there to give me support and comprehension. It would not have been possible to keep going during all the undergraduate and graduate programs without their invaluable company.

I would also like to acknowledge my advisor, Juan Carlos de la Llera for his help, advices, trust and confidence in my work, which allowed me to successfully finish this research.

I want to give also recognition to Rene Zemp, Claudio Frings, André Coté and Eduardo Izquierdo, whose help was very valuable in the process of my research., specially by proposing solutions to the issues I had to face all along the thesis.

I would also like to thank VULCO and its financial help through the WEIR-VULCO scholarship, LORD Co. for their fluid donation, and REVESOL S.A. for helping me in the manufacture of the damper passing through all the problems that were appearing on the road.

I am also very grateful to Euge, José Tomás, and all my college friends who were always there for giving me a word of hope.

Finally, this research has been supported by the *Fondo Nacional de Ciencia y Tecnología*, Fondecyt, through Grant #1085282, and the *Fondo de Fomento al Desarrollo Científico y Tecnológico*, Fondef, through Grant #D07I1006.

TABLE OF CONTENTS

ACKNOWLEDGEMENTS	iii
ABSTRACT	xii
RESUMEN	xiii
1. INTRODUCTION	1
2. MULTIPHYSICS ANALYSYS OF A MAGNETO-RHEOLOGICAL DAMPER AND EXPERIMENTAL VALIDATION	4
3. CONCLUSIONS.....	33
REFERENCES	35
APPENDICES	37
Appendix I: Model of the MR-damper.....	38
Appendix II: MR-damper design.....	74
Appendix III: Parametric analyses	108

LIST OF TABLES

Table 1. Properties of Lord MRF 132DG fluid.....	9
Table 2. Field equations	12
Table 3. Summary of the comparative analyses	25
Table 4. Chosen parameters for the design of MRDA-UC	26
Table 5. Summary of the experimental tests performed to the real-scale MR-damper..	27
Table A.I 1. Error when predicting total force with respect to the refined <i>CFX</i> model.	63
Table A.I 2 Summary of physical and geometrical properties for heat transfer.	72
Table A.I 3. Results of pressure raise estimation	73
Table A.II 1. Typical properties of Lord MRF-132DG.....	75
Table A.II 2. Parameters of the model used to exemplify the pre-design process	78
Table A.II 3. Extract from the <i>Magnetostatic</i> model output	79
Table A.II 4. Active regions in the fluid gap domain.....	81
Table A.II 5. Average yield stresses in each active portion of fluid gap domain [<i>kPa</i>].	81
Table A.II 6. Parameter values for model n° 20.....	82
Table A.II 7. Obtained values of magnetic field strength for each zone.....	84
Table A.II 8. Details of the first 15 analyzed models in the pre-design stage.....	86
Table A.II 9. Influence of the diameter of the holes over the viscous force	86
Table A.II 10. Geometric parameters for pre-design.....	87
Table A.II 11. Summary of current ratings for each AWG Gauge	87
Table A.II 12. Tests characteristics	90
Table A.II 13. Numerical results for each test.....	91
Table A.II 14. Controllable force comparison between both models.....	97
Table A.II 15. Controllable force comparison between configurations with equal stroke	99
Table A.II 16. Summary of results for both models.....	104

Table A.III 1. Values of each parameter. 109

LIST OF FIGURES

Figure 1. Application of an MR-damper in a TMD in <i>Parque Araucano</i> building	5
Figure 2. Comparison between the Bingham and Beverly-Tanner model	8
Figure 3. Magnetic properties of the fluid: (a) Magnetization curves for SAE 1045 steel and Lord MRF-132DG fluid; (b) MRF-132DG yield stress [<i>kPa</i>] versus magnetic field strength [<i>kA/m</i>]	11
Figure 4. General geometry of the MR-Damper	11
Figure 5. Magnetostatic model and boundary conditions: (a) Geometry, (b) FE mesh, and (c) Direction of electric current in each coil.....	14
Figure 6. Desired magnetic flux and coils numbering	14
Figure 7. Magnetic flux density around the third coil. (a) Radial flux on the external cylinder. (b) Axial flux on steel casing and internal cylinder.	15
Figure 8. Magnetic field strength in the fluid gap	15
Figure 9. Fluid domain. (a) full geometry, (b) reduced geometry due to symmetry (used model), and (c) FE mesh of the <i>CFX</i> model.....	16
Figure 10. Imposed boundary conditions for the flow, (a) Inlet and opening, and (b) Fluid-fluid interface.....	17
Figure 11. Numerically estimated constitutive relationships of the <i>CFX</i> model. (a) force-velocity, and (b) force-displacement.....	18
Figure 12. Validation model: (a) damper geometry; (b) magnetostatic mesh; (c) <i>CFX</i> FE model mesh; and (d) 15 [<i>ton</i>] MR-damper.....	20
Figure 13. Measured and predicted <i>f-v</i> constitutive relationship of the 15 [<i>ton</i>] MR-damper comparison	21
Figure 14. Parametric analyses results. (a) Controllable force F_{τ} [<i>ton</i>] versus spacing between coils b [<i>mm</i>]; (b) Controllable force versus electric current, when $b=50$ [<i>mm</i>]; (c) Force-velocity curves for different values of v_0 ; (d) Dynamic range versus gap size	23

Figure 15. Geometry of the extra models to be compared with the proposed model: (a) Three coils; (b) Five coils; (c) Diamagnetic rings on the external cylinder only; (d) Diamagnetic rings in the external and internal cylinder.	25
Figure 16. Picture of the final product of the MR-damper.....	27
Figure 17. Measured f - v and f - δ constitutive relationships for different amplitudes and frequencies.....	29
Figure 18. Test 21: (a) Measured pressure of both chambers & temperature; (b) Measured and calculated force by measuring the pressure difference between chambers.	30
Figure A.I 1. Photographical sequence of the geometry in <i>Magnetostatic</i> model	41
Figure A.I 2. Schematic view of the MR-damper (Dimensions in [mm]).....	42
Figure A.I 3. <i>Solid117</i> element.....	43
Figure A.I 4. Boundary condition: Magnetic flux parallel.....	44
Figure A.I 5. Boundary condition: Electric current on each coil	44
Figure A.I 6 Arrows diagram of the radial magnetic flux densities over the external bi-metallic cylinder	45
Figure A.I 7. Arrows diagram of the radial magnetic flux densities over the central region of the external bi-metallic cylinder.	46
Figure A.I 8. Magnetic flux values around each coil	47
Figure A.I 9. Yield stress distribution obtained from <i>Magnetostatic</i> model and processed with Matlab, to be used as an input of the fluid dynamics model.	47
Figure A.I 10. Representation of the Bingham model.....	48
Figure A.I 11. Full fluid geometry. (a) Initial view, (b) Longitudinal cut	49
Figure A.I 12. <i>CFX</i> model geometry.....	50
Figure A.I 13. Imposed flow model conditions. (a) Inlet, (b) Opening	51
Figure A.I 14. Fluid-fluid interface. (a) Periodic interface, (b) Periodicity about x-axis	52

Figure A.I 15. Monitored force	53
Figure A.I 16. RMS values for <i>CFX</i> model.....	54
Figure A.I 17. Viscous force predicted by <i>CFX</i> Ansys software. (a) Relationship with displacement; (b) Relationship with velocity	55
Figure A.I 18. Schematic view of the MR-damper for comparison between moving mesh and imposed flow methods	57
Figure A.I 19. <i>F-D</i> curves comparison for moving mesh and imposed flow methods ..	58
Figure A.I 20. <i>F-V</i> curve obtained with <i>CFX</i> and $dt = 1 \cdot 10^{-6}$ [s]	59
Figure A.I 21. <i>F-V</i> curve obtained with <i>CFX</i> and $dt = 1 \cdot 10^{-4}$ [s]	60
Figure A.I 22. Linear approximation of <i>F-V</i> curve obtained with <i>CFX</i> and $dt = 1 \cdot 10^{-4}$ [s]	61
Figure A.I 23. Approximation based on interval averages of <i>F-V</i> curve obtained with <i>CFX</i> and $dt = 1 \cdot 10^{-4}$ [s]	62
Figure A.I 24. Fitting schemes comparison. (a) Both fitting schemes together; (b) Along with <i>CFX</i> <i>F-V</i> curve with $dt = 1 \cdot 10^{-6}$ [s]	63
Figure A.I 25. Electric current on each coil of the validation model	65
Figure A.I 26. Desired magnetic flux of the validation model.....	65
Figure A.I 27. Magnetic field strength in the fluid gap, validation model.....	66
Figure A.I 28. Imposed flow boundary conditions at the initial and final ends of the domain, validation model	67
Figure A.I 29. Force-Velocity curve obtained in <i>CFX</i> , validation model.....	68
Figure A.I 30. Force-Displacement curve obtained in <i>CFX</i> , validation model.....	68
Figure A.I 31. Experimental results for MR-damper harmonic testing: (a) F-D constitutive; and (b) F-V constitutive relationships	69
Figure A.I 32. Comparison between the measured and predicted force–velocity relationship of the 15 [ton] MR-damper.....	70
Figure A.I 33. Comparison between the measured and predicted force–displacement relationship of the 15-ton MR-damper	70

Figure A.I 34. <i>F-D</i> curve obtained for the model taken into account for heating estimation.	71
Figure A.II 1. B-H curve for SAE 1045 steel.....	75
Figure A.II 2. B-H curve, Lord MRF 132DG fluid.....	76
Figure A.II 3 Yield stress vs magnetic field strength, Lord MRF 132DG	76
Figure A.II 4. Configuration used for the pre-design stage.....	78
Figure A.II 5. View of the mesh of model n° 20.....	79
Figure A.II 6. Magnetic field intensity over the fluid domain of model n° 20	80
Figure A.II 7. Schematic view of the left coil. Dimensions are expressed in [mm].....	84
Figure A.II 8. Cylinder test configuration	89
Figure A.II 9. Initial test cylinder	90
Figure A.II 10. Pressure vs Measured radial deformation. (a) Test N°1, (b) Test N°2, (c) Test N°3.....	92
Figure A.II 11. External winding configuration geometry	94
Figure A.II 12. Internal winding configuration geometry	94
Figure A.II 13. Magnetic flux paths for external winding configuration	95
Figure A.II 14. Magnetic flux density, internal winding.....	96
Figure A.II 15. Magnetic field strength, internal winding.....	97
Figure A.II 16. Geometry of the alternative for internal winding with equal stroke	98
Figure A.II 17. Magnetic flux density, internal winding with equal stroke	99
Figure A.II 18. Geometry comparison for both models. (a) Three coils configuration, (b) Five coils configuration.....	101
Figure A.II 19. Views of the meshing for the models with an odd number of coils. ...	102
Figure A.II 20. Fluid yield stress, τ_0 . (a) Three coils (b) Five coils	103
Figure A.II 21 Geometry, (a) Steel core only; (b) Steel + MR fluid core	105
Figure A.II 22. Maximum magnetic flux density in the fluid gap domain.....	106
Figure A.II 23. Maximum magnetic field strength in the fluid gap domain, steel core	107

Figure A.III 1. Schematic view of the parameter b	109
Figure A.III 2. F_t versus b . (a) Interval $b = [45,70]$; (b) Interval $b = [45,200]$	110
Figure A.III 3. F_τ vs i	112
Figure A.III 4. Maximum force obtained for each model, after the linear fitting	114
Figure A.III 5. Geometry modeled for maximum velocity analysis	115
Figure A.III 6. Representative average yield stress τ_{av} in the fluid gap domain versus the gap size	117
Figure A.III 7. Viscous force vs gap size, obtained with Ansys 12.1 <i>CFX</i> software...	117
Figure A.III 8. Dynamic range vs gap size.....	118

ABSTRACT

This investigation aims to understand by numerical simulation the behavior of large-capacity MR-dampers to be used for seismic applications in high rise buildings. An example of this was the reduced-scale damper developed earlier and placed in the Parque Araucano, which was active during the last February 27, 2010, Chile earthquake. More specifically, multi-physics finite element models are used to investigate the magnetic and fluid dynamics behavior of these dampers in order to reduce the cost of development and proof-of-concept testing of new designs. In this model, the magnetic field is represented through the well-known Maxwell equations, while the fluid dynamics are controlled by the Navier-Stokes equations. In our simplified representation, both fields, magnetic and fluid, are coupled through the viscosity of the magneto-rheological fluid used, which depends on the magnetic field intensity. To test its validity, the FE model developed was used to blindly predict the experimental behavior of the 15 [ton] MR-damper, subjected earlier to a series of pseudo-static and dynamic tests. Moreover, the numerical model is used for the design of a new large-capacity, 97 [ton] MR damper, which initial experimental results are presented here. The construction of this 97 [ton] MR damper involved several technical challenges, such as the use of an external coil and the confinement of the magnetic flux within a predefined path. Numerical and experimental results for the 15 [ton] MR-damper showed very good agreement, which encourages the use of the cascade magnetic-fluid model proposed herein. Differences between numerical and experimental results are mainly due to the force-velocity constitutive model of the fluid used, which neglects the compressibility of the fluid. Besides being the design tool for the 97 [ton] damper, the numerical model was also used to develop a parametric and sensitivity analysis for different critical design parameters of an MR damper.

Keywords: Magneto-rheological damper, MR fluid, Energy dissipation device, Semi-active damper, Structural dynamics

RESUMEN

Esta investigación tiene por objetivo entender, mediante simulación numérica, el comportamiento de disipadores MR de alta capacidad para aplicaciones sísmicas en edificios de altura. Un ejemplo de ello corresponde al disipador a escala reducida previamente desarrollado e instalado en el edificio Parque Araucano, hasta el último gran sismo del 27 de Febrero de 2010 en Chile. Más específicamente, modelos multi-físicos de elementos finitos se usan para investigar el comportamiento magnético y de la dinámica de fluidos de disipadores MR para reducir el costo de desarrollo y experimentación de nuevos diseños. En este modelo, el campo magnético es representado por las bien conocidas ecuaciones de Maxwell, mientras que la dinámica de fluidos está controlada por las ecuaciones de Navier-Stokes. En nuestra representación simplificada, ambos campos están acoplados mediante la viscosidad del fluido magneto-reológico a usar, la cual depende de la intensidad de campo magnético. Para probar su validez, el modelo FE aquí desarrollado fue usado para predecir el comportamiento experimental del disipador MR de 15 [ton], previamente sometido a una serie de ensayos pseudo-estáticos y dinámicos. Además, el modelo numérico es usado para el diseño de un nuevo disipador MR de alta capacidad, 97 [ton], cuyos ensayos experimentales iniciales se presentan en este documento. La fabricación de este disipador involucró diversos desafíos técnicos, como el uso de bobinas externas al cilindro y el confinamiento del flujo magnético en una trayectoria predefinida. Resultados numéricos y experimentales para el disipador MR de 15 [ton] muestran muy buena concordancia, lo que estimula el uso del modelo aquí propuesto. Las diferencias entre resultados numéricos y experimentales se deben principalmente al modelo elegido para la constitutiva fuerza-velocidad, el cual desprecia la compresibilidad del fluido. Finalmente, el modelo numérico fue también usado para desarrollar análisis paramétricos y de sensibilidad para parámetros críticos de diseño de un disipador MR.

Palabras Claves: Disipador magneto-reológico, Fluido MR, Dispositivo de disipación de energía, disipadores semi-activos, Dinámica estructural.

1. INTRODUCTION

Over the last decades, magneto-rheological (MR) dampers have become a promising alternative for energy dissipation systems. They belong to the family of semi-active devices, which have the reliability of a passive device, but their output force can be dynamically controlled with the use of very little external power, and without the input of extra energy to the system. Their main application in structural engineering includes mainly cable-stayed bridges (*Sutong Bridge*, Suzhou, China), Tuned mass dampers (TMD) control (*Parque Araucano Building*, Santiago, Chile), while they are widely used in vehicles suspension systems.

Multi-physics finite-element numerical models are becoming increasingly sophisticated and useful to unveiling the complex behavior of energy dissipation devices such as magneto-rheological (MR) dampers, where different fields (magnetism, fluid dynamics, mechanical stresses, heat transfer) interact. MR-dampers dissipate energy by means of the viscous flow of a fluid consisting on micro-sized magnetically polarized carbonyl iron particles dispersed in a carrier oil. When in presence of a magnetic field, these particles are lined up in chains, which change the fluid viscosity, turning it into a semisolid in a few milliseconds by exhibiting plastic behavior. Among other semi-active devices like electro-rheological (ER) dampers, they have shown to be a convenient alternative, because maximum magnetostatic energy density is two orders of magnitude larger than electrostatic density, which makes its yield stress to be about ten times higher than that of ER fluids (Yang, 2001).

A scaled MR-damper with capacity 15 [ton] was installed during the last February 27th, $M_w=8.8$, Chile earthquake. The damper was acting on a tuned-mass of 160 [ton] on the roof of the *Parque Araucano* building, in Santiago, Chile. Two recent publications elaborate on the main aspects of such implementation (Zemp, 2008). The system was activated during the earthquake, but it was mechanically disconnected from the TMD as the mass displacement exceeded 10 [cm]. Although the building was not instrumented, no damage was observed in the structure or in its contents.

The literature in MR-dampers is ample, but the one related to multi-physical modeling of interacting fields is scarce. Motivated by that, this paper deals with a FE numerical model describing the magnetic behavior and fluid dynamics of an MR-damper, which objective is to obtain a numerical estimation of its stress-strain (force-deformation) constitutive behavior. Previously, a 2D-axisymmetric model was analyzed in Ansys and results for four different pistons were derived, reaching similar force values, although this model was not contrasted with experimental testing (Walid, 2002). Besides, Yang developed an approximate analytical expression for the viscous and controllable forces of MR-dampers that has been used in damper designs (Yang, 2001).

In practice, most of the models used to design an MR-damper are based on a phenomenological approach (Spencer et al., 1997; Butz, 2002) or mathematical models (Brigadnov, 2005; Costa, Costa Branco, 2009; Chooi, Oyadiji, 2008). Consequently, this study aims to model the MR-damper behavior with state-of-the art numerical tools in order to predict its cyclic behavior. Based on that analysis, a numerical model for a 97 [ton] MR-damper is included in this paper for real-scale application in the *Parque Araucano* building. The model was first validated with the results of an existent MR-damper already installed on the building (Zemp, 2008) and then with experimental testing. A brief summary of the most relevant aspects of the design and fabrication are also discussed herein.

The specific goals of this research were: (i) to numerically predict the total force of a large-scale MR-damper with the help of a state-of-the art FE software; (ii) to use an existent MR-damper to validate the numerical model; (iii) to fabricate a large-scale MR-damper in a local manufacturer; and (iv) to perform analyses to certain geometric and boundary conditions parameters. To achieve the first goal, two models in Ansys 12.1 working in cascade were used: a magnetic model, responsible for computing the magnetic field produced in the damper due to the currents that run inside the coils, and a fluid dynamics model, responsible of accounting for the fluid yield stress caused by the magnetic field obtained by the magnetic model (cascade effect), and predicting the damper force by simulating the fluid dynamics. The constitutive behavior of the fluid uses an adaptation of the Bingham model, presented by Beverly & Tanner (Beverly,

Tanner, 2006). Based on these analyses, the force-velocity (F-V) constitutive relationship for a prescribed sinusoidal movement of the piston was predicted. By knowing the pressures on the piston heads, they can be integrated to obtain the total damper capacity provided by the pressure difference between the two piston chambers. The Ansys software used in this research included its *CFX* (fluid dynamics), *ICEM CFD* (fluid domain meshing) and *Magnetostatic* (magnetic field) applications.

The following chapter corresponds to the article that aims to be published in an ISI Journal, where the theory involved in MR-damper physics is exposed and the model in cascade is presented. The article also includes a validation of the method, where an existent MR-damper is considered along with its cyclic response on experimental dynamic tests, as well as parametric and comparative analyses. Main aspects of the fabrication of the damper are also discussed in the article.

In chapter 3 the main conclusions of the research are presented, followed by three appendices that explain the process behind the investigation. In Appendix I all aspects involved in modeling an MR-damper with the method explained herein are described. In Appendix II, aspects of the design of the MR-damper are discussed, while in Appendix III parametric analyses are explained.

2. MULTIPHYSICS ANALYSIS OF A MAGNETO-RHEOLOGICAL DAMPER AND EXPERIMENTAL VALIDATION

2.1 Introduction

Multi-physics finite-element numerical models are becoming increasingly sophisticated and useful in interpreting the complex behavior of energy dissipation devices such as magneto-rheological (MR) dampers, where different fields -magnetism, fluid dynamics, mechanical stresses, heat transfer- interact. MR-dampers dissipate energy by means of the viscous flow of a fluid consisting on micro-sized magnetically polarized carbonyl iron particles dispersed in a carrier oil. When in presence of a magnetic field, these particles are lined up in chains, thus changing the fluid viscosity, turning it into a semisolid in a few milliseconds and exhibiting plastic behavior. Among other semi-active devices like electro-rheological (ER) dampers, they have shown to be a convenient alternative, because maximum magnetostatic energy density is two orders of magnitude larger than electrostatic density, which makes the yield stress to be about ten times higher than that of ER fluids (Yang, 2001).

A real application of a scaled MR-damper with capacity 15 [ton] was installed during the last February 27, $M_w=8.8$, Chile earthquake (Figure 1). The damper was acting on a single tuned-mass of 160 [ton] at the roof of the *Parque Araucano* building, in Santiago, Chile [2,3]. During the earthquake, the system was mechanically disconnected from the TMD as the mass displacement exceeded 10 [cm]. Although the building was not seismically instrumented, no damage was observed neither in the structure nor in its contents.

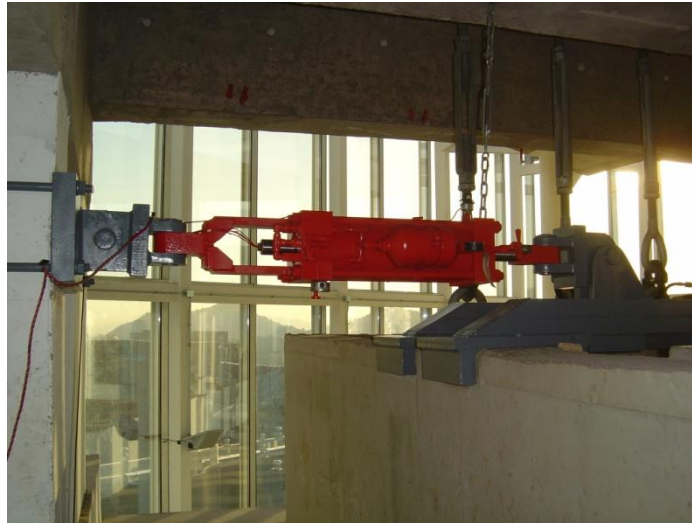


Figure 1. Application of an MR-damper in a TMD in *Parque Araucano* building

The literature in MR dampers is ample, but the one related to multi-physical modeling of interacting fields is scarce. Motivated by that, this paper deals with a FE numerical model describing the magnetic behavior and fluid dynamics of an MR-damper, which objective is to obtain a numerical estimation of the force-deformation constitutive behavior, for design purposes. Previously, a 2D-axisymmetric model was analyzed in Ansys and results for four different pistons were derived, reaching similar force values, although this model was not contrasted with experimental testing (Walid, 2002). Besides, Yang developed an approximate analytical expression for the viscous and controllable forces of MR-dampers that has been used successfully in damper designs (Yang, 2001).

In practice, most of the models used in MR-damper are based on a phenomenological approach (Spencer et al., 1997; Butz, 2002) or, alternatively, mathematical models (Brigadnov, 2005; Costa, Costa Branco, 2009; Chooi, Oyadiji, 2008). Because of the current state of the art of FE analyses, this study aims to model the MR-damper behavior with numerical tools in order to predict the cyclic behavior of the damper under sinusoidal excitations, thus saving considerable experimental work. Based on that analysis, a numerical model for a nominally 97 [ton] MR-damper is

included in this paper for real-scale application in the *Parque Araucano* building. The model was first validated with the results of the existent scaled damper in the building (Zemp, 2008), and then with a new round of experimental testing. For the sake of completeness, a brief summary of the most relevant aspects of the damper design and fabrication are discussed herein.

Consequently, the specific goals of this research were: (i) to develop and manufacture a large-scale proof-of-concept MR damper; (ii) to numerically predict the force-deformation and force velocity constitutive relationships of the MR damper using state-of-the art FE software, and validate the model with the 15 [ton] and 100 [ton] dampers; and (iii) perform parametric analyses of the damper with different geometries and boundary conditions. To achieve these goals, two models were developed that considered in cascade a magnetic model, responsible for computing the magnetic field produced in the damper due to the current running through the coils, and a fluid dynamics model, responsible of accounting for the fluid yield stress caused by the magnetic field computed from the FE magnetic model, which leads to the damper force through the fluid dynamics model.

2.2 Problem Formulation

Most of the material presented in this section is well known and may be shipped by the informed reader. However, it is presented with the simple purpose of making the article self-contained. Hence, a summary of the physical and mathematical models that will be used herein is included.

For high shear rates, an MR-fluid can be well represented by the Bingham constitutive model (Butz, 2002); models for lower shear rates usually depend on parameters that need to be calibrated with experimental results. The Bingham mathematical representation can be written in terms of the dynamic viscosity as:

$$\eta(\dot{\gamma}, \mathbf{H}) = \frac{\tau_0(\mathbf{H})}{\dot{\gamma}} + \eta_\infty, \quad \tau > \tau_0(\mathbf{H}) \quad (1)$$

where \mathbf{H} corresponds to the magnetic field strength in the fluid domain; $\eta(\dot{\gamma}, \mathbf{H})$ is the dynamic viscosity, $\tau_0(\mathbf{H})$ represents the fluid yield stress dependent on the magnetic field strength; $\dot{\gamma}$ is the shear strain rate of the fluid; η_∞ corresponds to the inherent dynamic viscosity of the fluid in absence of a magnetic field; and τ represents the fluid shear stress. For usual materials, there is a linear dependence between the magnetic flux density \mathbf{B} and \mathbf{H} , given by the magnetic permeability, but in the case of MR-fluid, this dependence is non-linear and is given by the manufacturer, as it will be further shown. A computational adaption of this model is required to implement it in the Ansys CFX platform 0. According to the model proposed by Beverly-Tanner (B&T) (Beverly, Tanner; 2006), and taking Eq. (1) as a basis, the fluid may be modeled as an equivalent bilinear Newtonian fluid with a field dependent dynamic viscosity, i.e.

$$\boldsymbol{\eta} = \begin{cases} \frac{\tau_0(\mathbf{H})}{\dot{\gamma}} + \eta_\infty, & \dot{\gamma} \geq \dot{\gamma}_0 \\ \alpha\eta_\infty, & \dot{\gamma} < \dot{\gamma}_0 \end{cases} \quad (2)$$

where α is a non-dimensional impedance parameter in the pre-yield region of the fluid, and $\dot{\gamma}_0$ corresponds to the critical shear strain rate given by $\dot{\gamma}_0 = \tau_0(\mathbf{H})/((\alpha-1)\eta_\infty)$. This alternative is compared schematically with the Bingham model in Figure 2. The higher the value of α , the better the consistency between the two models.

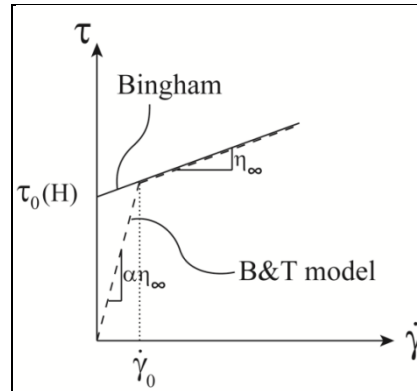


Figure 2. Comparison between the Bingham and Beverly-Tanner model

The MR fluid used in this research is the Lord MRF-132 DG and has the properties shown in Table 1. The magnetic properties of the fluid are given by the manufacturer and they are characterized by a magnetization (B - H) curve, and the yield stress–magnetic field strength constitutive relationship 0. A comparison between the B - H curves for the MR-fluid and steel SAE 1045 0 is plotted in a logarithmic axis in Figure 3(a). It is apparent that magnetization of steel is larger, faster and occurs for smaller values of the magnetic field strength, reaching a saturated state for lower H than the fluid. Furthermore, the relationship between the yield stress and magnetic field strength is shown in Figure 3(b), where the yield stress gets essentially saturated at a value of 48.32 [kPa] as H reaches 300 [kA/m]. This result suggests an upper limit for the current intensity.

Table 1. Properties of Lord MRF 132DG fluid

Properties	MRF 132DG Fluid
Fluid density	~ 3 [gr/cm^3]
Dynamic viscosity @ 40°C,	0.092 ± 0.015 [$Pa \cdot s$]
Solid content by weight	80.98%
Operating temperature	-40 to +130 [$^{\circ}C$]
Field dependent yield stress	Figure 2 (b)

The configuration of the MR damper considered in this research is shown schematically in Figure 4, and is formed by: (i) a piston; (ii) an internal steel cylinder; (iii) a bi-metallic external cylinder with a radial gap h relative to the internal cylinder; (iv) four coils wound around the external cylinder; (v) a steel casing covering the coils; (vi) two steel head plates; and (vii) magneto-rheological fluid filling out every empty space. For the geometry of the MR-damper considered (Figure 4), the fluid passes from one chamber to the next through the thin gap external to the fluid chambers. While the fluid moves along the gap impulsed by the displacement of the piston, the flow crosses the magnetic flux, generated by the external coils wound around the external steel cylinder. The magnetic field is controlled externally by the current intensity following a target control algorithm (Zemp, 2008). Please note also that the shear stress-velocity constitutive relationship of the fluid is a function of the magnetic field strength H . Moreover, there is no space between the piston and the internal cylinder, so the only possible way for the fluid to move between chambers is through the orifices present in the internal cylinder, which are connected to the gap. All steel elements are made with SAE 1045 steel.

Since the coils are not in direct contact with the fluid, a diamagnetic material is used to force the magnetic flux to cross the MR fluid at several locations as indicated in Figure 4. Some of the advantages of this configuration are that the coils may be intervened without disassembling the entire damper; the analysis is also simpler

computationally, because the magnetic field is invariant in time when the coils are wound around a non-moving component; and the resulting piston length is smaller, allowing a larger stroke. Nevertheless, other configurations for the MR damper were also simulated to better understand the advantages of one or the other. MR dampers with two, three and five external coils, and a damper with internal coils around the piston were also considered. Moreover, using as a benchmark the MR-damper with four coils, several changes to geometric dimensions as gap size, spacing between coils, piston radius, and cylinder length were also investigated.

By using the axial symmetry of the problem, it is possible to reduce the *CFX* model to 1/12th of its original size, which enables a more accurate representation of the singularities and complexities of the fluid behavior. Computing time is improved by this reduction in 94.3%, since the nature of this problem leads to a set of numerically stiff differential equations due to the inclusion of the fluid yield stress in the model; the integration requires a very small time-step, $dt = 1 \cdot 10^{-6}$ [s]. This simplification due to symmetry is not done in the *Magnetostatic* model because it does not improve significantly the computational cost. Moreover, a reduction in the size and a change on the boundary conditions of the problem in order to make it symmetric, lead to unreliable results using the current version of Ansys.

Before proceeding with the formulation and numerical implementation of the model, it seems relevant to summarize the different field equations that govern its physical behavior (Table 2). The electromagnetic equations are represented by the well known Maxwell equations, while Navier-Stokes equations are used to model the dynamical behavior of the fluid. It is assumed that the interaction between the different fields is given only by the dependence of the dynamic viscosity η on the magnetic flux density \mathbf{B} vector.

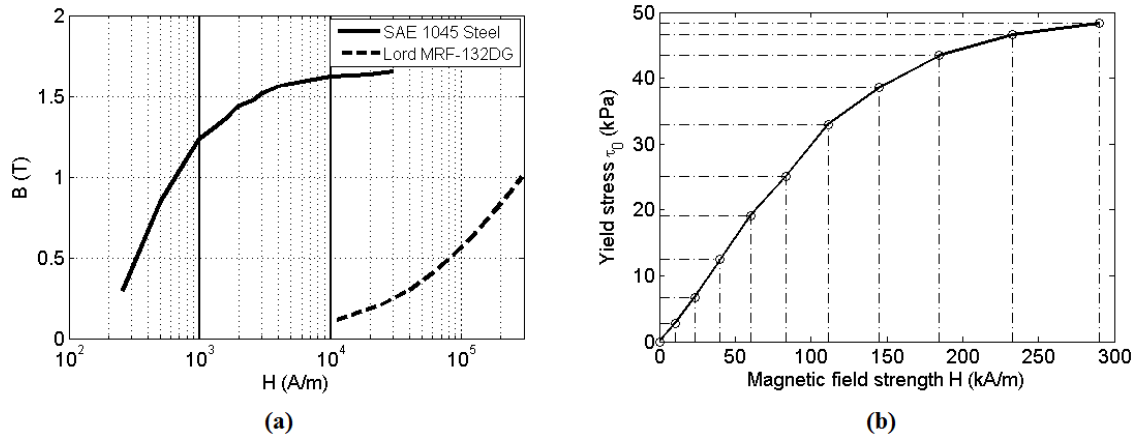


Figure 3. Magnetic properties of the fluid: (a) Magnetization curves for SAE 1045 steel and Lord MRF-132DG fluid; (b) MRF-132DG yield stress [kPa] versus magnetic field strength [kA/m]

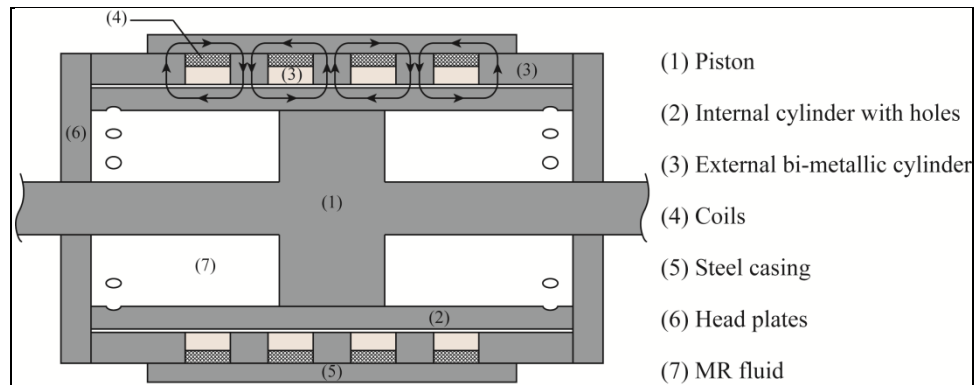


Figure 4. General geometry of the MR-Damper

Table 2. Field equations

Electro-Magnetic Equations (Maxwell)	Fluid Dynamics Equations (Navier-Stokes)
<ul style="list-style-type: none"> • $\nabla \cdot \mathbf{E} = \frac{\rho}{\epsilon_0}$ (Gauss Law) • $\nabla \cdot \mathbf{B} = 0$ (Gauss Law for Magnetism) • $\nabla \times \mathbf{E} = -\frac{\partial \mathbf{B}}{\partial t}$ (Faraday Induction Law) • $\nabla \times \mathbf{B} = \mu_0 \mathbf{J} + \mu_0 \epsilon_0 \frac{\partial \mathbf{E}}{\partial t}$ (Ampere Circuital Law) 	<ul style="list-style-type: none"> • $\nabla \cdot \mathbf{u} = 0$ (Continuity) • $\rho \frac{\partial \mathbf{u}}{\partial t} + \rho(\mathbf{u} \cdot \nabla)\mathbf{u} = -\nabla p + \dots$ $\nabla \cdot \{\boldsymbol{\eta}(\dot{\gamma}, \mathbf{H}(\mathbf{B}))(\nabla \mathbf{u} + (\nabla \mathbf{u})^T)\} + \mathbf{F}$ (Momentum)
Lorentz Force (Constitutive equation): <ul style="list-style-type: none"> • $\mathbf{F} = q(\mathbf{E} + \mathbf{v} \times \mathbf{B})$ Body Force Interaction 	Constitutive equation (Bingham model) <ul style="list-style-type: none"> • $\boldsymbol{\eta}(\dot{\gamma}, \mathbf{H}(\mathbf{B})) = \frac{\tau_0(\mathbf{H}(\mathbf{B}))}{\dot{\gamma}} + \eta_\infty, \quad \tau > \tau_0(\mathbf{H}(\mathbf{B}))$
Where:	Where:
<ul style="list-style-type: none"> • \mathbf{E} = Electric field, [V/m]; • \mathbf{B} = Magnetic field density, [T]; • \mathbf{H} = Magnetic field strength, [A-turn/m]; • \mathbf{J} = Current density, [A/m²]; • ρ = Volumetric charge density, [C/m³]; • ϵ_0 = Permittivity of free space = 8.85×10^{-12}, [F/m]; • μ_0 = Permeability of free space = $4\pi \times 10^{-7}$, [N/A²]; • q = Particle charge, [C]; • \mathbf{v} = Particle velocity, [m/s]. 	<ul style="list-style-type: none"> • \mathbf{u} = Velocity field, [m/s]; • ρ = Fluid density, [kg/m³]; • $\dot{\gamma}$ = Shear strain rate, [1/s]; • $\boldsymbol{\eta}$ = Dynamic viscosity, [Pa-s]; • η_∞ = Dynamic viscosity when no magnetic field is present, [Pa-s]; • p = Pressure in one point of the fluid domain, [Pa]; • τ = Shear stress, [Pa]; • τ_0 = Yield stress, [Pa]; • \mathbf{F} = Body forces, [N].

The integration strategy proposed herein considers first to solve the set of field equations of the magnetic field, and apply these results into the fluid problem, thus uncoupling the set of equations. The main rationale behind this assumption is that the magnetic field is invariant in time, and the model calibrations will be performed using experimental tests that are done at constant values of the current intensity. Therefore, the fluid dynamics model takes the output of the magnetostatic model as an input for obtaining the dynamic viscosity according to the Beverly & Tanner (B-T) model (Beverly, Tanner, 2006). A three-dimensional FE model capable of changing both models in time, the fluid dynamics and the magnetic field, would be necessary to

simulate the damper behavior subjected to controlled conditions on a building, a task that goes beyond the scope of this research.

2.3 Magnetostatic Model

A schematic view of the 3D model geometry used for the MR damper is presented in Figure 5(a). The finite element (FE) mesh of the model and its boundary conditions are presented in Figure 5(b) and (c) respectively. The FE mesh consists of 801,590 elements, with a total of 1,590,910 nodes. The model includes an external surrounding air chamber that has been intentionally hidden in the figure. Finite elements have been modeled with the *solid117* Ansys element 0, developed to simulate 3D magnetic fields. Boundary conditions are given by zero voltage applied at the external surfaces of the air chamber, and by the electric current intensity that runs inside each coil in opposite directions, as indicated in Figure 5(c). The arrows in Figure 5 (c) represent the direction of the current flow on each coil. Each coil has 250 turns of AWG 16 copper wire and electric current varies from zero to 3[A], in ten equal intervals of 0.3[A] and $dt = 0.01$ [s].

Conceptually, the direction of the magnetic flux expected in the cylinder is shown schematically in Figure 6, for four coils. The flux travels in paths that are in opposite directions, but interact constructively when crossing the fluid gap. Diamagnetic elements conduct the flux to the fluid gap and prevent that it leaks along other steel components.

The solver of the magnetostatic application of Ansys software carries out an iterative procedure (equilibrium iterations) at each sub-step. As usual, successful solutions are reached when the out-of-balance loads are less than the specified convergence tolerance. For the convergence of the magnetic field, the *CSG* convergence criterion is used, which is controlled internally by the software. The *CSG* criterion represents magnetic flux, and if a time-step needs more iterations than the required for convergence, it is dynamically reduced to a half (Ansys Inc, 2009).

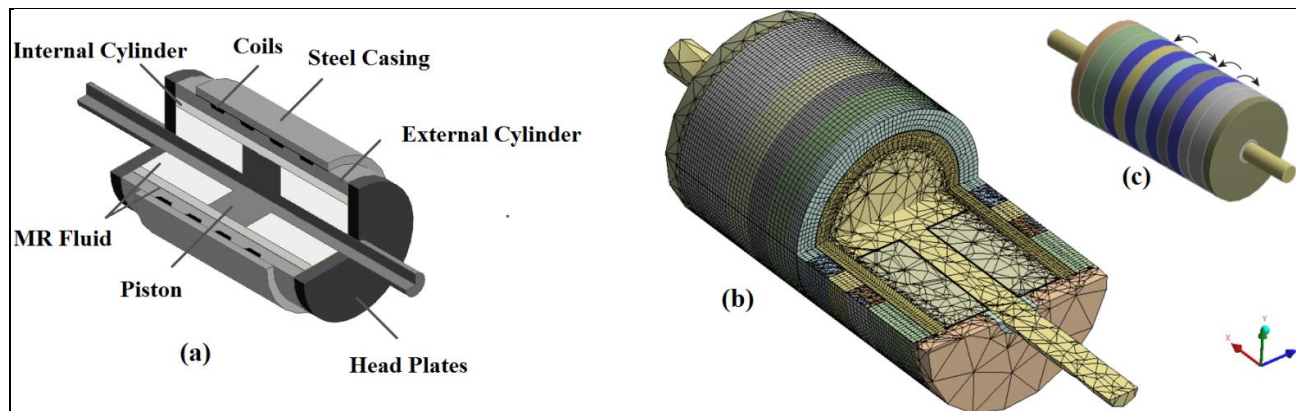


Figure 5. Magnetostatic model and boundary conditions: (a) Geometry, (b) FE mesh, and (c) Direction of electric current in each coil.

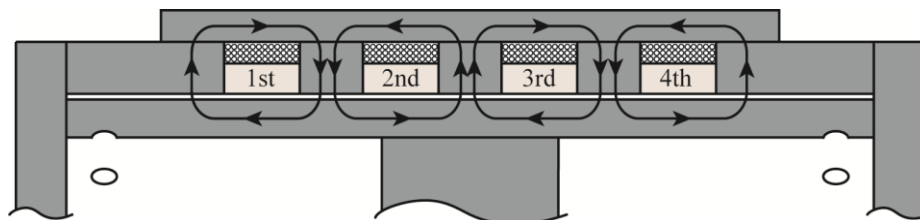


Figure 6. Desired magnetic flux and coils numbering

It is apparent in Figure 7 at the radial path of the flux at both sides of the coils, that the flux interacts with the one resulting from the adjacent coils to the left and right. In this example, the magnetic flux density on the steel components around the third coil subjected to a current intensity of 3 [A] is presented. As a reference, the total flux on the steel casing is $1.67 \cdot 10^{-2}$ [Wb].

On the other hand, shown in Figure 8 is the resulting magnetic field strength H [kA/m]. The zones located between coils concentrate the larger H values, which are above 300 [kA/m], reaching saturation according to the results presented in Figure 3 (b), which is the target for design. Symmetry of the results is essentially explained by the

symmetry of the problem. As explained before, the results in the fluid gap are taken and used as an input for the fluid dynamics model of the damper, taking into account the direct relationship between the magnetic field strength and the fluid yield stress already shown in Figure 3(b).

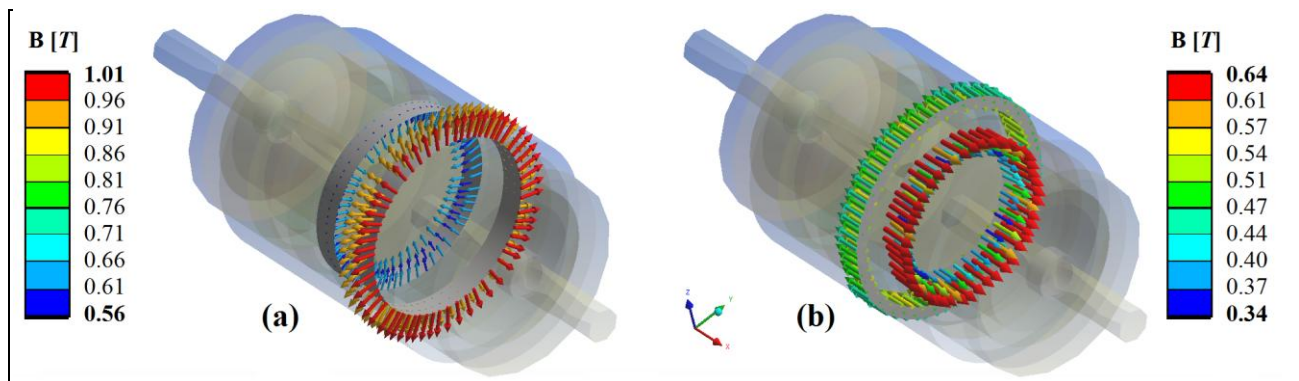


Figure 7. Magnetic flux density around the third coil. (a) Radial flux on the external cylinder. (b) Axial flux on steel casing and internal cylinder.

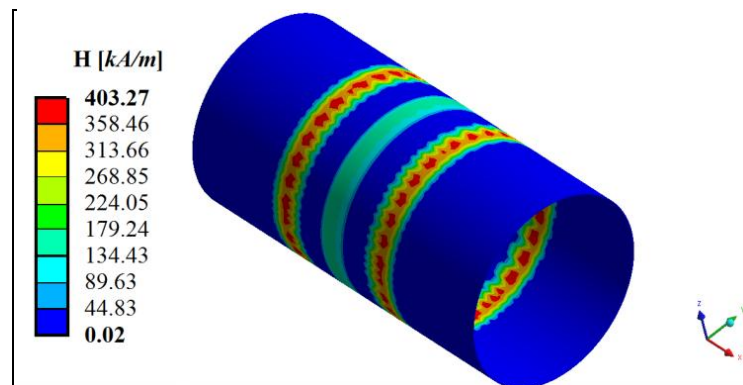


Figure 8. Magnetic field strength in the fluid gap

2.4 Fluid dynamics model

The domain considered in the *CFX* FE model is that of the fluid inside the MR damper. As shown earlier, the damper has a rotational periodicity, and only $1/12^{\text{th}}$ of the entire domain needs to be included in the model; such is the case since the damper has 12 orifices in each side to allow the fluid to pass into the gap Figure 9(a). The full and the reduced domains can be compared in Figure 9(a) and (b), respectively. They are composed by a single fluid domain, including both chambers at either side of the piston, the gap between the internal and external cylinder, and the 24 holes in the internal cylinder that connect the gap to the chambers. The number of orifices in the internal cylinder was selected simulating viscous force models of the MR-damper, and used this quantity as the main parameter. The model was meshed using the *ICEM CFD* application 0, and consists of hexahedral solid elements; the total number of elements is 520,456 and the total number of nodes is 553,434. The gap is meshed separated from the rest of the domain, since it needs several layers of regular elements in order to obtain an accurate velocity profile of the fluid (Figure 9(c)).

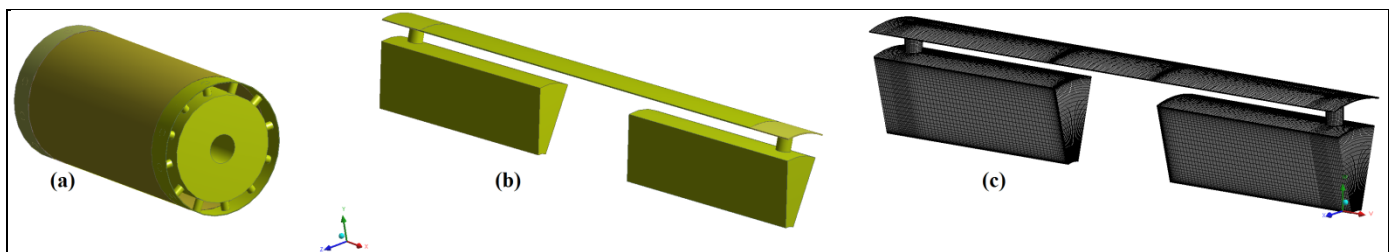


Figure 9. Fluid domain. (a) full geometry, (b) reduced geometry due to symmetry (used model), and (c) FE mesh of the *CFX* model

The boundary conditions applied to the *CFX* model are schematically shown in Figure 10, and correspond to: (i) no-slipping at the cylinders and piston walls; (ii) an inlet at the initial end and an opening at the final end of the domain, with a determined velocity profile and relative pressure, respectively (Figure 10(a)); (iii) rotational periodicity at the fluid-fluid interface for the lateral surfaces of the domain (Figure 10(b)); and (iv) the yield stress obtained from the magnetostatic model used for the dynamic viscosity. An imposed flow at the ends of the model has been finally selected given its simplicity and the negligible differences relative to a model with a moving mesh technique. Consequently, at the inlet, the specified velocity profile is $v_{flow,x} = v_0 \sin(\omega t)$, where v_0 corresponds to the maximum velocity and ω is the frequency [rad/s].

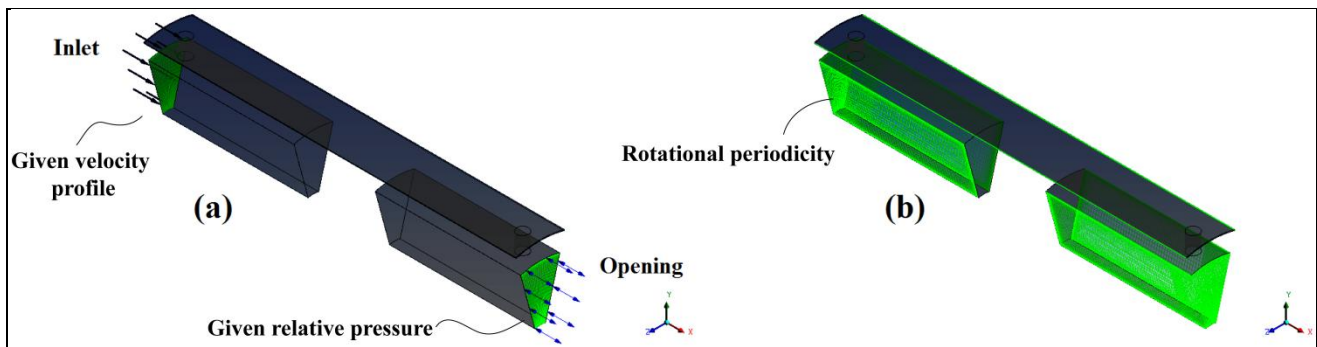


Figure 10. Imposed boundary conditions for the flow, (a) Inlet and opening, and (b) Fluid-fluid interface.

Laminar flow is considered for the model, and a transient analysis is performed with a maximum velocity of $v_{max} = 0.17$ [m/s], a frequency $\omega = 10$ [rad/s], and a time-step $dt = 5 \cdot 10^{-4}$ [s]. Results are then filtered in order to reduce noise due to the coarseness of the time interval. To control the accuracy of the simulation, RMS values are calculated for the three momentum conservation equations and continuity equation. RMS serves as a measure of how well the numerical solution converges and corresponds to the residuals for each equation at the end of each time-step. For adequate accuracy, the

converged solution requires a maximum residual level of $1.0e-4$. RMS residuals in the simulation are usually an order of magnitude lower than this tolerance. If the RMS values do not achieve this limit, simulation continues to the next time-step after 10 iterations (Ansys Inc, 2009).

Damper force is computed by integrating the total pressure on the two faces of the piston. Thus, the constitutive force-velocity (f - v) and force-displacement (f - δ) relationships can be obtained, which are shown in Figure 11(a) and (b), respectively. Please note that the Bingham model is a “static” model, i.e., it does not include the possibility of force-velocity hysteresis, which is typical of fluids with compressibility. By using this model and assumptions, the maximum damper force obtained for the given parameter values was about 97.1 [ton]. The numerical noise in the figures is produced by the time step selected, which, despite being small ($dt = 1 \cdot 10^{-4}$ [s]), is coarser than the one required to assure perfect convergence of the *CFX* simulation; the model data was filtered by a smoothing five-point moving average (MA) scheme. Even with this MA scheme, the numerical noise could not be eliminated completely, although differences in the maximum force value are negligible relative to the output given by the ideal time-step.

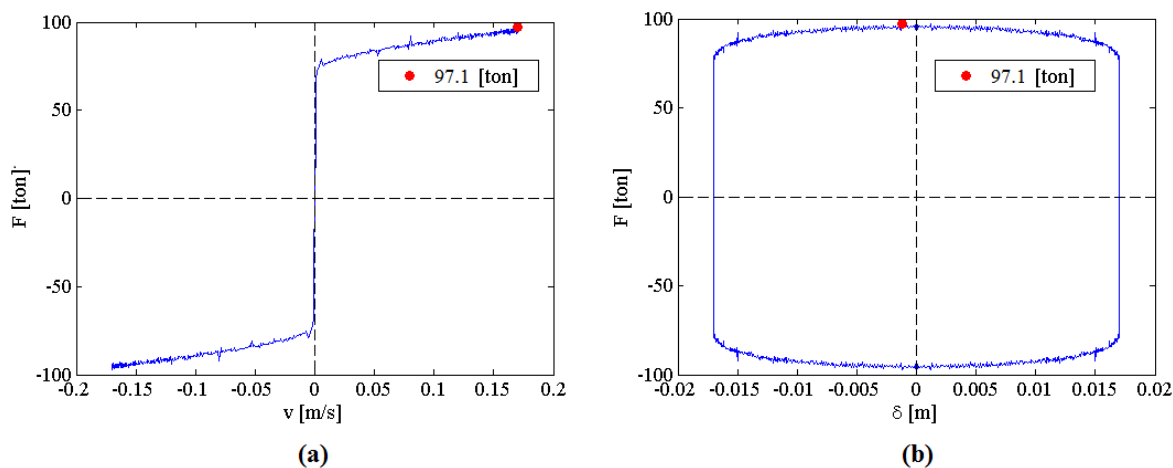


Figure 11. Numerically estimated constitutive relationships of the *CFX* model. (a) force-velocity, and (b) force-displacement

2.5 Model validation

The model developed was first validated by using as benchmark an existent MR-damper (Zemp, 2008), and contrasting the numerical outputs with those obtained earlier by experimental testing. The complete geometry of this damper can be seen in Figure 12(a) and consists of: (i) a piston; (ii) a cylinder; (iii) two coils wound around the piston; (iv) two steel head plates; and (v) the MR-fluid. The design considers a 1.5 [mm] gap between the piston and the cylinder, and a nominal capacity of 15 [ton]. The procedure is the same as explained in previous sections, but for this model a reduction of the fluid domain was not necessary, since the computational cost of this problem was manageable. The mesh of the Magnetostatic model consisted of 61,503 elements and 94,289 nodes, while the mesh of the CFX model has 272,988 elements and 77,485 nodes (Figure 12(b) and (c)). A picture of the damper is shown in Figure 12(d); further details of this solution may be found elsewhere (Zemp, 2008).

The first set of experiments consisted of harmonic motions applied to the piston at different constant current intensities, corresponding to $I = 0, 0.5, 1, 1.5, 2$ and 2.5 [A]. Testing included also different displacement amplitudes and cycling frequencies. The test used to validate the FE numerical model corresponds to a maximum displacement of 5 [cm], a period of 2.7 [s], and a current intensity of 2 [A], which correspond to typical building design values. The force measured with these parameters was 13.8 [ton], while the maximum force of the damper is 14.8 [ton] at 2.5 [A].

Shown in Figure 13 is a comparison between the force-velocity constitutive relationship $f-v$ obtained numerically and the experimental result. Maximum force predicted is 0.32% greater than the one obtained by experimental testing. As it was explained before, the Bingham model was not capable of capturing the hysteresis observed in the experimental $f-v$ relationship.

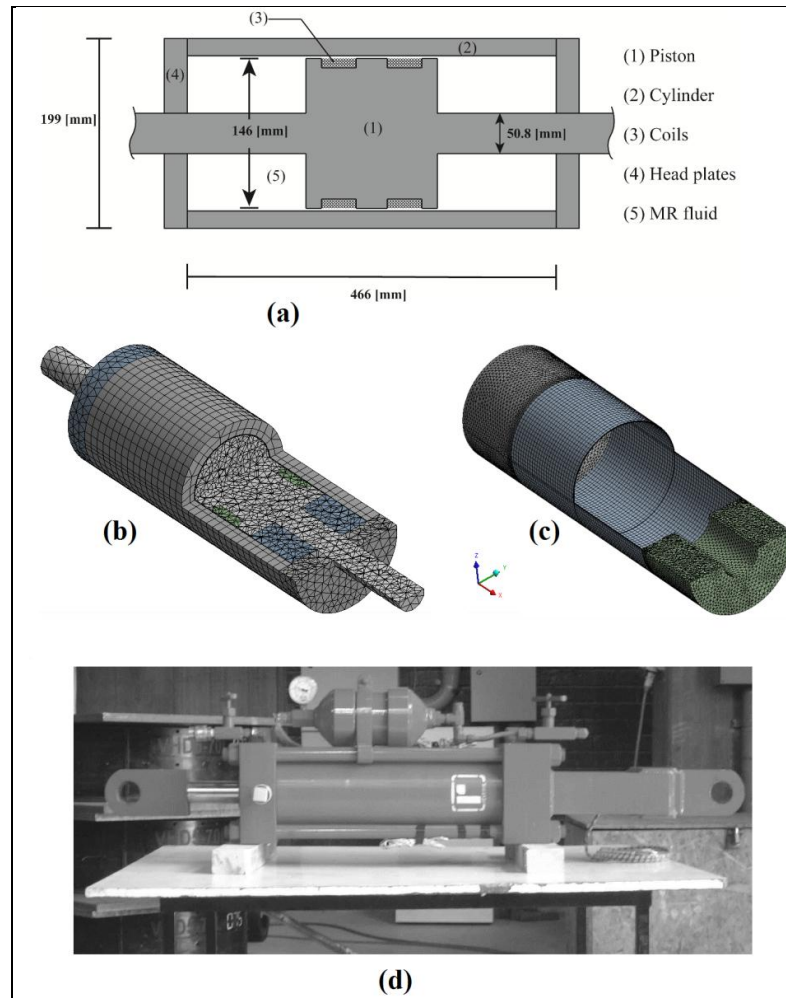


Figure 12. Validation model: (a) damper geometry; (b) magnetostatic mesh; (c) *CFX* FE model mesh; and (d) 15 [ton] MR-damper

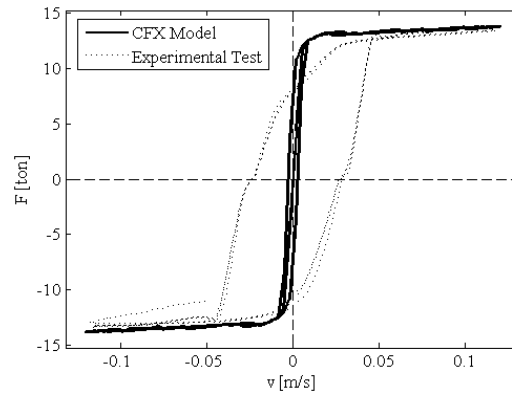


Figure 13. Measured and predicted f - v constitutive relationship of the 15 [ton] MR-damper comparison

2.6 Parametric analyses

One of the main advantages of developing a numerical model of the damper is to be able to carry out a sensitivity analysis with different damper parameters. Thus, parametric analyses were performed on the MR damper simulation model by varying the following parameters: (i) axial spacing between coils b ; (ii) current intensity i ; (iii) maximum piston velocity v_0 ; and (iv) gap size h . By varying axial spacing of the coils, an optimal distribution of the magnetic field strength (H) can be obtained, i.e., an optimum volume of saturated fluid. Current intensity helps us to understand the importance of the power source used, while velocity conditions are related to different ground motion conditions and available damper hardware. Moreover, since the gap size has a strong influence on the dynamic range of the damper, its effect needs to be evaluated.

The same procedure explained earlier was applied for all these parameters, with the exception of the gap size analysis. In that case, Yang's formula (Yang, 2001) for the MR damper was used. Although we found that this formula may differ around 30%

relative to *CFX* results in external coil configurations, it shows the same trend with variable gap size, and hence, it can be used to predict an optimum gap size, to maximize the MR-damper dynamic range.

The variation of the axial spacing between coils, b , was generated by keeping every other geometric parameter constant, except the length of the outer steel casing that needs to stretch in order to cover the coils and generate the magnetic flux circuit. The electric current intensity selected is 3[A], and the values of b that have been considered are 40 to 200 [mm] (Figure 14(a)). The second analysis keeps $b = 50$ [mm], and changes the current intensity in the coils 0 to 3 [A] (Figure 14(b)). The damper controllable force has been obtained for every current value using the *CFX* model. Third, the variation of the maximum velocity considered values of v_0 varying from 17 to 46 [cm/s], in 3 [cm/s] intervals. A lower bound was chosen corresponding to the maximum velocity that can be achieved by the current actuator in the PUC laboratory testing facility, and the upper bound was chosen corresponding to the maximum velocity expected in operation. Finally, a sensitivity analysis of the gap size h was done with values ranging in the interval between 0.9 and 5.5 [mm] and a maximum velocity given by 250 [mm/s]. The gap size has an influence mainly in the viscous force and, hence, controls the dynamic range D . The viscous component of the damper force, F_η was also obtained using the Ansys *CFX* model by representing the fluid properties in absence of a magnetic field (Table 1). The controllable force of the damper is computed by subtracting F_η from the total damper force. The dynamic range D (Figure 14(d)) is defined as the ratio of the controllable force F_τ and the uncontrollable viscous and frictional damper force, $F_\eta + F_f$. The friction force F_f is constant measured while testing the device.

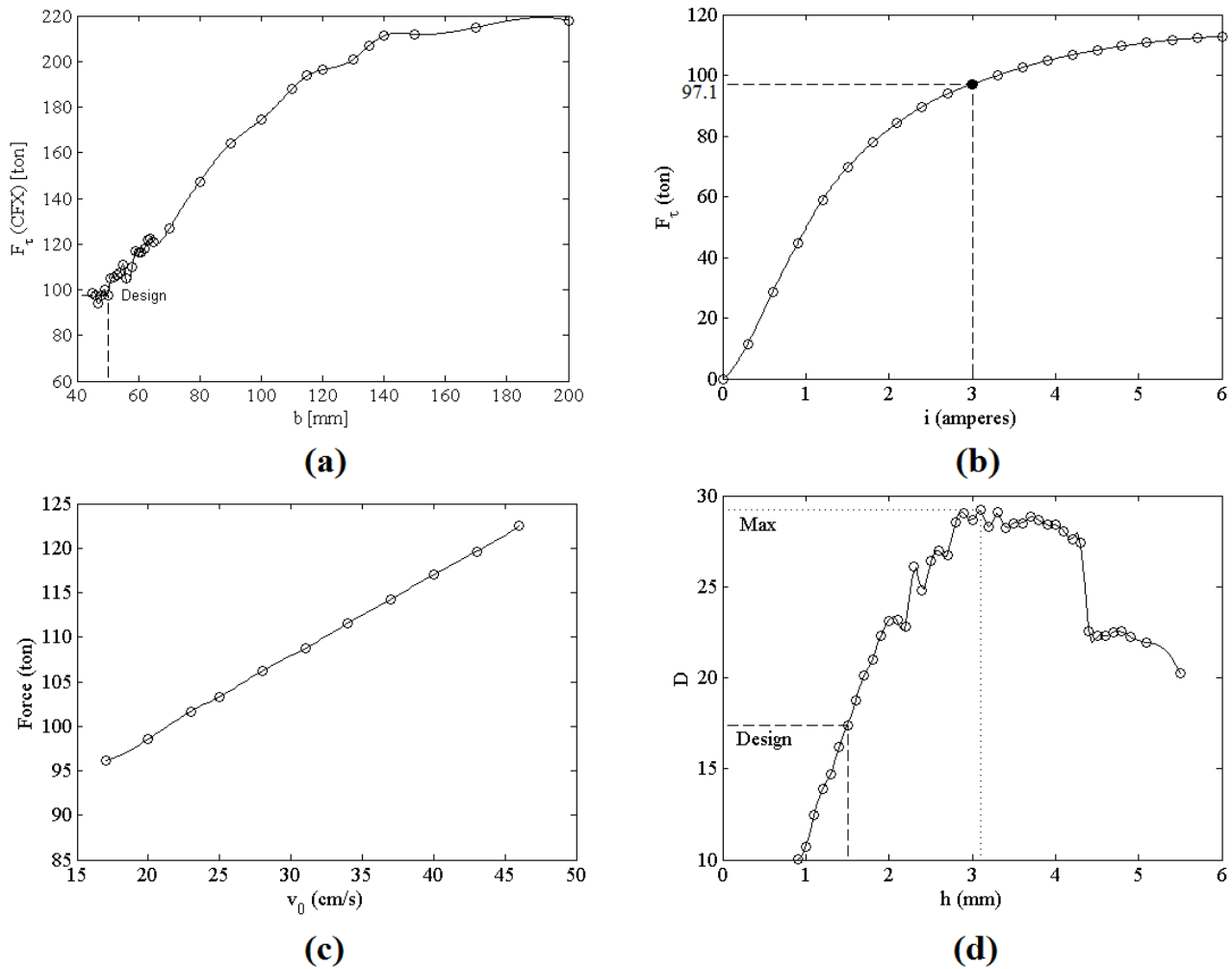


Figure 14. Parametric analyses results. (a) Controllable force F_t [ton] versus spacing between coils b [mm]; (b) Controllable force versus electric current, when $b=50$ [mm]; (c) Force-velocity curves for different values of v_0 ; (d) Dynamic range versus gap size

It is apparent from part (a) of Figure 14 that the value of the controllable force increases as the spacing between coils does. This is a natural conclusion trend since the fluid is magnetically saturated in every model analyzed. But this increase tends to a constant value near 220 [ton] when b is larger than 130 [mm], which is the point where the steel begins to saturate. Despite this value, $b = 50$ [mm] was chosen mainly because

of the capacity of the available experimental testing equipment. Part (b) shows that the rate of change of the controllable force F_τ decreases as the current intensity increases, tending to saturation after 5 [A], which becomes the upper possible bound for experimental testing. The influence of damper velocity is summarized in part (c). The maximum force of the MR-damper does not increase substantially with the maximum piston velocity, which allows to have a rough estimation of the operational velocities at the design stage. With the parameters assumed in the simulation, in part (d) is shown that the nominally optimal gap size is 3.2 [mm], which is larger than the typical values used in practice. In this case, the maximum dynamic range value obtained from the results implies a very low controllable force, which is not desirable.

The MR damper proposed in this research has been numerically tested against other configurations to study possible improvements in future designs. The alternatives include varying the number of external coils, and incorporating diamagnetic rings at the ends of the cylinders to provide a better efficiency of the magnetic circuit (Figure 15). Therefore, four new models were analyzed and their f - v constitutive relationships obtained to compare results with the base configuration. Models (a) and (b) belong to a configuration with three and five coils respectively, model (c) includes one diamagnetic ring at each end of the external cylinder, and model (d) has diamagnetic rings at either of the external and internal cylinder ends.

While magnetic flux leaking through the head plates can be found in configurations (a) and (b), numerical results reveal that it is negligible in cases (c) and (d), which indicates that the diamagnetic layer on the external cylinder is enough to stop this leakage. Therefore, all magnetic flux crosses through the fluid gap, and models (c) and (d) result in more efficient models than (a) and (b), fact that is reflected in their maximum force values shown in Table 3. It should be noticed that the inclusion of diamagnetic components could be incorporated to any MR-damper in order to increase its capacity with minimum cost.

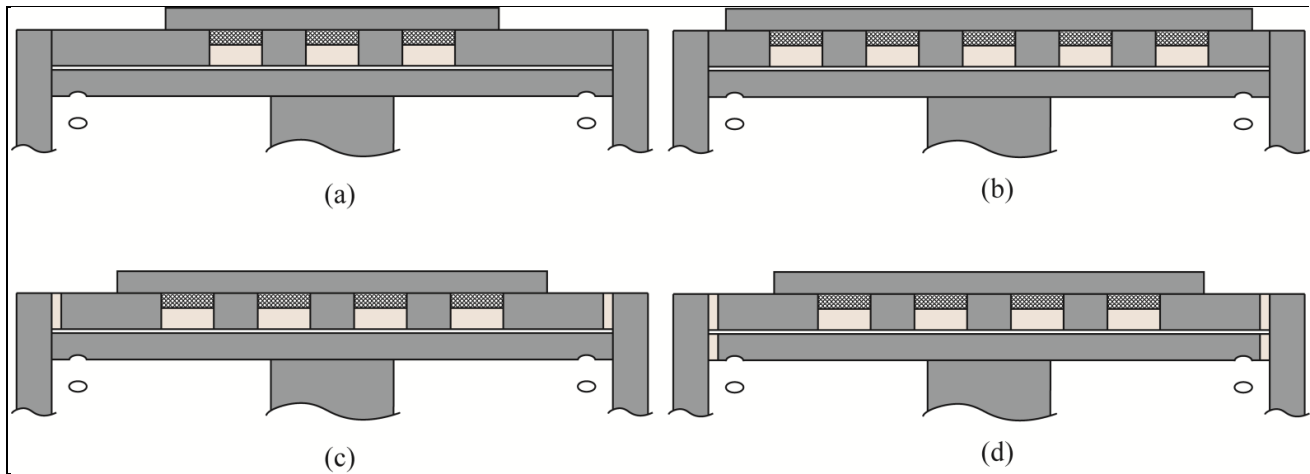


Figure 15. Geometry of the extra models to be compared with the proposed model: (a) Three coils; (b) Five coils; (c) Diamagnetic rings on the external cylinder only; (d) Diamagnetic rings in the external and internal cylinder.

Shown in Table 3 is the value of τ_{av} corresponding to the average yield stress representative of the fluid, which acts on the active length and was obtained from FE output. Results show that if the number of coils increases within a fixed length, the magnetic flux becomes more concentrated and the active length becomes smaller. Therefore, the total force can be substantially varied by modifying this parameter; for instance, if one more coil is added to the base system, the capacity may be improved in 24%. On the other hand, the capacity of the damper may be improved in approximately 10%, if the magnetic flux is efficiently directed and leaking is minimized.

Table 3. Summary of the comparative analyses

Model	Original model	(a) Three Coils	(b) Five Coils	(c) One diamagnetic ring	(d) Two diamagnetic rings
τ_{av}	23.43 [kPa]	17.75 [kPa]	34.41 [kPa]	26.56 [kPa]	27.74 [kPa]
F_{max} (CFX)	97.08 [ton]	91.98 [ton]	120.37 [ton]	106.52 [ton]	110.92 [ton]
Variation relative to base model	-	-5.25 %	23.99 %	9.72 %	14.26 %

2.7 Design, Manufacturing, and Testing of the real-scale MR-Damper

The finally selected design properties for the large-scale MR-damper are presented in Table 4. The damper has a nominal capacity of 97 [ton] and its design was based on the numerical model developed herein. This damper had to be modified to meet the requirements of the available experimental setup, which considers a maximum stroke of ± 200 [mm] and a capacity of 100 [ton]. Several pressure tests were run on the cylinder to assure its integrity due to the increase in the internal pressure expected in the fluid. As intuitively expected, one of the most challenging aspects of its design and construction was to achieve a safe bi-metallic configuration for the cylinder, which purpose was to induce the required magnetic circuit and minimize the magnetic flux leakage. A picture of the final product can be seen in Figure 16.

Table 4. Chosen parameters for the design of MRDA-UC

Design parameter	Dimension	Design parameter	Dimension	Design parameter	Dimension
Stroke	± 200 [mm]	Gap size, h	1.5 [mm]	Cyl. Length	640 [mm]
Piston radius	130 [mm]	Rod radius	35 [mm]	N° of coils	4
Coils width	60 [mm]	Spacing between coils, b	50 [mm]	Int. Cyl. Thickness	30 [mm]
N° of holes in internal cylinder	12x2	Internal cylinder holes diameter	20 [mm]	Head plates thickness	40 [mm]
Steel casing thickness	25 [mm]	Ext. cyl. thickness (steel)	41 [mm]	Ext. cyl. thickness (diamagnetic)	24 [mm]

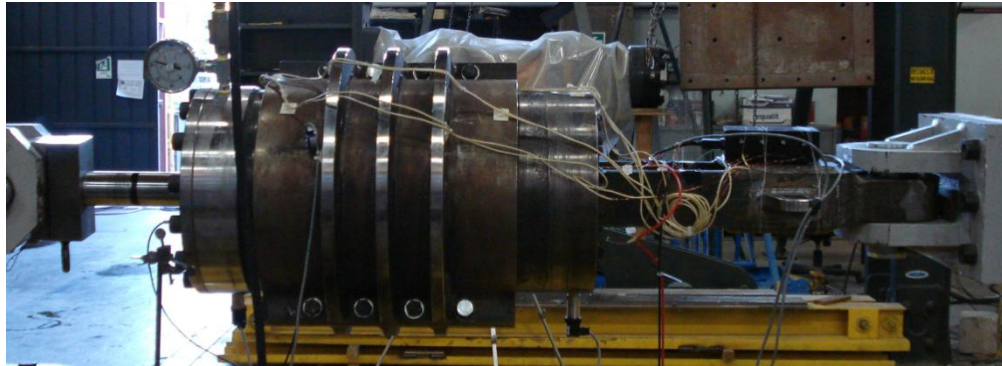


Figure 16. Picture of the final product of the MR-damper

A set of 23 proof-of-concept harmonic tests were performed on the real-scale MR-damper with different amplitudes, frequencies, and current intensities (Table 5). Each test was run at a constant current intensity value, which is consistent with the assumption presented for the cascade magnetic-fluid model used. The experimental force velocity f - v and force displacement f - δ relationships are shown in Figure 17; four groups of tests are plotted, each considering different current intensity values under the same velocity, or equivalently using the same combination of amplitude and frequency (Table 5). Please note that the last group was tested only to 2.5 [A], since the hydraulic pump of the actuator could not reach a better performance.

Table 5. Summary of the experimental tests performed to the real-scale MR-damper

Group of tests	(a)	(b)	(c)	(d)
Amplitude [mm]	10	60	100	140
Frequency [Hz]	0.48	0.212	0.21	0.19
Current intensities [A]	0-3	0-3	0-3	0-2.5

It is apparent from Figure 17 that, as it was expected for an MR damper, the change in maximum force is not strongly affected by the change in the maximum velocity. For the (c) group of tests, a dynamic range of 2.8 was measured; this value is lower than the expected value in the FE simulation due mainly to the higher measured friction and viscous forces. The viscous force is probably higher than the one predicted because of inaccuracies in the manufacturing of the fluid passage gap, and the turbulent flow around the inlet orifices toward the fluid gap, which is not included in the simulation model. All these details are being optimized and studied to improve the final damper design. In any case, results of Figure 17 prove that the scaling up of MR dampers is feasible and works, though some improvements are still needed related to the practical construction of the damper prototype.

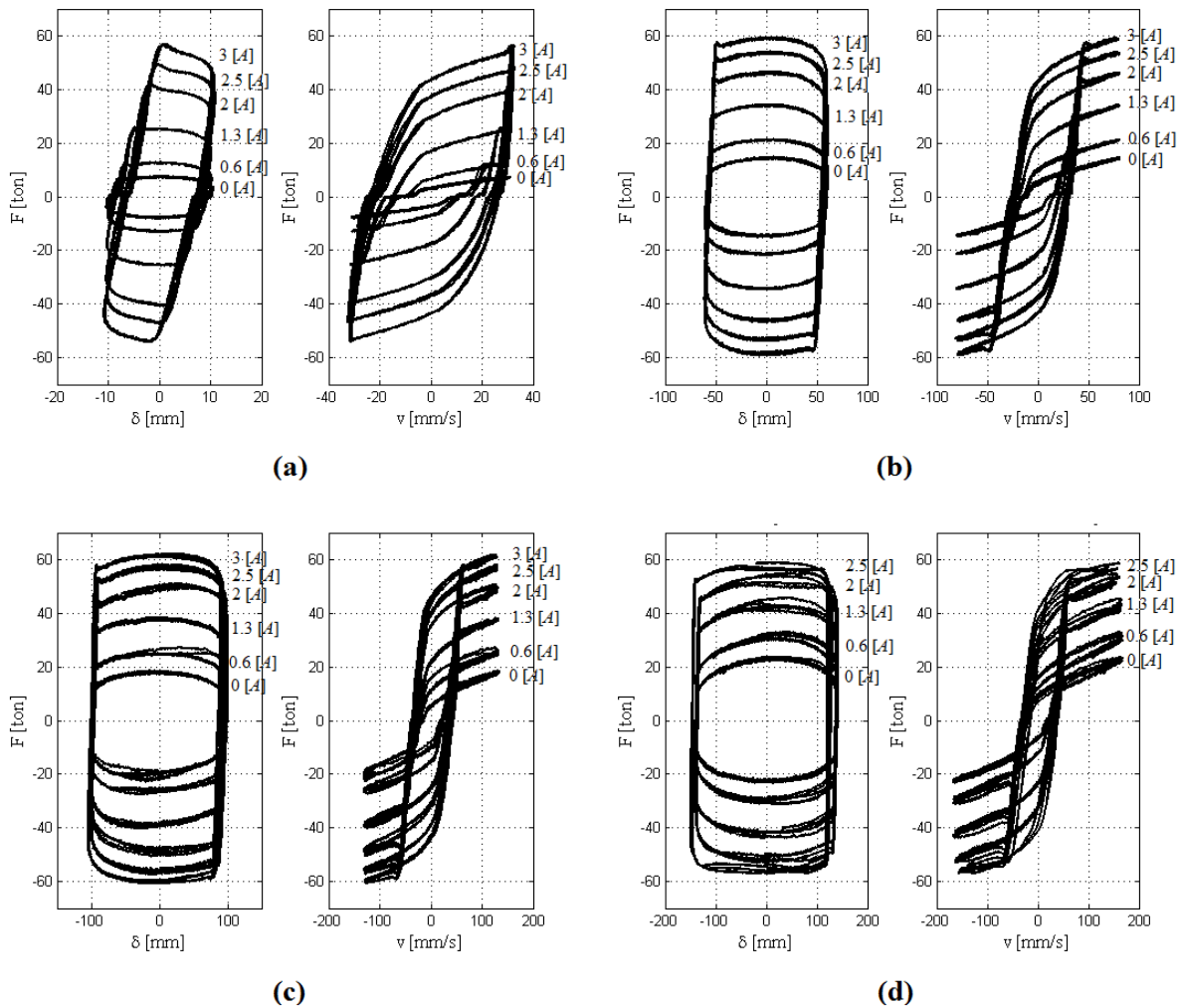


Figure 17. Measured f - v and f - δ constitutive relationships for different amplitudes and frequencies.

Shown in Figure 18(a) is an example of the pressure measured in both chambers, and the fluid temperature measured in one of the chambers during the test specified by an amplitude of $A = 100$ [mm], $f = 0.21$ [Hz], and current intensity $I = 2.5$ [A] (Test# 21). Temperature rose 10 [$^{\circ}\text{C}$] during the test, and due to the corresponding thermal expansion of the fluid, the average pressure in the damper rose by 7.3 [$\text{bar}/^{\circ}\text{C}$]. This value agrees well with the numerically estimated value of 8.6 [$\text{bar}/^{\circ}\text{C}$]. It can also be

seen that the temperature keeps rising after the last loop, which can be explained by a delay in the heating of the PT 100 temperature sensor with respect to the fluid, inserted in the damper through one of the head plates. On the other hand, while the pressure rises in one chamber it decreases in the other. In Figure 18(b), the damper force is obtained by simply multiplying the pressure difference by the piston area plus the measured friction force, which was estimated as 7.3 [ton]. This is a clear proof that the applied external force on the damper is in equilibrium with the force obtained by this pressure differences.

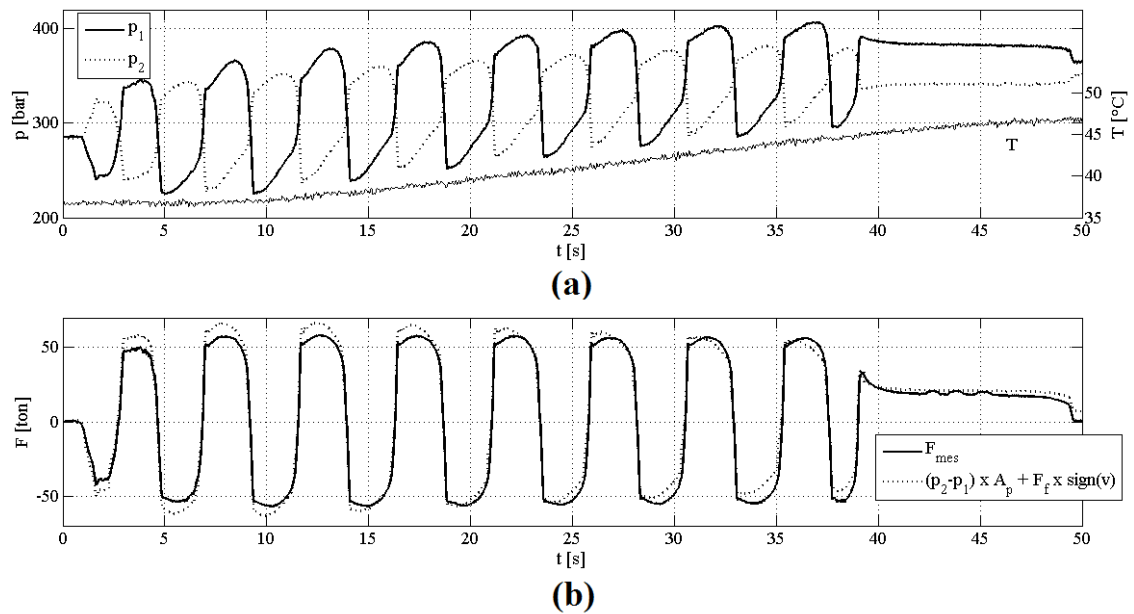


Figure 18. Test 21: (a) Measured pressure of both chambers & temperature; (b) Measured and calculated force by measuring the pressure difference between chambers.

2.8 Conclusions

This paper deals with the numerical simulation of the response of an MR-damper using a multi-physics FE model, which solves the magnetostatic and fluid problems as cascade systems. It has been shown in this article that the numerical boundary conditions imposed to the problem lead to a well posed numerical problem. The numerical solution of the magneto-static and fluid problems is coupled through the fluid viscosity, which depends on the magnetic field intensity.

It is concluded from the comparison between numerical and experimental results for a 15 [ton] damper that the capacity of an MR-damper with coils wound around the piston can be correctly predicted by the use of a FE numerical model like the one presented herein. The model was validated by using dynamic tests on a 15 [ton] MR-damper later implemented in the *Parque Araucano* building in Santiago, Chile. It is also true that the numerical simulation proposed that uses the Bingham model is not capable of representing the real hysteretic behavior observed in the MR-damper due to compressibility of the fluid. Even so, the maximum damper capacity and post-yield capacity differ in less than 0.5%.

The numerical model was also extended to help in the design of a prototype of a real-scale 97 [ton] MR-damper, which was manufactured and is being currently tested. The scaling of the device from 15 [ton] to 97 [ton] presented several design and practical construction challenges that have being mostly resolved but are still fine-tuned; the explanation of these details go beyond the scope of this article which purpose is mainly validate a design methodology through FE models. In any case, the critical construction aspects have been related to the proper confinement of the magnetic field to force this field to go through the MR-fluid, and the pressure increase in the fluid. The former was achieved by the use of a bimetallic cylinder. For the latter, since pressures inside the damper are significant and rise as the temperature in the fluid increases, a careful design of the joint between the two materials for the cylinder was considered. A

complete set of pressure tests have been considered to prove that this material joint works properly.

Numerical results have shown that the inclusion of diamagnetic components can actually improve the efficiency of an MR-damper. Also, as the number of coils increases in the damper, the capacity increases if the active pole length is kept constant. Furthermore, it is derived from parametric analyses that the spacing between coils is a critical design parameter due to its influence in the active length and the magnetic flux saturation within the fluid domain. These analyses also proved that the fluid saturates after a current intensity of 5 [A]; the dynamic range for the proposed configuration is smaller than the optimally predicted one due to the fact that the target force for the damper was larger and required a smaller dynamic range.

Initial test results on the large scale damper show that the concept of the external coil and other damper design aspects work in practice, but there are still several construction and model details that need to be improved in order to get a better agreement between the FE model simulations and the proof-of-concept experimental results in this case. There are several physical and practical explanations for these discrepancies, but they need to be studied further before a final conclusion can be achieved on how to correct them.

3. CONCLUSIONS

This research deals with the simulated response of an MR-damper using a FE model with cascade solutions of a magneto-static and fluid model.

It is concluded from the results that the force-velocity and force-deformation of an MR-damper with coils around the piston can be correctly predicted using FE numerical models coupling a magneto-static and a fluid dynamics problem. This conclusion has been validated by using a 15 [ton] MR-damper that was thoroughly tested dynamically and was later implemented at the *Parque Araucano* building in Santiago, Chile. It has also been proved that Yang's expression for the controllable force and the proposed method do not match well, resulting in a 30% error due to differences in the boundary conditions.

It is true that the analytical model is not capable of representing the complete hysteretic behavior observed in the experiments mainly because of the chosen model for simulation. Differences in numerical results occur because the model does not include the possibility of compressibility in the damper fluid. Even so, the maximum damper capacity and post-yield capacity err in less than 0.5%.

Results have shown that the inclusion of diamagnetic components can actually add efficiency to an MR-damper by improving its performance. It has also been shown that the number of coils has an impact in the maximum force if the active pole length is kept constant. Furthermore, it is deducted from parametric analyses that the spacing between coils is a crucial design parameter due to its influence over the active length and the magnetic flux saturation in the fluid domain. These analyses also proved that the system saturates after a current intensity of 5 [A] and that the maximum imposed velocity is not a key factor at an initial design stage. The dynamic range for the proposed configuration is out of the expected limits and it implies an unsatisfactory maximum force, mainly due to the viscous force, which it does not depend only on the fluid gap, but also in the internal cylinder orifices.

It is also concluded that the cascade effects of the magneto-static and fluid model can be used in the numerical solution of the coupled multi-physics theory characteristic of the MR-damper behavior. It has also been tested in this article that the numerical boundary conditions imposed lead to a well posed numerical problem. The most relevant implication of this result is that the numerical model presented herein is an alternative to be integrated as an effective tool in product design of larger-scale MR-dampers.

This research has also reached to the conclusion that the imposed flow boundary condition and a moving mesh technique agree very well when modeling fluid dynamics caused by a harmonic piston movement, as it can be seen in the appendices. Furthermore, fitting schemes used herein are also in good concordance when estimating the maximum force based on fluid dynamics modeling outputs generated by a coarse time interval. A moving average scheme is naturally better in the yield region than a linear fitting.

The manufacture of the damper, specifically the bi-metallic cylinder suffered of problems in its process, mainly caused by the unusual welding procedure between SAE 1045 steel and the diamagnetic material used. This procedure needs a special care on regulating temperatures, and it can easily derive in an unsatisfactory union between both materials, which imply an oil leaking through cracks generated in the union when submitted to internal pressure. The inclusion of pre-stressing bolts at both sides of the internal cylinder helped in relieving the axial stresses and therefore improved the performance of the welded joint. These problems were not predicted when a similar cylinder was tested, before the manufacture of the final prototype. This key aspect of the prototype needs to be redesigned in order to make our MR-damper economically attractive.

REFERENCES

- Guangqiang Yang. Large-scale Magnetorheological Fluid damper for Vibration Mitigation: Modeling, Testing and Control, 2001, PhD. Dissertation, Universtity of Notre Dame, Indiana.
- Rene Zemp. Tall Building Vibration Control Using a TM-MR Damper Assembly: Analytical Results, April 29, 2008, M.Sc. Thesis, Pontificia Universidad Catolica de Chile.
- Rene Zemp. Tall Building Vibration Control Using a TM-MR Damper Assembly: Experimental Results and Implementation, April 29, 2008, M.Sc. Thesis, Pontificia Universidad Catolica de Chile.
- Walid H. El-Aouar. Finite element based modeling of magnetorheological dampers, September 23, 2002, M.Sc. Thesis, Virginia Polytechnic Institute and State University.
- Spencer B F Jr, Dyke S J, Sain M K and Carlson J D. Phenomenological model of a magnetorheological damper, 1997, *J. Eng. Mech.* 123 230–8
- T. Butz. Modelling and Simulation of Electro and Magnetorheological Fluid Dampers, *ZAMM _ Z. Angew. Math. Mech.* 82 (2002) 1, 3—20
- L.A. Brigadnov. Mathematical modeling of magnetorheological fluids, *Continuum Mechanics and Thermodynamics* (2005) 17: 29–42
- Costa, Costa Branco. Continuum electromechanics of a magnetorheological damper including the friction force effects, *Sensors and actuators. A, Physical*, 2009, vol. 155, no1, pp. 82-88
- Chooi, Oyadiji. Design, modelling and testing of magnetorheological (MR) dampers using analytical flow solutions, *Computers and Structures* 2008 86(3-5): 473-82.
- Beverly, Tanner. Numerical Analysis of Extrudate Swell in Viscoelastic Materials with yield stress, Department of Mechanical Engineering, University of Sydney, Sydney, N.S.W. 2006, Australia
- LORD Corporation. Lord Technical Data, MRF-132DG Magneto-Rheological Fluid, Cary, NC, USA
- Lorenz, Fowler. Synchronous Generator Subtransient Reactance Prediction Using Transient Circuit Coupled Electromagnetic Analyses & Odd Periodic Symmetry, Kato Engineering Inc., North Mankato, MN
- Ansys Inc, Ansys 12.1 User's Manual, Canonsburg, PA, USA, 2009

Fujitani, Soda, Iwata. Dynamic Performance Evaluation of Magneto-rheological damper by Experimental and Analytical Method, *Proc. International Conference on Advances in Structural Dynamics*, vol. 1, Hong Kong, China, pp. 319–326.

APPENDICES

APPENDIX I: MODEL OF THE MR-DAMPER

Involving the simulation of the MR-Damper, the following models and tasks were developed: (i) a magnetostatic model; (ii) a fluid dynamics model; (iii) a viscous force simulation; (iv) a comparison between two different strategies for fluid dynamics simulation; (v) a fitting scheme for fluid dynamics model outputs with coarse time interval; (vi) a validation of the model based in an existent damper, and (vi) an estimation of the pressure raise due to heat generation.

Two different FE models are combined in order to achieve the constitutive relationships *force-velocity* ($F-V$) and *force-deformation* ($F-D$). The first one is the *Magnetostatic* model, which simulates the three-dimensional magnetic behavior of the damper, due to the electric current running through the coils. The second model simulates the dynamics of the fluid, using as an input the output of the previous model, since the viscosity properties of the fluid depend on the magnetic field strength, H . They are not simulated simultaneously because of computational requirements and the complexity to achieve such a model within the available software. The main objective of the simulation is to compare the model with experimental testing and use it as a tool for design. The tests are done under constant magnetic field conditions, and hence the magnetic field distribution does not vary in time, and it works as a constant input to the fluid dynamics simulation. Software used are: *Magnetostatic*, *ICEM CFD* and *CFX* applications of Ansys 12.1, for magnetostatic analysis, fluid mesh and fluid dynamics, respectively, and Matlab for output processing. Operative system used is Windows XP Professional x64 Edition.

The viscous force is also obtained with the help of Ansys *CFX*, by using a constant dynamic viscosity value instead of a magnetic field-dependent viscosity. This allows us to obtain information about the dynamic range of the modeled damper.

On the other hand, there are several strategies that can be selected when simulating the dynamics of a fluid. In this research two of them were taking into account: a moving mesh technique and an imposed flow strategy. The first simulates the movement of the

piston, while the second imposes a flow at an inlet with a velocity profile representing the velocity of the piston. These two strategies are compared, aiming to justify the use of the imposed flow condition.

In order to obtain soft curves from *CFX* models, an enormous amount of computing time is needed. Instead, a coarser time-step can be used, reducing the computing time, but resulting in outputs with oscillations around the exact value. This noise can be eliminated by fitting schemes, which are explained herein.

Finally, an estimation of the pressure raise in the fluid because of heating during one cycle of the movement of the piston is also done, since it affects the design of the steel components of the damper.

I.1 Magnetostatic Model

This model determines the magnetic field produced in a magneto-rheological damper due to the current that runs inside the coils that are installed inside of it. This simulation allows obtaining yield stress distribution on the fluid domain, necessary input when modeling the fluid flow.

The hypothesis states that a magnetic 3D model can be simulated in a reliable way, so the magnetic field produced by the coils inside the MR-damper can be correctly predicted, allowing us to have more available information to use in the magneto-dependent properties of the MR fluid. Main limitations are related to software simulation capacity and computational requirements.

The damper is made mainly with SAE 1045 steel, but it also has components made from a diamagnetic material that act as isolators to force the magnetic flux to be directed where it is needed, the gap between both cylinders, where the fluid goes from one chamber to another. The fluid used is Lord MRF 132-DG, which is a magneto-rheological fluid and hence, its dynamic properties change in presence of a magnetic field.

Lord fluid and SAE 1045 steel are materials with non-linear magnetic behavior. Their magnetic permeability is not constant, and the relationship between magnetic flux density B and magnetic field strength H is given by a magnetization curve (B - H curve) specified by their respective manufacturers. In Figure 3 the B - H curves for Lord fluid and SAE 1045 steel were shown respectively. The diamagnetic material, however, has an absolute permeability very similar to the air (relative permeability close to 1).

In terms of geometry, the configuration of the MR-damper consists of four coils coiled up externally to the damper. They are located in a cylinder external to the fluid chambers and, although they are not in direct contact with the fluid, they can affect its dynamic properties thanks to its design. This configuration allows the coils to be intervened without disassembling the entire damper. It also benefits computational simulation, as the magnetic field does not change through time, since the coils are not in the piston. In other words, if a constant current runs through the coils, spatial distribution of the magnetic field will be constant through time, which simplifies the simulation and makes it more reliable. In Figure A.I 1, a photographic sequence of the model is shown.

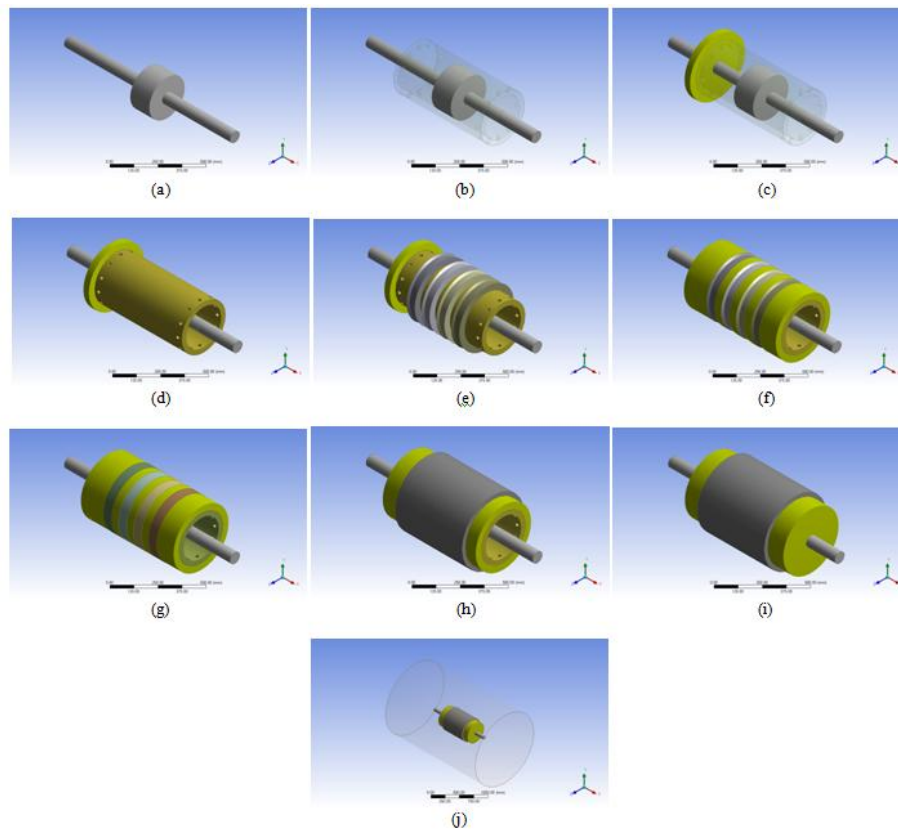


Figure A.I 1. Photographical sequence of the geometry in *Magnetostatic* model

In this configuration, there is no gap between the piston and the internal cylinder; therefore no fluid can cross from one chamber to another through there. Then, the only possible way for the fluid to transport between chambers as the piston moves is through 12 holes made at both extremes of the surface of the internal cylinder, which connect both chambers to the 1.5 [mm] gap between the internal and external cylinders. A schematic view with dimensions in [mm] can be seen on Figure A.I 2.

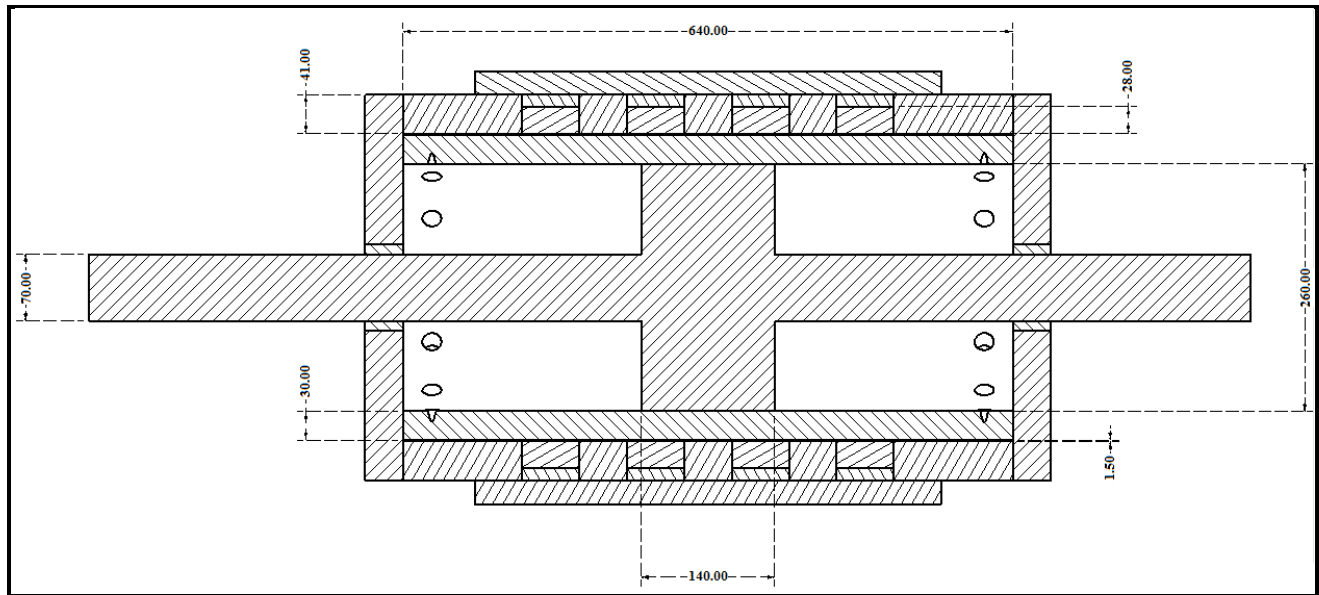


Figure A.I 2. Schematic view of the MR-damper (Dimensions in [mm])

Finite elements have been modeled with *solid117* Ansys element, which can be seen in Figure A.I 3 and has been created to simulate magnetic fields in three dimensions. It is defined by 20 nodes; it has 12 degrees of freedom for magnetic flux (one on each intermediate edge node). The eight vertex nodes have the last DOF's for electric potential. This element applies, in general, for magnetic field analysis with low frequency and they can simulate $B-H$ curves for transient and static analyses. The mesh of our configuration was already shown in Figure 5 (a).

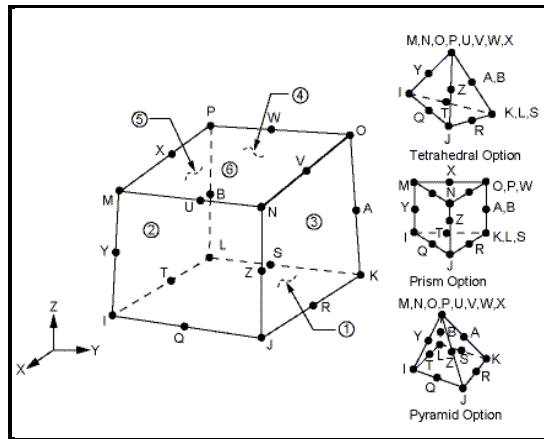


Figure A.I 3. *Solid117* element

There are two types of boundary conditions for this model. First, zero voltage is applied in the external surfaces of the air chamber, simulating service conditions, which is shown in Figure A.I 4. The other corresponds to the source that generates the magnetic field, which is given by the 3 [A] electric current that runs inside each coil in opposite directions, shown in Figure A.I 5. Each coil consists of 250 turns of copper wire. The blue regions represent the coils, and the red arrows show the direction of the current flow. The analysis reaches 3[A] in 0.1[s], with intervals of 0.01 [s]. The convergence is based in CSG method, which has been explained in chapter 2. The time of convergence for this model was 9,822 [s].

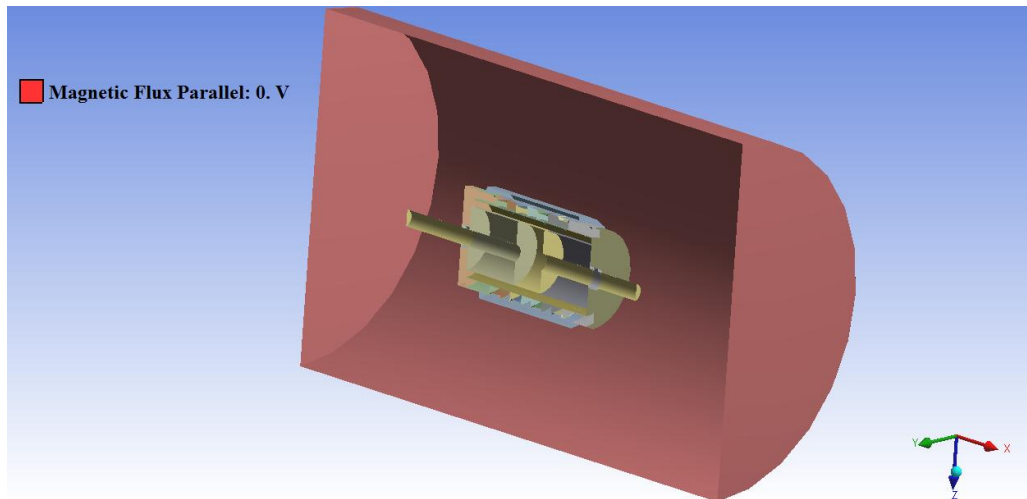


Figure A.I 4. Boundary condition: Magnetic flux parallel

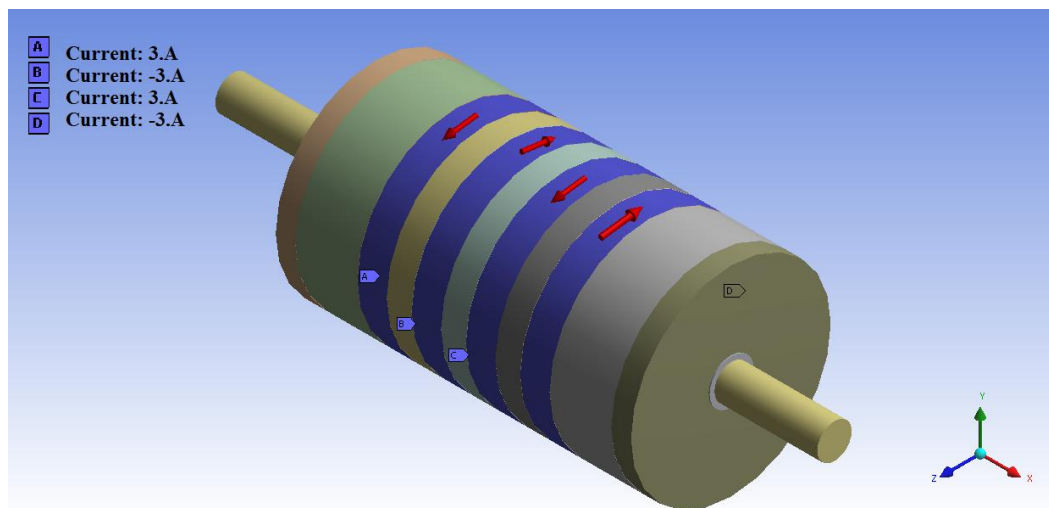


Figure A.I 5. Boundary condition: Electric current on each coil

Several outputs can be obtained from this model. The most important result for our purposes is the magnetic field strength H , because the fluid yield stress depends on this parameter. But magnetic flux density is also important when designing steel thicknesses. A colored plot showing results for H in the fluid gap domain was shown in Figure 8. Its maximum value is obtained in the zones between coils, but not in the center zone as it was expected. On those zones the maximum reaches 403 [kA/m] and the average value surpasses the yield stress saturation limit of 300 [kA/m].

Arrows representing the value of B on the external cylinder can be seen in Figure A.I 6, which shows the radial flux around each of the four coils. For one coil, radial flux at both of its sides is influenced by the coils adjacent to it. As expected, the flux density at the extremes of the cylinder is weak, since the flux has more cross area to be spread and it is affected only by one coil. Values of B for the center region have been plotted in Figure A.I 7. Because of its direct relationship with H , it is natural that in the center region, B values result smaller than in the other regions as well. Comparing these results with the B - H curve for SAE 1045 steel it can be noticed that the steel is not saturated.

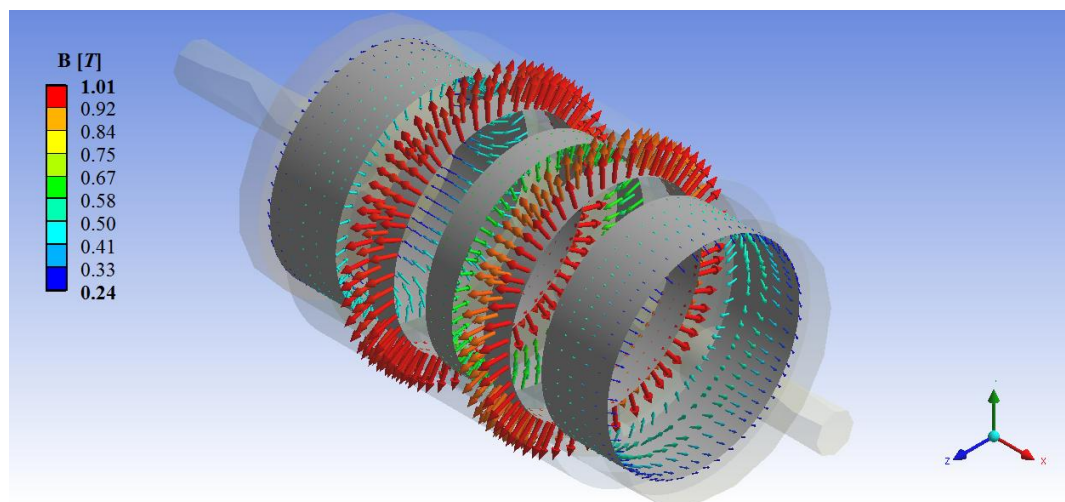


Figure A.I 6 Arrows diagram of the radial magnetic flux densities over the external bi-metallic cylinder

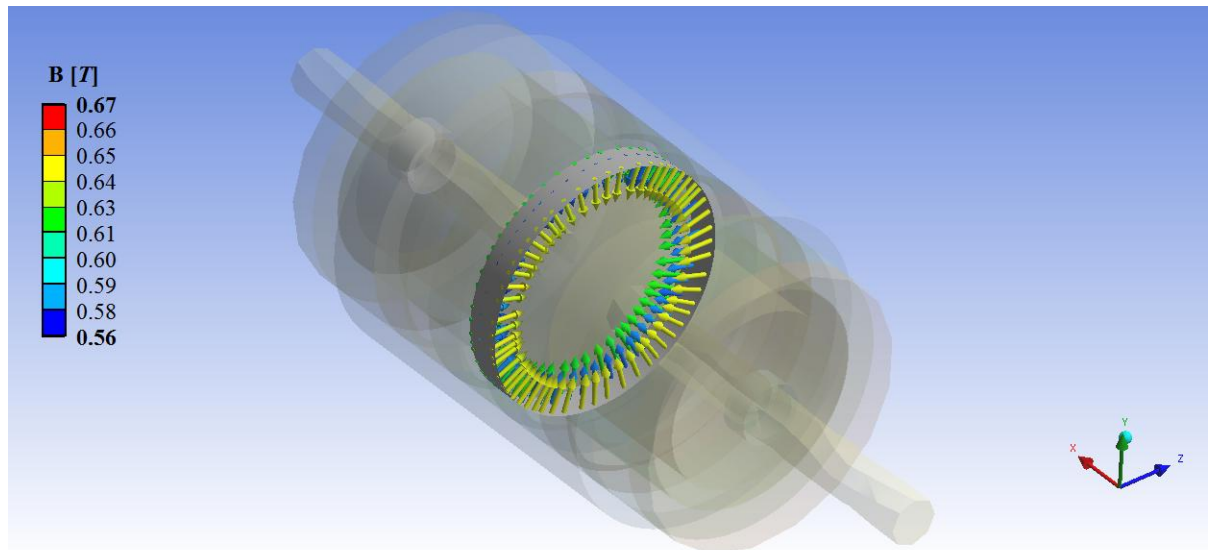


Figure A.I 7. Arrows diagram of the radial magnetic flux densities over the central region of the external bi-metallic cylinder.

Finally, absolute values for total magnetic flux around each coil are presented on Figure A.I 8, where it is shown that the coils located at both extremes of the configuration present a greater magnetic flux than the ones located at the center. The values are shown in $[Wb] \cdot 10^{-2}$.

The fluid yield stress exported to *CFX* model is obtained after processing the results in Matlab, by using the curve $\tau_0 - H$ specified by the manufacturer, and it is shown in Figure A.I 9. The region of the fluid gap is what concerns, since the fluid on both chambers has a negligible yield stress. Red zones corresponds to saturated fluid, i. e. regions of fluid with $\tau_0 = 48.32 [kPa]$.

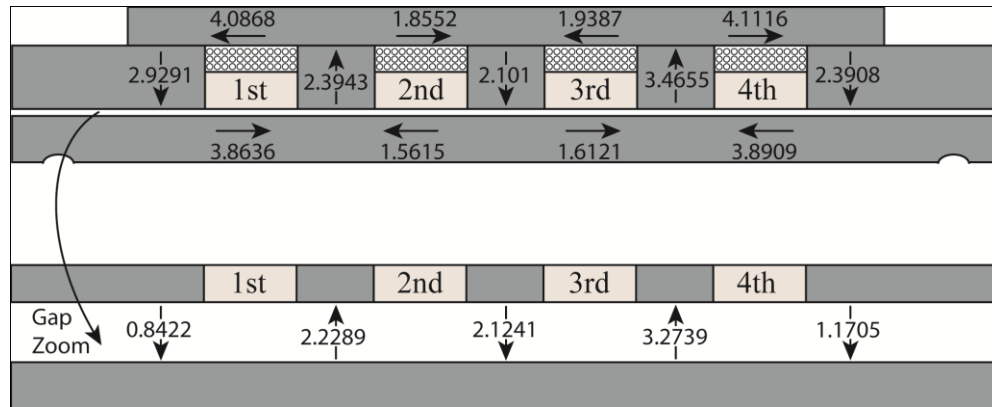


Figure A.I 8. Magnetic flux values around each coil

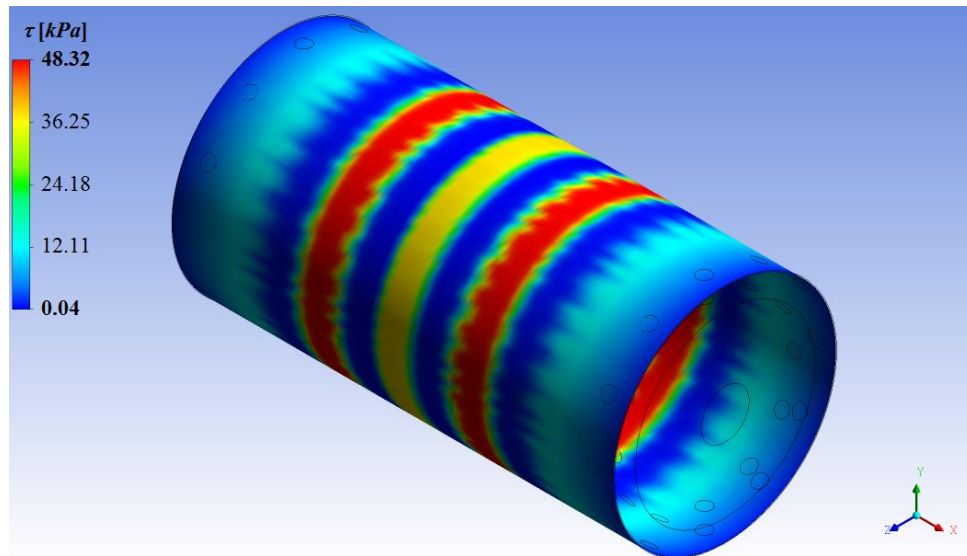


Figure A.I 9. Yield stress distribution obtained from *Magnetostatic* model and processed with Matlab, to be used as an input of the fluid dynamics model.

I.2 CFX Model of a Magneto-rheological Damper

The fluid dynamics are governed by Navier-Stokes equations (Table 2). The fluid to be used is a *non-newtonian* fluid, and it can be modeled as a *Bingham fluid*. Interaction between magnetic field and fluid behavior occurs in two variables on *Momentum equations* of Table 2. First, the body force is taken as the *Lorentz* force produced by the magnetic field. But the stronger interaction can be seen in the dynamic viscosity model, since it depends on the shear strain rate and the yield stress present in the fluid domain. This situation turns the model into a non-linear one.

Several investigations have proven that MR fluid can be well modeled by using the *Bingham* model, which is schematically presented on Figure A.I 10 and states that the fluid will flow only after its yield stress has been surpassed. Before that happens, it behaves as a semi-solid. It has to be remembered that, in order to implement this model in the *CFX* simulation, it is necessary to implement the scheme proposed by Beverly & Tanner.

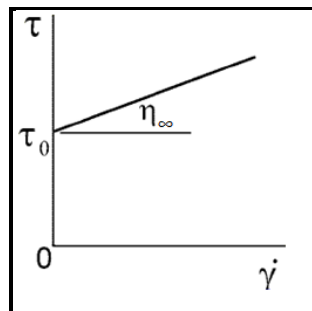


Figure A.I 10. Representation of the Bingham model

This model predicts the total force that the MR-damper can develop, by simulating the fluid dynamics at its inside to predict the constitutive relationship *F-V* for a given

sinusoidal movement of the piston. Once the movement has been modeled, the pressure on piston walls can be integrated, since the total force is given by the pressure difference between chambers.

Piston movement simulation requires a moving mesh technique on the fluid domain, since the volume it occupies changes its geometry with time. An alternative is to impose an inlet of fluid at one side of the damper, following the same movement characteristics, i.e. with a sinusoidal velocity profile. This alternative is the one to be used and will be further justified.

Characteristics of the fluid have already been discussed and all of its properties are defined in Appendix II. To model the fluid it was necessary to simulate a cut of the full domain, taking rotational periodicity into account. Then, only one twelfth of the domain was modeled, taking special care on boundary conditions. This simulation only works with fluid domain, which corresponds to the space that is filled with fluid inside the MR-damper, i.e. steel and bronze elements are not included in the model. In Figure A.I 11 a full domain is shown. There can also be seen a longitudinal cut of the full domain in order to have a better understanding of the domain. The one twelfth portion modeled in this investigation is shown in Figure A.I 12

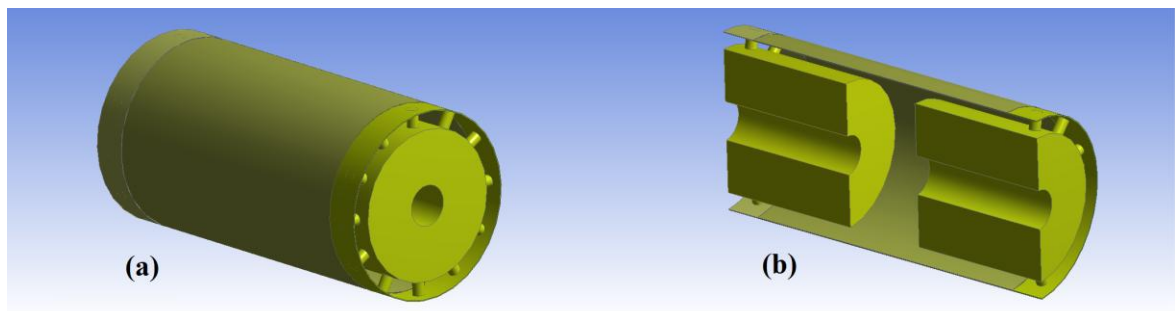


Figure A.I 11. Full fluid geometry. (a) Initial view, (b) Longitudinal cut

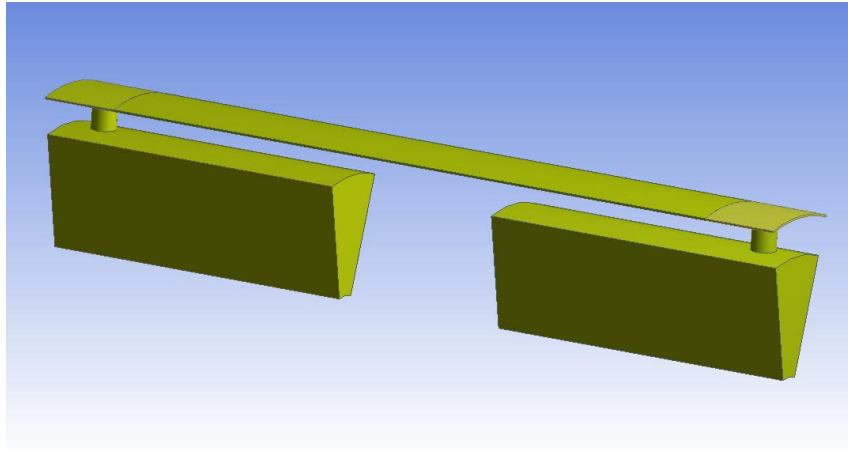


Figure A.I 12. *CFX* model geometry

The model was meshed using the *ICEM CFD* application of Ansys 12.1 and consists of hexahedral elements. The total amount of elements and nodes are 520,456 and 553,434 respectively (Figure 10). The gap is meshed separately from the rest of the domain, as it needs at least five layers of regular elements in order to obtain an accurate velocity profile in it.

Boundary conditions are related with the characteristics of each wall of the fluid domain. They are given by stationary or moving walls, slip or no-slip walls, inlets, openings and fluid-fluid interfaces. Border conditions of this model are defined below.

- *No-slip wall*: Every velocity component of the fluid is null. However, if a velocity condition is applied, velocity components of the fluid are equals to surface velocity.
- *Unspecified surface*: In moving meshes, used for surfaces whose movement is *a priori* unknown, but must accommodate to other surfaces specified movement. The software decides their movement.

- *Inlet*: An inlet boundary condition is used where the flow is predominantly directed into the domain.
- *Opening*: An opening boundary condition allows the fluid to cross the boundary surface in either direction. A reference pressure must be determined.
- *Interface fluid-fluid*: If the flow field is repeated in multiple identical regions, then only one region needs to be solved, but the boundaries are specified as periodic (via rotation or translation). In this case, a rotational periodicity is needed.

Imposed flow model works on the basis of an inlet and an opening shown in Figure A.I 13. At the inlet, the sinusoidal velocity profile in Eq. (1) is specified, where v_0 is the maximum velocity of the excitation, with a value of $0.17 [m/s]$; ω corresponds to the angular frequency of the excitation, which has been chosen as $10 [rad/s]$ under the assumption that the total force is independent on the frequency if the maximum velocity is kept constant; and t represents time. The opening is characterized by a relative pressure of $0 [Pa]$. Surfaces at both sides of the domain, shown in Figure A.I 14, are characterized by a fluid-fluid interface with rotational periodicity. The rest of the surfaces have a no-slip wall boundary condition.

$$v_{fluj0,x} = v_0 \sin(\omega t) \quad (3)$$

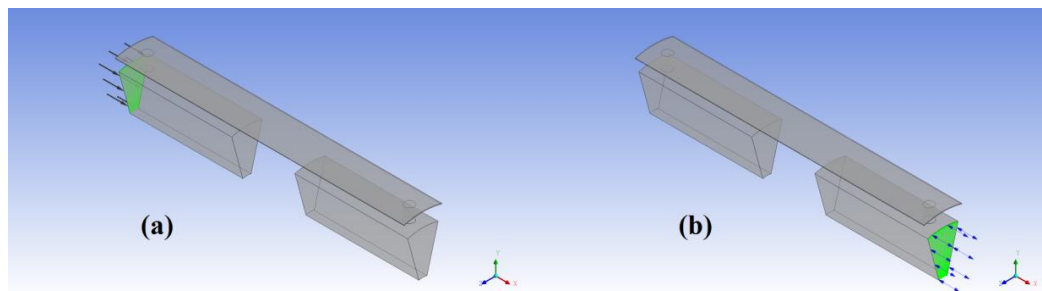


Figure A.I 13. Imposed flow model conditions. (a) Inlet, (b) Opening

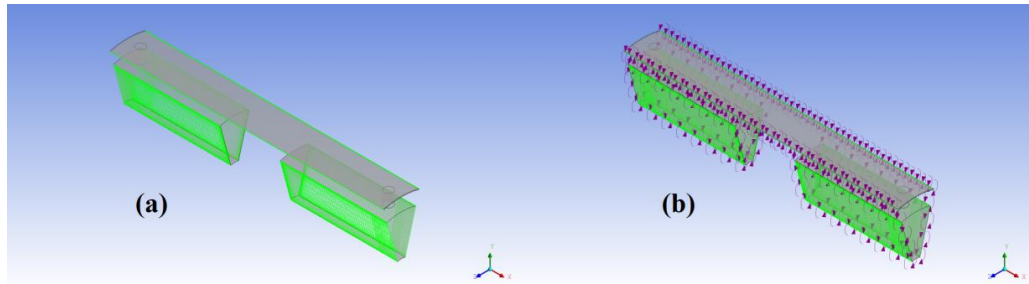


Figure A.I 14. Fluid-fluid interface. (a) Periodic interface, (b) Periodicity about x-axis

Regarding the set up of the mathematical model, according to Beverly & Tanner, the fluid is modeled as a *Newtonian* fluid with a field dependent dynamic viscosity shown in Eq. (2) (Beverly, Tanner, 2006):

$$\eta(\dot{\gamma}, H) = \begin{cases} \frac{\tau_0(H)}{\dot{\gamma}} + \eta_\infty, & \dot{\gamma} \geq \dot{\gamma}_0 \\ \alpha\eta_\infty, & \dot{\gamma} < \dot{\gamma}_0 \end{cases} \quad (4)$$

where, η_∞ is 0.092 [Pa-s]; α is a non-dimensional parameter and has been chosen as 10000; $\tau_0(H)$ [Pa] corresponds to the fluid yield stress read from *Magnetostatic* model; $\dot{\gamma}$ [1/s] is the shear strain rate of the fluid; and $\dot{\gamma}_0$ [1/s] represents the critical shear strain rate, obtained by $\tau_0(H)/[(\alpha-1)\eta_\infty]$.

A transient analysis is performed for a quarter of a cycle, i.e., with a final analysis time t_f equal to 0.157 [s] with a time interval given by $\Delta t = 5 \cdot 10^{-4}$ [s], and applying a filter scheme to eliminate the noise of the results given by the chosen time interval. A filter would not be necessary if the time-step is reduced to less than $5 \cdot 10^{-6}$ [s], but it would require a lot of computational effort. This scheme will be further explained in this appendix. As a monitor parameter, the longitudinal force exerted upon piston walls is calculated by integration, and shown while the solver runs the simulation. Please note

that this monitored force corresponds to only a twelfth of the full domain. This monitored force can be seen in Figure A.I 15. The unit is in $[N]\cdot 10^{-3}$.

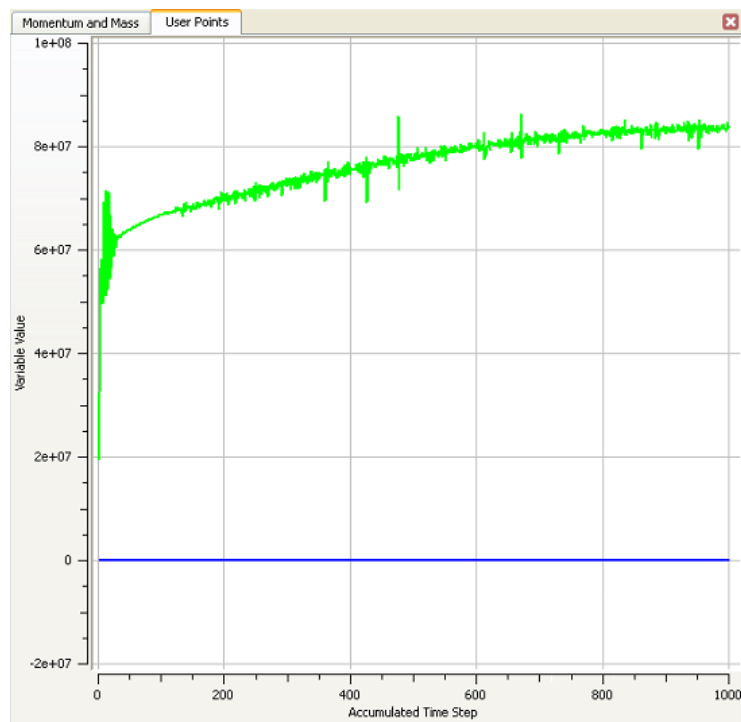


Figure A.I 15. Monitored force

To control the accuracy of the simulation, four RMS values are calculated. RMS stands for *Root Mean Square* and is a measure of how well the solution converges. They correspond to the residuals for each equation at the end of each time-step. A reasonably converged solution requires a maximum residual level no higher than $5\cdot 10^{-4}$, but in our setup a maximum of $1\cdot 10^{-4}$ is required for accuracy. Typically, the RMS residual will be an order of magnitude lower than this. If the RMS values do not reach that limit, simulation continues to the next time-step after 10 iterations. The measured RMS values are: RMS P-Mass (residual for continuity equation), RMS U-Mom (residual for

momentum equation in u direction), RMS V-Mom (residual for momentum equation in v direction) and RMS W-Mom (residual for momentum equation in z direction) (Ansys Inc, 2009). Convergence for this model can be seen in Figure A.I 16.

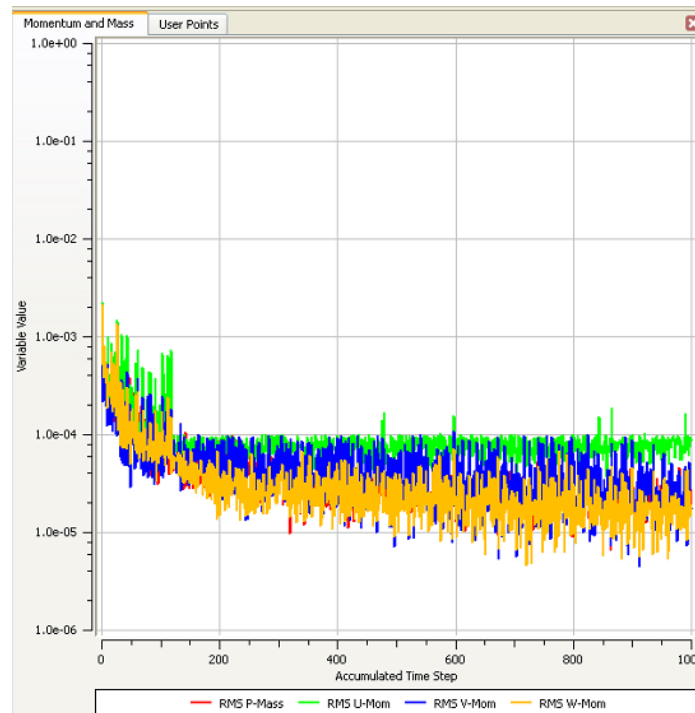


Figure A.I 16. RMS values for *CFX* model

After running the simulation, the total force of the damper can be calculated by integrating the total x-force on piston walls. Then, constitutive relationships $F-V$ and $F-D$ can be obtained, which were shown in Figure 11(a) and (b) respectively. $F-V$ curve naturally follows the shape of the *Bingham* model, and it does not consider hysteresis. Moreover, it is very close to a rectangle, the shape of a frictional damper. The noise presented in the output is given by the values of the parameters chosen for the fitting scheme which is, in this case, based on the average of intervals of length of 5 elements

in the data obtained from the *CFX* output. Maximum capacity for the given values of frequency and maximum velocity is 97.08 [ton].

I.3 Viscous Force

Ansys *CFX* software is also used to predict the viscous force of the damper. This quantity has a direct influence on the dynamic range D of MR-dampers, which will be further defined. In this case, the fluid is represented by its properties in absence of a magnetic field, i.e., with a constant dynamic viscosity, $\eta = 0.092$ [Pa·s]. The geometry and boundary conditions are the same as for the *CFX* model explained above as well as the maximum velocity of 17 [cm/s]. The computing time using four processors was 1.22 [hrs]. In Figure A.I 17 the relationship *viscous force – displacement* and *viscous force – velocity* are shown. A maximum of 2.17 [ton] has been obtained for F_η . The analysis considers only the first cycle of the piston movement.

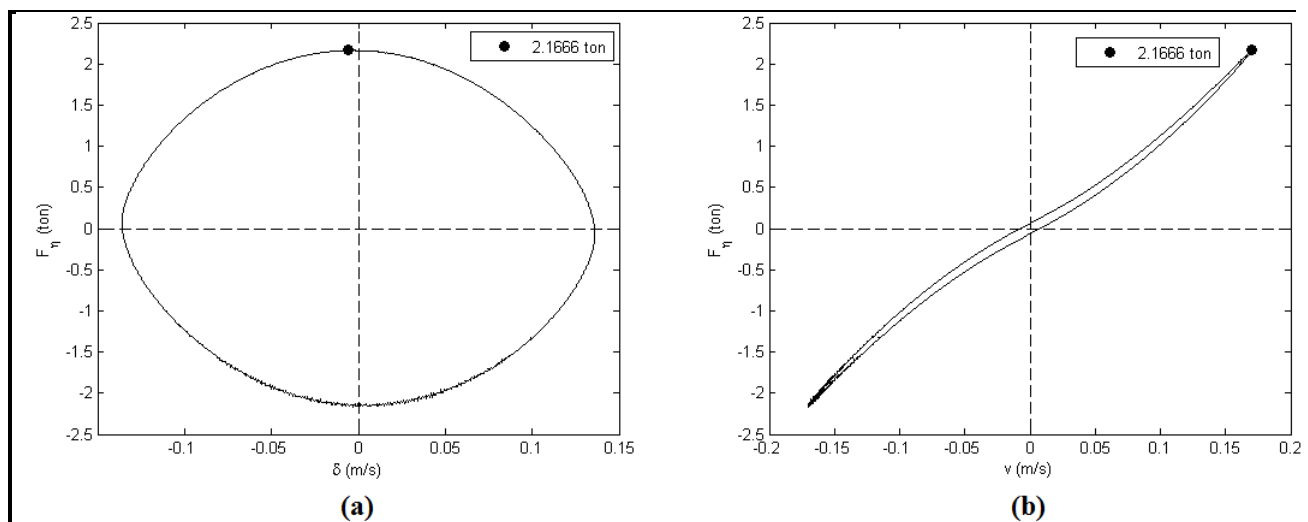


Figure A.I 17. Viscous force predicted by *CFX* Ansys software. (a) Relationship with displacement; (b) Relationship with velocity

By subtracting these results to those of the total force previously obtained, the controllable force can be computed, and it has a value given by $F_{\tau_{max}, CFX} = 93.33$ [ton] when $v_0 = 17$ [cm/s]. The dynamic range D is defined as the ratio of the controllable force F_{τ} and the uncontrollable force $F_{\eta} + F_f$. The friction force F_f is a constant value and it can only be measured when testing. A typical assumption is that $F_f = F_{\eta}$, and then $D = 21.5$. The influence of gap variation in the viscous force (and hence, in the dynamic range) has been studied and it is presented on Appendix III.

I.4 Comparison between moving mesh and imposed flow

To validate the imposed flow method, two models sharing the same configuration were done, a model using this scheme, and one consisted on a moving mesh technique. The $F-D$ and $F-V$ curves were compared and the quadratic error from the $F-D$ curve was obtained. The geometry used to do this validation consisted in the same as the one shown in the paper, but with changes in some parameters, since it was made before the final design was established. Its parameters can be summarized in Figure A.I 18.

Boundary conditions for the imposed flow method are the same as usual, except for the values of v_0 and ω , which are 0.25 [m/s] and π [rad/s] respectively, and the viscosity of the fluid, which was taken as $\eta = 0.092$ [Pa·s], for simplicity. Boundary conditions for the moving mesh technique are related with the movement of the walls. All walls are defined as *no slip walls*, but only the piston walls have a specified sinusoidal displacement. Walls whose movement depend on the movement of the piston to accommodate to the new geometry, as internal cylinder walls and rod walls, have an *unspecified mesh motion* with a condition of *wall velocity relative to mesh motion*.

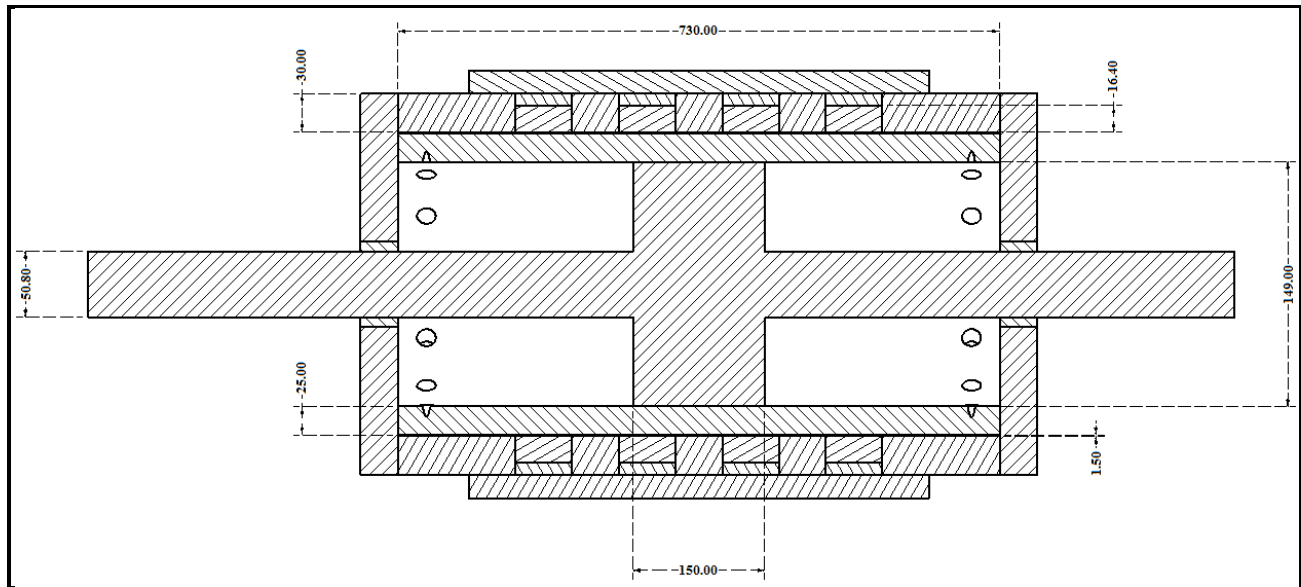


Figure A.I 18. Schematic view of the MR-damper for comparison between moving mesh and imposed flow methods

The results of the comparison can be seen in Figure A.I 19, where $F-D$ and $F-V$ curves for both methods have been plotted. Visually, there is a minimal difference, and numerically the average percentage error between both curves is given by 4.3%, and the maximum error is 30.14%, due to differences of convergence for the initial time-step for both methods. These percentages are estimated with respect to the curve obtained by the *moving mesh* method. It is then concluded that an imposed flow boundary condition can be applied instead of a moving mesh method when it is necessary to save computing time.

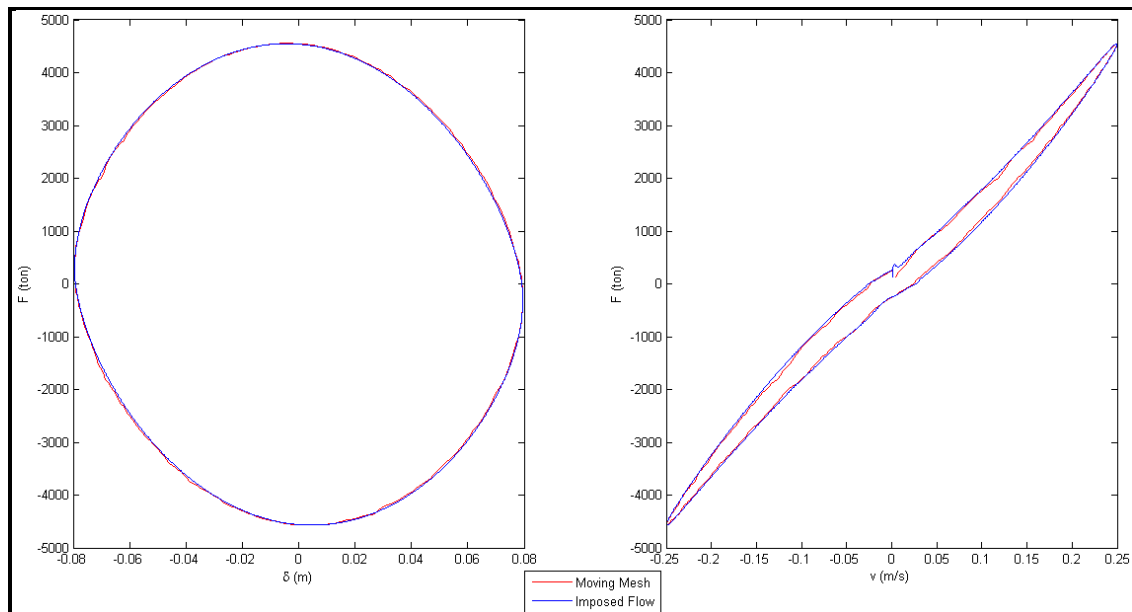


Figure A.I 19. F - D curves comparison for moving mesh and imposed flow methods

I.5 Fitting of Curves for *CFX* Model Outputs

The goal of this section is to prove the accuracy of the approximations done to the results in *CFX* model when they have a coarse time interval. In our models, a time interval dt of at least $1 \cdot 10^{-6}$ [s] is required to obtain good results, which still have some noise at the beginning of the simulation, specifically in the transition region where the yield stress is surpassed. This time interval consumes a great amount of computing time. Instead, $dt = 1 \cdot 10^{-4}$ [s] is used, which results in an unstable F - V relationship that oscillates around a definite average value. This result is then approximated by a linear fitting, which is compared to a model that was run using a time step of $1 \cdot 10^{-6}$ [s].

Geometry, *FE* model, and boundary conditions are the same in every model presented in this section, and correspond to those of the *CFX* model explained above. The flow enters the domain with the velocity profile given by Eq. 1. The parameters to

be varied are, then, ω , v_0 and the time interval, dt . First, a model using a fine time interval was done. The properties of the model are given by $\omega = \pi$ [rad/s], $v_0 = 25$ [cm/s] and $dt = 1 \cdot 10^{-6}$ [s]. The resulting F - V curve is shown in Figure A.I 20. It took 300 [hrs] of computing time (or 12.5 days). Maximum force obtained is 83.71 [ton].

Now, the same model, but this time changing the time interval to a coarser one, is run. The properties for this case are $\omega = \pi$ [rad/s], $v_0 = 25$ [cm/s] and $dt = 1 \cdot 10^{-4}$ [s]. The result obtained can be seen on Figure A.I 21. It is a clearly unstable result, but it seems to oscillate around a definite average value. A maximum force cannot be obtained easily and that allows performing a regression in order to predict a *force-velocity* relationship consistent with the one obtained in Figure A.I 20 .

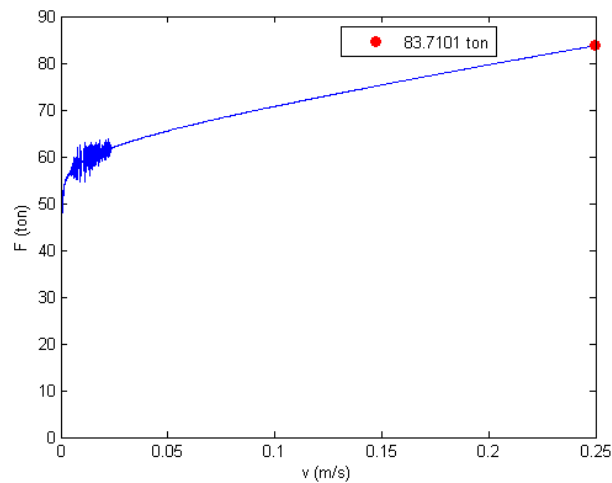


Figure A.I 20. F - V curve obtained with CFX and $dt = 1 \cdot 10^{-6}$ [s]

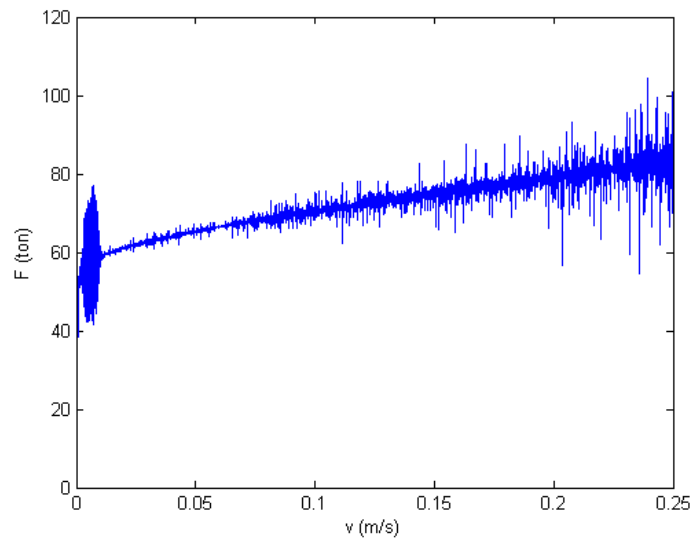


Figure A.I 21. F - V curve obtained with CFX and $dt = 1 \cdot 10^{-4}$ [s]

A linear approximation, fitting the curve corresponding to Figure A.I 21 can be seen on Figure A.I 22. It gives a maximum of 83.69 [ton] when the velocity reaches its maximum value. This approximation consists simply on doing a linear regression, in the least-squares sense. The problem with this scheme is that it does not predict well the behavior in the yield region. In order to do that, another fitting scheme should be used.

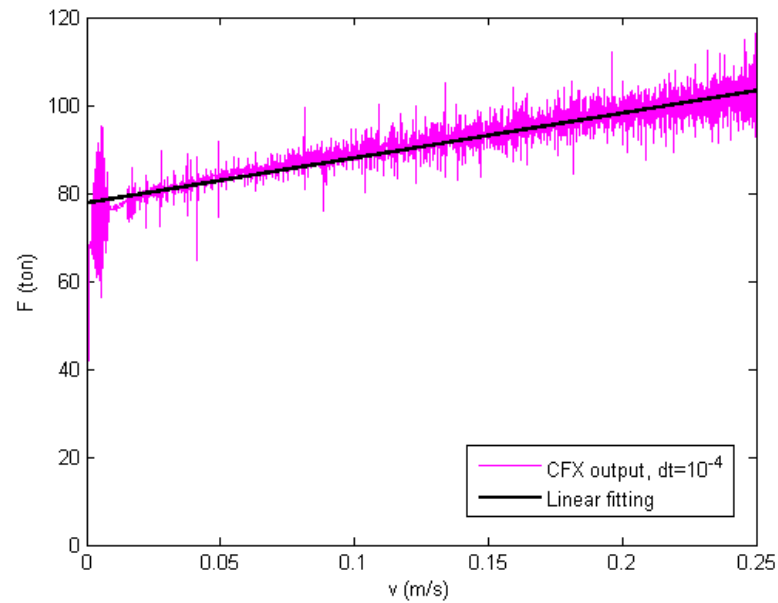


Figure A.I 22. Linear approximation of F - V curve obtained with CFX and $dt = 1 \cdot 10^{-4}$ [s]

A second fitting scheme was also done. Taking into account that the time interval is small, the average value of a group of m points was taken. The regression is then compared to the CFX initial output and the linear approximation. For example, if $m = 50$ points, groups of 50 values are taken from the coarser model, and their average value is then calculated (see Figure A.I 23). It leads to a maximum of 83.45 [ton]. This scheme has the advantage that gives a better idea of the behavior around the yielding zone.

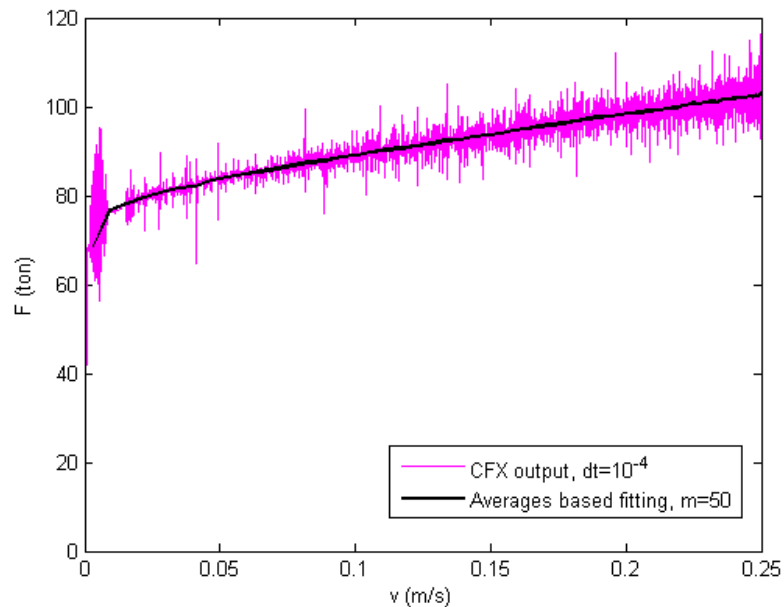


Figure A.I 23. Approximation based on interval averages of F - V curve obtained with CFX and $dt = 1 \cdot 10^{-4}$ [s]

A visual comparison between both schemes and the CFX model with fine time-step can be seen in Figure A.I 24. The linear regression predicts the maximum value better than the interval average approximation and it gives a good prediction of the behavior after the fluid has yielded, but the latter gives a better idea of what happens when t is small. The objective is then accomplished, if it is noticed that a refined model which takes 300 hours of computational time can be well approximated by running a coarser model, and then applying fitting methods. This process takes 17 hours using eight processors, which corresponds to a 5.67% of the initial computational time. The error in obtaining the maximum force with each of the fitting schemes can be seen on Table A.I 1, where it is clear that either of both schemes is reliable for predicting the CFX convergence value when calculating the total force of the damper, being the linear approximation more accurate than the other scheme.

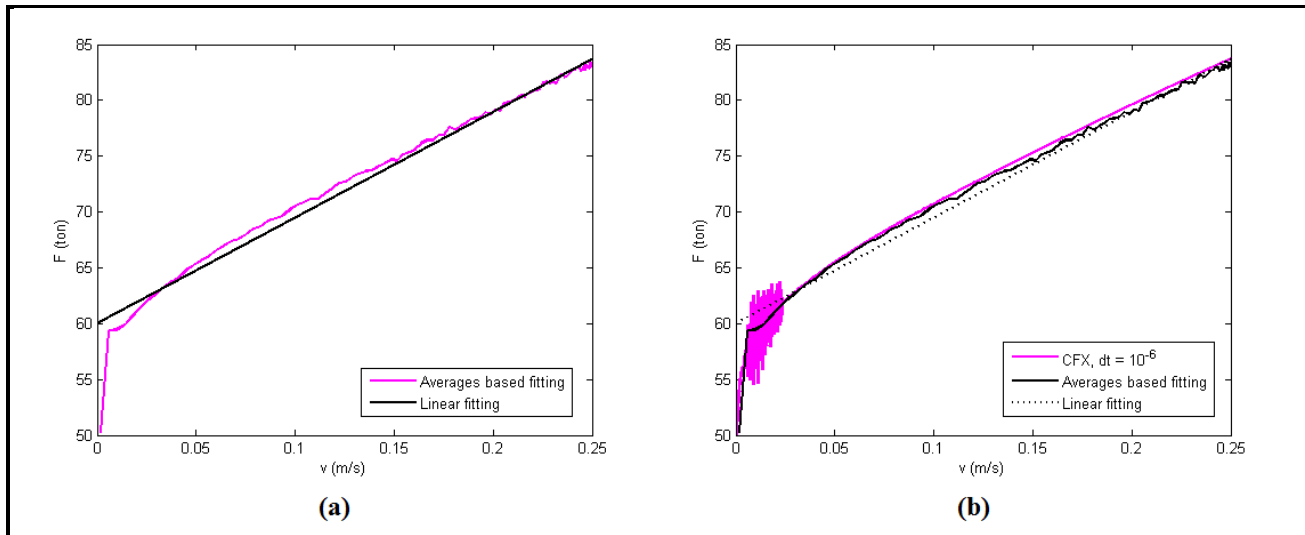


Figure A.I 24. Fitting schemes comparison. (a) Both fitting schemes together; (b) Along with *CFX* F - V curve with $dt = 1 \cdot 10^{-6}$ [s]

Table A.I 1. Error when predicting total force with respect to the refined *CFX* model

Fitting scheme	Maximum Force	Error w/respect to refined model
<i>CFX</i> $dt = 1 \cdot 10^{-6}$ [s]	83.7101 [ton]	0 %
Linear	83.6976 [ton]	0.0149 %
Interval averages	83.4501 [ton]	0.3106%

I.6 Validation of the model using an existent MR-damper

In order to validate the described method, an existent damper whose properties are well known is taken. The damper belongs to Rene Zemp and it was implemented in the *Parque Araucano* building in Santiago, Chile (Zemp, 2008). Experimental results for this damper are available and were used to validate the total force prediction method explained herein.

The geometry of the MR-damper has been presented in chapter 2 in Figure 13. The fluid passes from one chamber to the contiguous through a thin gap between the piston and the steel cylinder. While the fluid moves along the gap pushed by the displacement of the piston, the flow crosses a magnetic flux, which is generated by two coils wound around the piston. The magnetic field is controlled externally through a current intensity according to a target control algorithm.

An overview of the three-dimensional *Magnetostatic* model mesh of the MR-damper was already shown in Figure 14 (a), with a longitudinal section to the geometry. Finite elements have been also modeled with the *solid117* Ansys element. Boundary conditions are given by zero voltage applied at the external surfaces of the air chamber, and by the electric current intensity that runs inside each coil in opposite directions, which is presented in Figure A.I 25. Each coil has 447 turns of AWG 19 copper wire. The arrows represent the direction of the current flow on each coil. Electric current varies from zero to $2[A]$, in intervals of $0.5[A]$.

The magnetic flux expected is shown schematically in Figure A.I 26. The flux travels around each coil crossing through the gap at both sides, and it is increased by the flux of the adjacent coil. It does not leak through the head plates due to a bronze guide installed in the interface between the head plates and the piston rod.

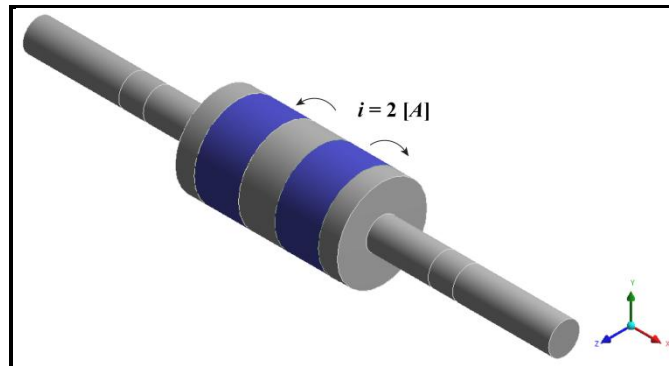


Figure A.I 25. Electric current on each coil of the validation model

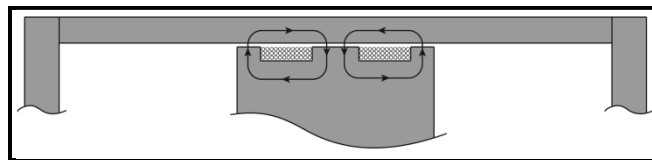


Figure A.I 26. Desired magnetic flux of the validation model

It is apparent that the radial flux at the central path between the coils interacts with the flux resulting from the adjacent coil. Shown in Figure A.I 27 is the resulting magnetic field strength H [kA/m], for an electric current intensity of 2 [A] running inside the coils. The zone located between coils concentrates the larger H values, but it does not reach saturation, which is above 250 [kA/m]. Saturation can be obtained by applying larger electric currents as an input. Symmetry of the results is explained by the symmetry of the configuration. The results in the fluid gap are, again, taken and used as an input for the fluid dynamics model of the damper.

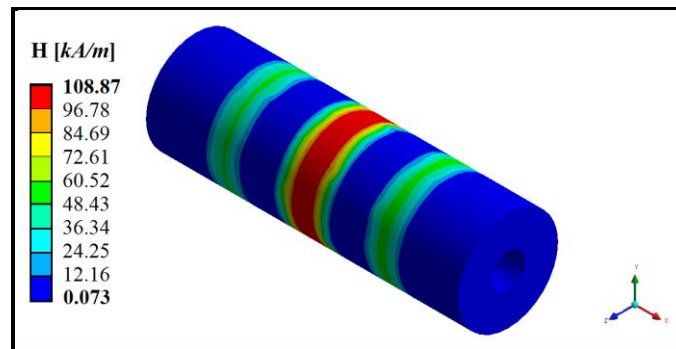


Figure A.I 27. Magnetic field strength in the fluid gap, validation model

The domain modeled in *CFX* is that of fluid inside the MR-damper. The mesh of the fluid domain considered in this model was already shown in Figure 14 (b). It corresponds to one fluid domain, which includes both chambers at the sides of the piston and the gap between the piston and cylinder. The model was meshed using the meshing application of *CFX*, and consists of hexahedral elements. The gap is meshed separated from the rest of the domain, as it needs several layers of regular elements in order to obtain an accurate velocity profile of the fluid.

The initial and final ends of the domain are defined in Figure A.I 28. Two types of boundary conditions related with the fluid domain are specified. The first group includes for the fluid: (i) no-slipping at the cylinder and piston surfaces, (ii) the inlet, and (iii) an opening at the end. The other group includes: (iv) a velocity profile at the inlet of the fluid domain, and (v) the yield stress that results from the *Magnetostatic* model and that is used in the values of the dynamic viscosity.

An imposed flow at the ends of the model has been used again as defined in Eq. (1) given its simplicity and the negligible differences obtained relative to the model with a moving mesh. A reference pressure of 0 [Pa] is defined in the opening. The rest of the surfaces have a no-slip wall boundary condition.

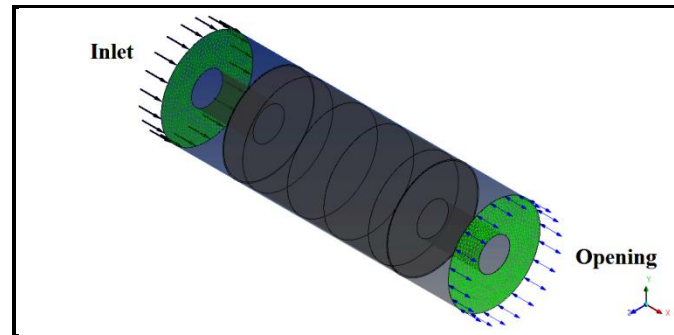


Figure A.I 28. Imposed flow boundary conditions at the initial and final ends of the domain, validation model

Laminar flow is considered in the fluid model. A transient analysis is performed with a maximum velocity given by $v_0 = 0.12$ [m/s], a frequency $\omega = 2.4$ [rad/s] and time-step $dt = 1 \cdot 10^{-3}$ [s]. Results are then filtered in order to reduce noise due to the coarseness of the time interval, as it was already presented.

Damper force is computed by integrating the total x-force on the piston at the anterior and posterior heads. Thus, the constitutive force-velocity ($F-V$) and force-displacement ($F-D$) relationships can be obtained, which are shown in Figure A.I 29 and Figure A.I 30, respectively. It should be noticed again that the Bingham model does not include the possibility of force-velocity hysteresis, and hence, such behavior cannot be considered using this model. The maximum damper force obtained for the given parameter values was about 13.86 [ton]. The noise on the figures is produced by the time step selected, which is coarser than the one required to assure perfect convergence of the *CFX* simulation. This data was processed and a smoothing moving average (MA) scheme was applied using 12 points of the data. Even with this MA scheme, the noise could not be eliminated completely, though its maximum force value produces a negligible error with respect to the output given at the required time-step.

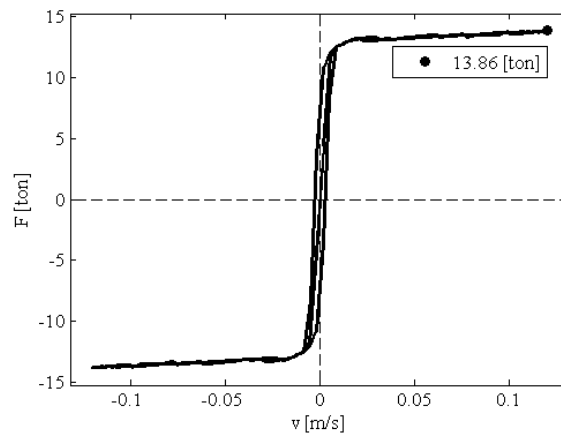


Figure A.I 29. Force-Velocity curve obtained in *CFX*, validation model

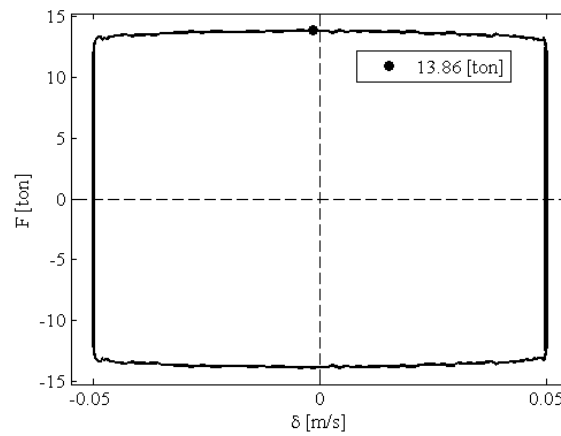


Figure A.I 30. Force-Displacement curve obtained in *CFX*, validation model

The damper was locally manufactured in 2007 and tested at the dynamic testing laboratory of *Pontificia Universidad Católica de Chile*. A picture of the built damper was shown in Figure 15. The first set of experimental tests consisted in harmonic motions applied vertically to the piston at different constant current intensities, corresponding to $I = 0, 0.5, 1, 1.5, 2$ and 2.5 [A]. Testing included also different displacement amplitudes and periods. Shown in Figure A.I 31 are the results for a displacement of 5 [cm] and a period of 2.7 [s]. The MR-damper can achieve a capacity of up to 14.78 [ton] at 2.5 [A], while the force measured at 2 [A] was 13.82 [ton].

The 2 [A] results were selected for comparison with the analytical model. Predicted and experimental $F-V$ and $F-D$ constitutive relationships are plotted together in Figure A.I 32 and Figure A.I 33, respectively. It is apparent that the maximum force of the damper, as well as its post yield slope, are well captured by the analytical model. As said before, since a Bingham model has been used to represent the constitutive behavior of the damper, the hysteresis observed in the loop cannot be predicted. The model predicts a maximum force 0.32% greater than the obtained by experimental testing.

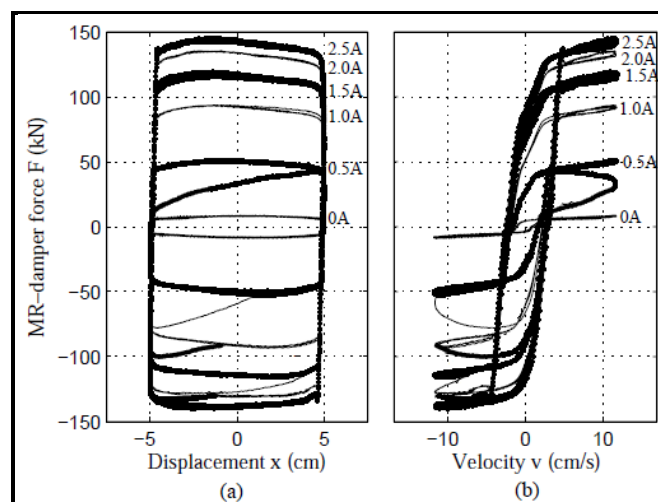


Figure A.I 31. Experimental results for MR-damper harmonic testing: (a) $F-D$ constitutive; and (b) $F-V$ constitutive relationships

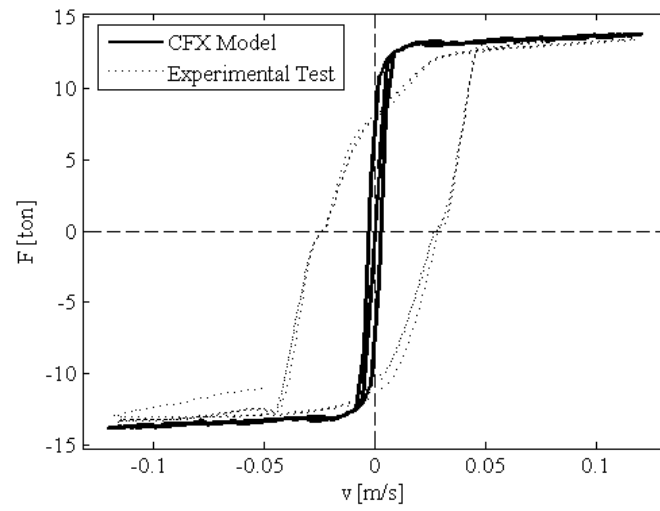


Figure A.I 32. Comparison between the measured and predicted force–velocity relationship of the 15 [ton] MR-damper

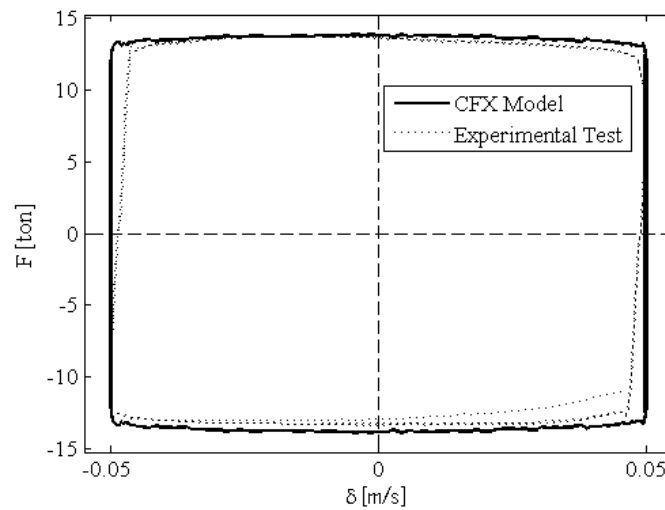


Figure A.I 33. Comparison between the measured and predicted force–displacement relationship of the 15-ton MR-damper

I.7 Estimation of Pressure Raise because of Heat Generation

The constitutive relationship *force-deformation* obtained from *CFX* model for our damper considering a maximum velocity of 25 [cm/s] is taken, and can be seen on Figure A.I 34. This simulation differs with the one presented in chapter 2 as it can be seen in the total force value, since this analysis was done before the final design. The area enclosed by the curve corresponds to the energy dissipated by the damper in one cycle, and it has a value of 25.544798 [ton·m], which corresponds to 250594.47 [J].

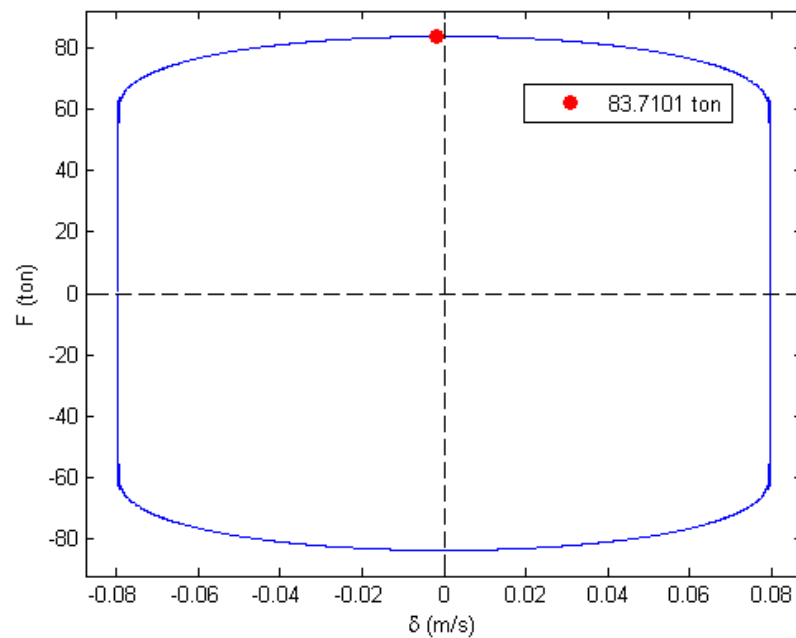


Figure A.I 34. *F-D* curve obtained for the model taken into account for heating estimation.

First, a summary of the equations used in this study is presented. By using Eq. (7) it is assumed that all the energy is dissipated by heating. The temperature raise produced by the energy dissipation is used in Eq. (8) to obtain the volumetric change, which allows us to predict the pressure raise in a cycle with Eq. (9).

$$\Delta Q = m \cdot C_p \cdot \Delta T \quad (5)$$

$$\Delta V = \alpha V \Delta T \quad (6)$$

$$\Delta V = \beta V \Delta P \quad (7)$$

Where ΔQ represents the dissipated energy; m is the mass of the material; C_p corresponds to the specific heat capacity; ΔT represents the change in temperature; α is the thermal expansion coefficient; V corresponds to the volume of the elements of each considered material; β corresponds to the compressibility of the material; and ΔP represents the pressure raise due to heating.

Material properties are summarized in Table A.I 2. Thermal expansion and compressibility of steel and bronze have been neglected on the heating process, i.e. only expansion of the fluid is considered. The mass is obtained by multiplying the volume of each material with its density ρ . In a first analysis, only the fluid is taken into account in the heating process. Its volume belongs to both chambers, the 24 holes and the fluid gap.

Table A.I 2 Summary of physical and geometrical properties for heat transfer.

Materials	Material Properties				Geometric Properties	
	α [1/K]	β [1/bar]	C_p [J/kg·K]	ρ [kg/m ³]	V [m ³]	M [kg]
MRF132 DG Fluid	0.0005	$5.8 \cdot 10^{-5}$	683	3000	0.025818	77.45
Steel	-	-	500	7850	0.045377	356.21
Diamagnetic Material	-	-	435	8900	0.006279	55.88

In a second analysis, not only the fluid, but also the internal steel cylinder and the bi-metallic external cylinder are taken into account, looking for more accuracy and reliability. This addition implies the modification of the Eq. (3), which is shown in Eq. (6). Results for both analyses can be seen in Table A.I 3. The piston and two cylinders are considered, the internal steel cylinder (including 24 $\Phi 20$ [mm] holes), and the external bi-metallic cylinder.

$$\Delta Q = (m_f \cdot C_f + m_s \cdot C_s + m_b \cdot C_b) \cdot \Delta T \quad (8)$$

Table A.I 3. Results of pressure raise estimation

Materials considered	ΔT [K]	ΔV_f [m ³]	ΔP [bar]
Fluid	4.73	$6.106 \cdot 10^{-5}$	40.78
Fluid, steel and bronze	0.98	$1.265 \cdot 10^{-5}$	8.45

The pressure obtained from the second analysis is 4.82 times smaller than the calculated in the first one. Then, steel and bronze cannot be neglected when obtaining pressure raise due to heat transfer, since it can lead to overrated results. Assuming that a test will have 10 cycles as a maximum, pressure can reach 84.5 [bar]. The damper has a 90 [ton] capacity, which implies that the pressure difference between chambers is 180 [bar] approximately. This means that there has to be at least an initial pressure of 180 [bar] so it doesn't decrease below the zero level. Maximum pressure is then given by $P_{max} = 180 + 180 + 84.5 = 444.5$ [bar]. And if an additional pressure of 30 [bar] is added for security issues, then the maximum pressure can easily reach 475 [bar]. A design pressure of 500 [bar] is then established.

APPENDIX II: MR-DAMPER DESIGN

Every aspect of the design stage is explained herein. In first place, the materials used in this project are described. Then, a pre-design stage is presented, in which the general dimensions of the damper have been decided. Since this is a preliminary design stage, Yang's formula will be introduced and used instead of a *CFX* model to obtain a prediction of the controllable force. The selection of wiring is also justified in this appendix. In order to assure that the damper will work properly, a pressure test was performed to a cylinder similar to the final design which is also discussed in this appendix. Finally, other design configurations were compared with the finally manufactured damper, such as a typical configuration with the coils around the moving piston, and configurations with three and five coils.

II.1 Materials Specification

Materials used through this research are SAE 1045 steel and Lord MRF-132DG fluid. Their properties are listed below.

Relevant physical and mechanical properties of SAE 1045 steel are (i) density, (ii) Young modulus, (iii) yield strength, and (iv) ultimate strength, which are given by $\rho = 7850 \text{ [kg/m}^3\text{]}$, $E = 2100 \text{ [ton/cm}^2\text{]}$, $f_y = 400 \text{ [MPa]}$ and $f_u = 620\sim 720 \text{ [Mpa]}$ respectively. Magnetic properties for SAE 1045 steel are given by a Magnetization (B-H) curve, since it is a material with nonlinear magnetic behavior: Its *B-H* curve can be seen in Figure A.II 1 (Lorenz, Fowler, 2006). It saturates at a magnetic flux of 1.6 [T] and a magnetic field strength given by 5 [kA/m].

Magneto-rheological fluid corresponds to Lord MRF 132DG fluid. Its typical properties are given by the provider and listed in Table A.II 1 (LORD Co, 2008). Since it is basically a nonlinear material in terms of its magnetic properties, a *B-H* curve is given in Figure A.II 2. In comparison with SAE 1045 steel, Lord fluid develops magnetic field strengths ten times higher, but it does not have a clear saturation point.

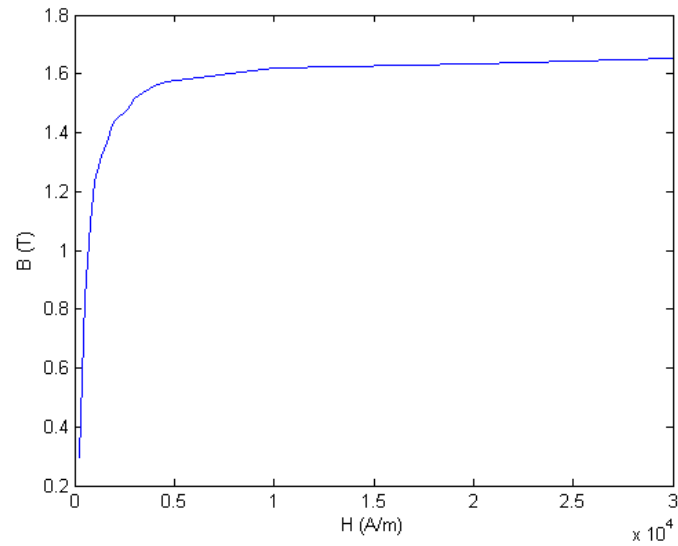


Figure A.II 1. B-H curve for SAE 1045 steel

Table A.II 1. Typical properties of Lord MRF-132DG

Viscosity	$0.092 \pm 0.015 [Pa \cdot s] @ 40 \text{ } ^\circ C$
Density	$3000 [kg/m^3]$
Solids Content by Weight	80.98%
Flash Point	$>150 [^\circ C]$
Operating Temperature	$-40 \text{ to } +130 [^\circ C]$
B-H Curve	Figure A.II 2
$\tau_0(H)$	Figure A.II 3

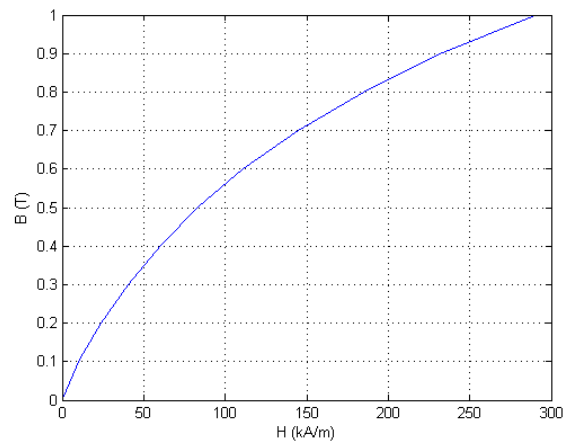


Figure A.II 2. B-H curve, Lord MRF 132DG fluid

Finally, because of its plastic behavior under the influence of a magnetic field, the manufacturer also provides the yield stress of the fluid related to the magnetic field strength, shown in Figure A.II 3. It saturates to $48.32 [kPa]$ at $300 [kA/m]$.

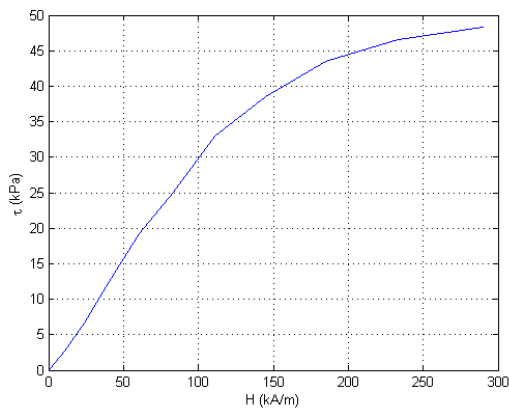


Figure A.II 3 Yield stress vs magnetic field strength, Lord MRF 132DG

II.2 Pre-Design Stage

In the pre-design stage, *Magnetostatic* application of Ansys software was used to obtain the magnetic field strength. Matlab codes were designed to process the outputs of the magnetic analyses, and the estimation of the maximum controllable force was done with the formula derived in the dissertation of Yang (Yang, 2001), which will be further explained.

Several models were run in order to decide the best option to get a controllable force of 60 [ton]. The geometric parameters to be varied were: (i) Number of coils, N_c ; (ii) electric current, i ; (iii) number of turns per coil, N ; (iv) distance between coils, b ; (v) coils width, L_c ; (vi) piston radius, r_p ; (vii) gap size, h ; (viii) cylinder length, L_{cyl} ; and (ix) the internal cylinder holes diameter, d_h .

The geometry used for this pre-design stage is presented in Figure A.II 4. The head plates have been modeled as if they were made of bronze, so the magnetic flux cannot pass through them. Final design does not have this configuration, but there are other ways to avoid flux from passing, which will be further analyzed. Dimensional parameters can also be understood from Figure A.II 4. The maximum velocity taken into account for modeling was 25 [cm/s].

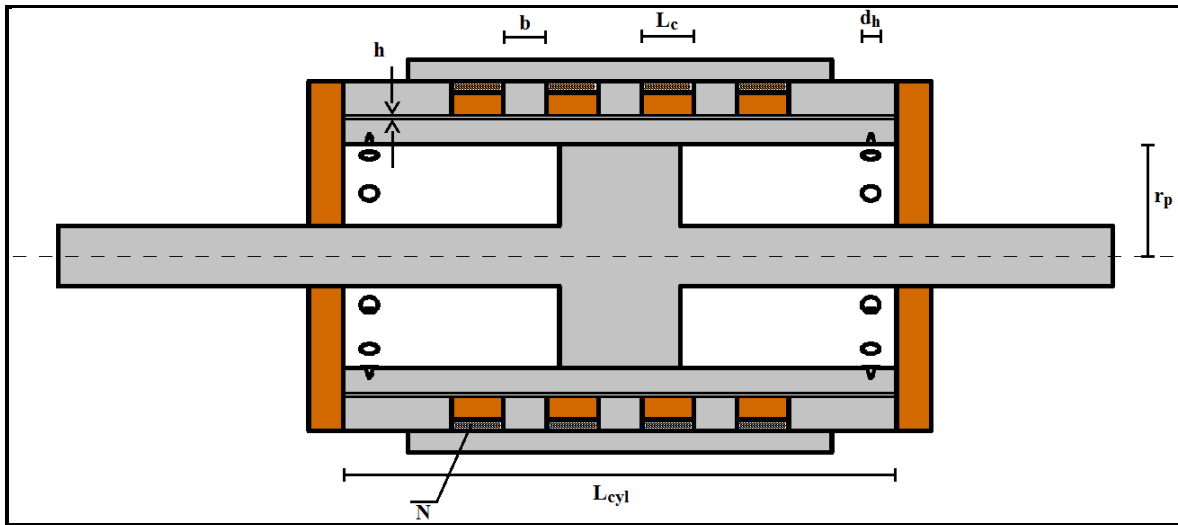


Figure A.II 4. Configuration used for the pre-design stage.

The pre-design process will be exemplified with one of the models taken into account for the design, which will not necessarily be the finally chosen model.

- Geometric parameters

The model chosen for exemplifying the design process is model n° 20. Its geometric parameters are shown in Table A.II 2. It needs to be noticed that this is not the finally chosen model for design:

Table A.II 2. Parameters of the model used to exemplify the pre-design process

N_c	i [A]	N	b [mm]	L_c [mm]	r_p [mm]	h [mm]	L_{cyl} [mm]	d_h [mm]
4	3	450	80	70	75	1	730	20

- Magnetic Model

Models are done as explained in chapter 2. In this case the mesh, which can be seen in Figure A.II 5, consists of 999,210 elements and 1,450,390 nodes. Magnetic field strength over the fluid domain is shown in Figure A.II 6. It is exported to an excel table to be processed using Matlab. The output can be exported in excel format, and it has the structure shown in Table A.II 3.

Table A.II 3. Extract from the *Magnetostatic* model output

ANSYS Node N°	X [m]	Y [m]	Z [m]	Total Magnetic Field Intensity [A/m]
70156	-0.35947	0.060079	-0.079315	33983
109380	-0.35917	0.059645	-0.080887	33983
⋮	⋮	⋮	⋮	⋮

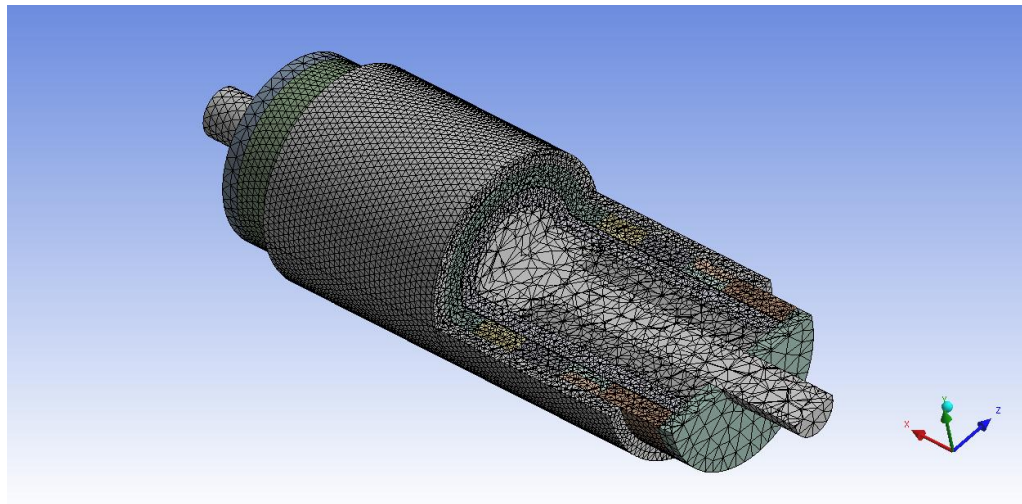


Figure A.II 5. View of the mesh of model n° 20

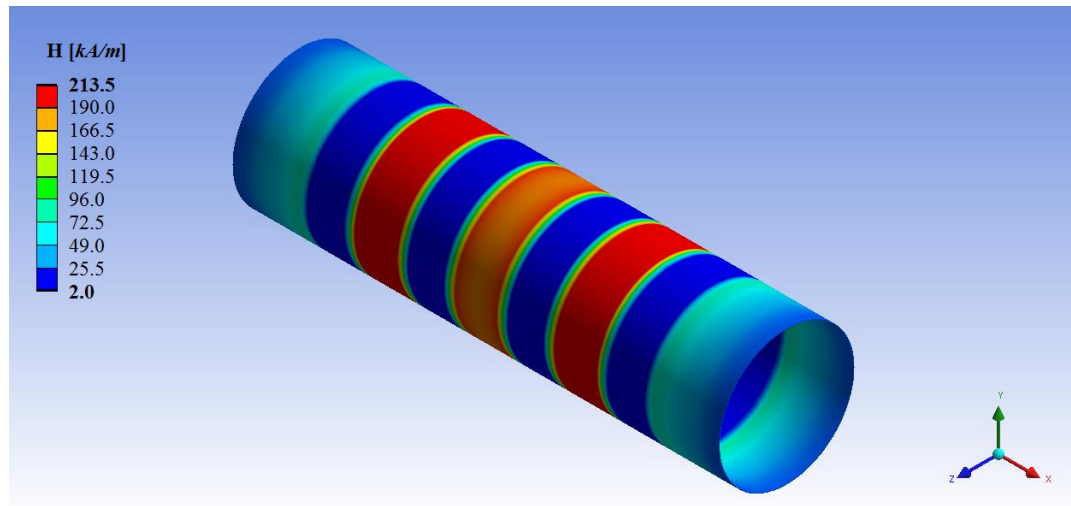


Figure A.II 6. Magnetic field intensity over the fluid domain of model n° 20

- Matlab output processing

First, the location of each active portion of fluid must be determined. An active portion of fluid is given by fluid that is significantly affected by the magnetic field, and therefore increases the controllable force of the damper. From Figure A.II 4, these zones correspond to those that are located between the coils, since no magnetic flux can cross the fluid regions right under them, because of the diamagnetic characteristics of some cylinder components. In other words, they correspond to the regions which are not colored in blue. Since the relevant axis for delimiting the zones is the axial axis, y and z coordinates are not taken into account. The active fluid regions axial (x) coordinates are detailed in Table A.II 4. An average yield stress is estimated in each fluid active portion, using a Matlab routine. The fluid zones that are located beyond the holes of the internal cylinder are not taken into account. The algorithm is summarized below.

Table A.II 4. Active regions in the fluid gap domain

Active Region	AR 1	AR 2	AR 3	AR 4	AR 5
Coordinates	$-322 < x < -260$	$-190 < x < -110$	$-40 < x < 40$	$110 < x < 190$	$260 < x < 322$
Length	62 [mm]	80 [mm]	80 [mm]	80 [mm]	62 [mm]

- First, from Lord Technical Data, the relationship $\tau - H$ is used to obtain the yield stress in each point of the domain where the magnetic field strength has been calculated, with a limit value of $\tau_{max} = 48.32$ [kPa].
- Then, only the location of the nodes corresponding to an active region of fluid and their yield stress are extracted. In other words, the output is filtered, eliminating any unneeded data.
- The next step is to obtain an average yield stress for each active portion of fluid, by simply adding the yield stresses obtained in the last step, and dividing them by the total number of nodes in that portion: The obtained values can be seen in Table A.II 5:

Table A.II 5. Average yield stresses in each active portion of fluid gap domain [kPa]

$\bar{\tau}_{left}$	$\bar{\tau}_{center-left}$	$\bar{\tau}_{center}$	$\bar{\tau}_{center-right}$	$\bar{\tau}_{right}$
19.58	45.28	45.77	45.28	19.69

- Now, an average global yield stress is estimated using a weighted average, considering all of the yield stress averages for each active portion of fluid and their respective length. The goal of this calculation is

to obtain a representative yield stress for the total active pole length to be used in Yang's expression for controllable force.

$$\bar{\tau} = \frac{1}{364 [mm]} (62 \cdot \bar{\tau}_{left} + 80 \cdot \bar{\tau}_{center-left} + 80 \cdot \bar{\tau}_{center} \dots + 80 \cdot \bar{\tau}_{center-right} + 62 \cdot \bar{\tau}_{right})$$

$$\Rightarrow \bar{\tau} = 36.67 [kPa]$$

- Finally, to estimate the controllable force in a pre-design stage, Yang's formula, which is defined in Eq. (7), can be used. It is based upon the parallel plate model (Yang, 2001).

$$F_{\tau} = \left(2.07 + \frac{12A_p v_0 \eta}{12A_p v_0 \eta + 0.4wh^2 \tau_0} \right) \frac{\tau_0 L A_p}{h} \quad (9)$$

Where, A_p corresponds to the area of the piston; L is the total active pole length; v_0 represents the maximum velocity of the excitation; h corresponds to the gap size; w is the average perimeter through which the fluid flows; η is the dynamic viscosity of the fluid in absence of a magnetic field; and τ_0 represents the fluid yield stress. Their values can be seen in Table A.II 6.

Table A.II 6. Parameter values for model n° 20

$A_p [m^2]$	$L [m]$	$v_0 [m/s]$	$h [m]$	$w [m]$	$\eta [Pa \cdot s]$	$\tau_0 [kPa]$	$F_{\tau} [ton]$
0.0156	0.364	0.25	0.001	0.6315	0.092	36.67	50.81

A total of 50 models were taken into account on this pre-design stage. Throughout the process, it became necessary to raise the number of coils to four, in order to achieve the desired force in a more efficient way, since it maximizes the damper's capacity and minimizes the response time of the system. An odd number of coils was analyzed separately and will be further detailed. The number of turns finally chosen is 250 per coil. As models were run, it became clear that, to achieve approximately 1[T] on the fluid, at least 1.3[T] needed to be obtained in the internal cylinder. Once its width had been established, the number of coils could be calculated using the expression for magnetic voltage, or ampere-turns which is shown in Eq. (8) (Zemp, 2008).

$$Ni = \sum H_{ck}L_{ck} \quad (10)$$

where H_{ck} is the intensity on the k -th part of the magnetic circuit and L_{ck} corresponds to its length. On the other hand, the magnetic flux is constant throughout the magnetic circuit, and is given by:

$$\Phi = B_{ck}A_{ck} \quad (11)$$

where B_{ck} is the magnetic flux density on the k -th region of the magnetic circuit and A_{ck} its cross area, which will be taken as the width, multiplied by 1 [mm]. Regions are described on Figure A.II 7, where they are shown around the left coil. If a magnetic flux density of 1.3[T] is needed at the internal cylinder (zone 2 of Figure A.II 7), then a total magnetic flux of $\Phi = 39 [T \cdot mm^2]$ must be developed. Since this is a constant value, needed magnetic flux density values in the other zones can be obtained, and then the B - H curve of steel can be used to read the values of H . The details for each zone are presented in Table A.II 7.

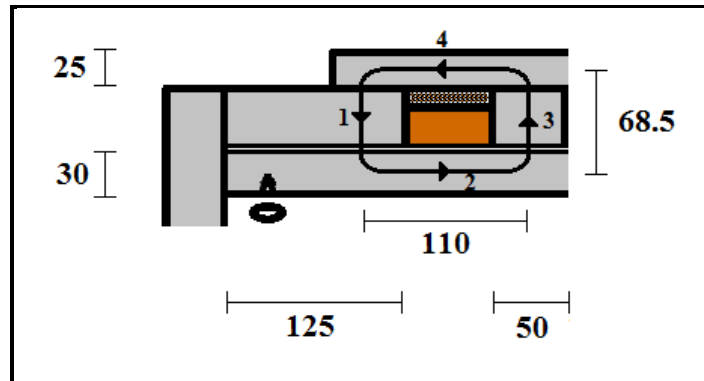


Figure A.II 7. Schematic view of the left coil. Dimensions are expressed in [mm]

Table A.II 7. Obtained values of magnetic field strength for each zone.

Zone	A_{ck}	$B_{ck} = \Phi/A_{ck}$	H_{ck}
1	125 [mm ²]	0.312 [T]	0.3 [A/mm]
2	30 [mm ²]	1.3 [T]	1.2 [A/mm]
3	50 [mm ²]	0.78 [T]	0.5 [A/mm]
4	25 [mm ²]	1.56 [T]	4.0 [A/mm]

Finally, with the current intensity set up at 3 [A], all values can be replaced in Eq. (8) to find the number of turns, which is calculated as $N = 208.93$ [turns].

When deciding the piston radius, the desired force is crucial. Since the force is equal to the product of the pressure difference between chambers and the piston area, an increase on the piston radius implies an increase in the desired force. Maximum pressures must be considered as well, in order to obtain reasonable operation values. A pressure study is further included in this research.

Two important quantities must be taken into account when designing the gap size: the dynamic range and the desired force. Dynamic range is defined as the ratio between

the damper controllable force and the uncontrollable force. This topic will be treated in Appendix III.

In Table A.II 8 the first 15 models of this preliminary stage are shown. Looking at them, it is clear that the diameter of the holes of the internal cylinder does not have an influence on the controllable force F_τ , but it does affect the viscous force F_η . Intuitively, as the holes diameter increases, the viscous force decreases. This fact can be proven by using the expression obtained by Yang for the viscous force, which is:

$$F_\eta = \left(1 + \frac{wh}{2A_p}\right) \frac{12\eta A_p^2 L v_0}{wh^3} \quad (12)$$

Applying Eq. (10) to each model, the viscous force can be obtained. Only the first 15 models are taken. It must be noticed, that they can be divided into three groups of five models that share the same geometric properties, except for the holes diameter. Then, the output of the viscous force gives us an idea of how it affects the global behavior of the damper. In Table A.II 9 this quantity is presented for each one of the 15 models and it can be seen that the intuition was correct, since the viscous force does decrease when the diameter of the holes increases. It is also clear that the rate of change of F_η decreases when d_h increases. This fact can give us an approach of what size of diameter is needed in order to reduce viscous effects, which is crucial for obtaining a high dynamic range value.

A diameter of 20 [mm] is then chosen, considering the following facts: (i) A high dynamic range is assured; (ii) as long as the diameter increases, the stroke of the damper is reduced, and the aim of this research was to achieve a stroke of ± 200 [mm]; (iii) a variation of the diameter above 20 [mm] does not imply a considerable increase in the dynamic range. Twelve holes in each side of the internal cylinder were chosen, taking into account that this parameter has also an influence on the viscous force. Finally, the geometric parameters for the design stage are the ones shown in Table A.II 10.

Table A.II 8. Details of the first 15 analyzed models in the pre-design stage

Model	N_c	i [A]	N	b [mm]	L_c [mm]	r_p [mm]	h [mm]	L_{cyl} [mm]	d_h [mm]
1	2	3	450	40	70	75	2	466	5
2	2	3	450	40	70	75	2	466	10
3	2	3	450	40	70	75	2	466	15
4	2	3	450	40	70	75	2	466	20
5	2	3	450	40	70	75	2	466	25
6	2	3	450	40	70	75	1.5	466	5
7	2	3	450	40	70	75	1.5	466	10
8	2	3	450	40	70	75	1.5	466	15
9	2	3	450	40	70	75	1.5	466	20
10	2	3	450	40	70	75	1.5	466	25
11	2	3	450	60	70	75	1.5	466	5
12	2	3	450	60	70	75	1.5	466	10
13	2	3	450	60	70	75	1.5	466	15
14	2	3	450	60	70	75	1.5	466	20
15	2	3	450	60	70	75	1.5	466	25

Table A.II 9. Influence of the diameter of the holes over the viscous force

Model	d_h [mm]	F_η [ton]
1	5	5.3751
2	10	1.0913
3	15	0.2461
4	20	0.1723
5	25	0.1449
6	5	5.7867
7	10	1.343
8	15	0.8245
9	20	0.3517
10	25	0.3102
11	5	5.7867
12	10	1.343
13	15	0.8245
14	20	0.3517
15	25	0.3102

Table A.II 10. Geometric parameters for pre-design

N_c	i [A]	N	b [mm]	L_c [mm]	r_p [mm]	h [mm]	L_{cyl} [mm]	N_h	d_h [mm]
4	3	250	50	60	130	1.5	640	12	20

II.3 Wire Selection

In order to choose the appropriate wire for our damper, let the following parameters be: (i) Number of turns per coil, $N = 250$; (ii) internal radius of the coils, $r_{ci} = 0.1855$ [m]; (iii) external radius of the coils, $r_{ce} = 0.2025$ [m]; and (iv) the current flowing in each coil, $i = 3$ [A].

The first criterion for choosing the wire gauge is the current capacity. The wire needs to withstand at least 3 [A]. On Table A.II 11 the current rating for different AWG gauges is shown. The data has been extracted from the “Handbook of Electronic Tables and Formulas for American Wire Gauge”. *Maximum Amperes for Power Transmission* column uses the 700 circular mils per amp rule, which is very conservative. *Maximum Amperes for Chassis Wiring* column is meant for wiring in air, and not in a bundle.

Table A.II 11. Summary of current ratings for each AWG Gauge

AWG Gauge	Diameter [mm]	Max amps for chassis wiring	Max amps for power transmission
6	4.1148	101	37
7	3.66522	89	30
8	3.2639	73	24
9	2.90576	64	19
10	2.58826	55	15
11	2.30378	47	12
12	2.05232	41	9.3

13	1.8288	35	7.4
14	1.62814	32	5.9
15	1.45034	28	4.7
16	1.29032	22	3.7
17	1.15062	19	2.9
18	1.02362	16	2.3
19	0.91186	14	1.8
20	0.8128	11	1.5
21	0.7239	9	1.2
22	0.64516	7	0.92

An *AWG 16* wire is preliminary chosen. Now, the medium radius of each coil is given by $\bar{r}_c = 0.194$ [m], therefore, the total length of each coil is: $L_c = 304.73$ [m]. On the other hand, for an *AWG 16* wire, the resistance is given by $R = 13.18$ [Ω/km], then, by following Ohm's law, $V = 39.54$ [V/km]. Finally, for each coil, $L_c = 0.30473$ [km], giving a voltage loss of $V_c = 12.0492$ [V]. Power supply used in this research has a maximum voltage capacity of 30 [V]. Finally, *AWG 16* wire is chosen.

II.4 Test Cylinder

This section describes the hydraulic pressure tests that were made to a bi-metallic cylinder with similar dimensions to the one that has been designed. The objectives of these tests are: (i) To ensure that the welding process is appropriate to bear high pressures by not allowing fluid to filter between materials, which implies that the welding process does not generate pores and that the union of the materials is good enough to the service the cylinder was designed for; (ii) to verify that the strength of the chosen materials is appropriate; and (iii) to decide the minimum thickness that the diamagnetic elements of the cylinder can have, before entering to plastic behavior.

Tests configuration can be seen in Figure A.II 8. It consists on the cylinder to be tested, two head plates, eight bolts and nuts. After its assembling, it is filled with hydraulic oil, by using a funnel through a hole that is then sealed. Then, pressure was

added to the system by using a pump. Pressure values from 100 to 600 [bar] are applied and the radial deformation is measured with a dial indicator.

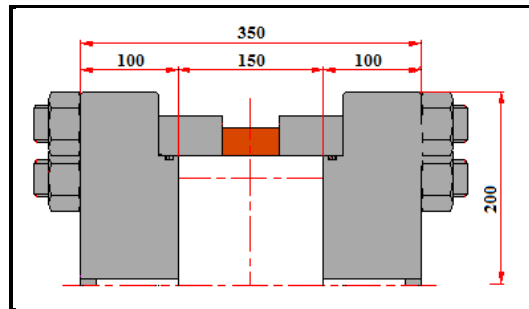


Figure A.II 8. Cylinder test configuration

Different bronze thicknesses were tested. First cylinder to be tested can be seen in Figure A.II 9 which consists of a thickness of 28 [mm] for the diamagnetic material. After the cylinder is tested, thickness is reduced to 24 [mm], by reducing the outside diameter, and the test is done again. A second thickness reduction is then applied, testing a cylinder with a thickness given by 21 [mm].

Characteristics of each test are summarized in Table A.II 12. Test N°1 was done inside a security system, with the cylinder not fixed to its surface, because of space issues. Then, results for this test must not be taken thoroughly. The configuration of the experiment was changed for tests N° 2 and 3, where the cylinder was anchored to a steel table. The detailed results are presented in Table A.II 13, where measures were taken every 50 [bar]. Only the test N°1 started at a pressure of 200 [bar]. The radial deformation of the micrometer was read and the remnant deformation, in the case of test N°3, was also measured.

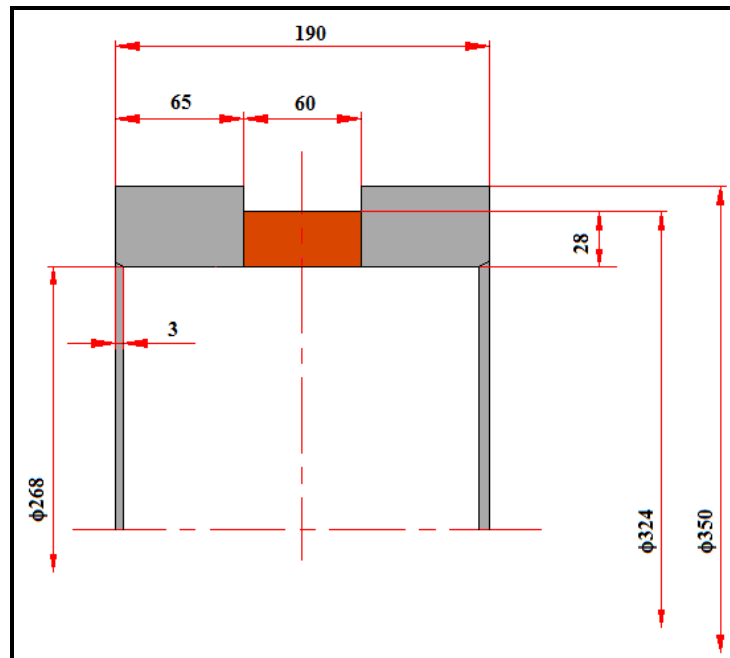


Figure A.II 9. Initial test cylinder

Table A.II 12. Tests characteristics

	Test N° 1	Test N° 2	Test N° 3
Thickness	28 [mm]	23 [mm]	21 [mm]
Outside Diameter	324 [mm]	316 [mm]	310 [mm]

Table A.II 13. Numerical results for each test.

Pressure [<i>bar</i>]	Measure [μm]			Discharge [μm]
	Test N°1	Test N°2	Test N°3	Test N°3
0	0	0	0	0
100	-	30	55	10
150	-	54	70	10
200	55	80	100	18
250	74	110	130	20
300	98	145	170	30
350	115	175	210	42
400	135	205	260	60
450	145	230	315	85
500	153	250	385	130
550	160	270	465	180
600	155	290	548	218

Figure A.II 10 presents a visual representation of the data shown in Table A.II 13. Test N°1 is taken only as a reference. In test N°2 there were no evidences of plastic deformation. The inside diameter was measured after the test, and it showed the same initial value, i.e. 316 [*mm*]. On the other hand, in test N°3 is clear that the cylinder has entered to the plastic range. Elastic discharges have a mean of 2.1205 [*bar*/ μm] with a variance of 0.0476. Final remnant deformation is 218 [*mm*]. Since maximum service pressure is expected to be 500 [*bar*], a security factor of 1.2 is assured in test N°2. The cylinder tested on test N°3 cannot be used in our design.

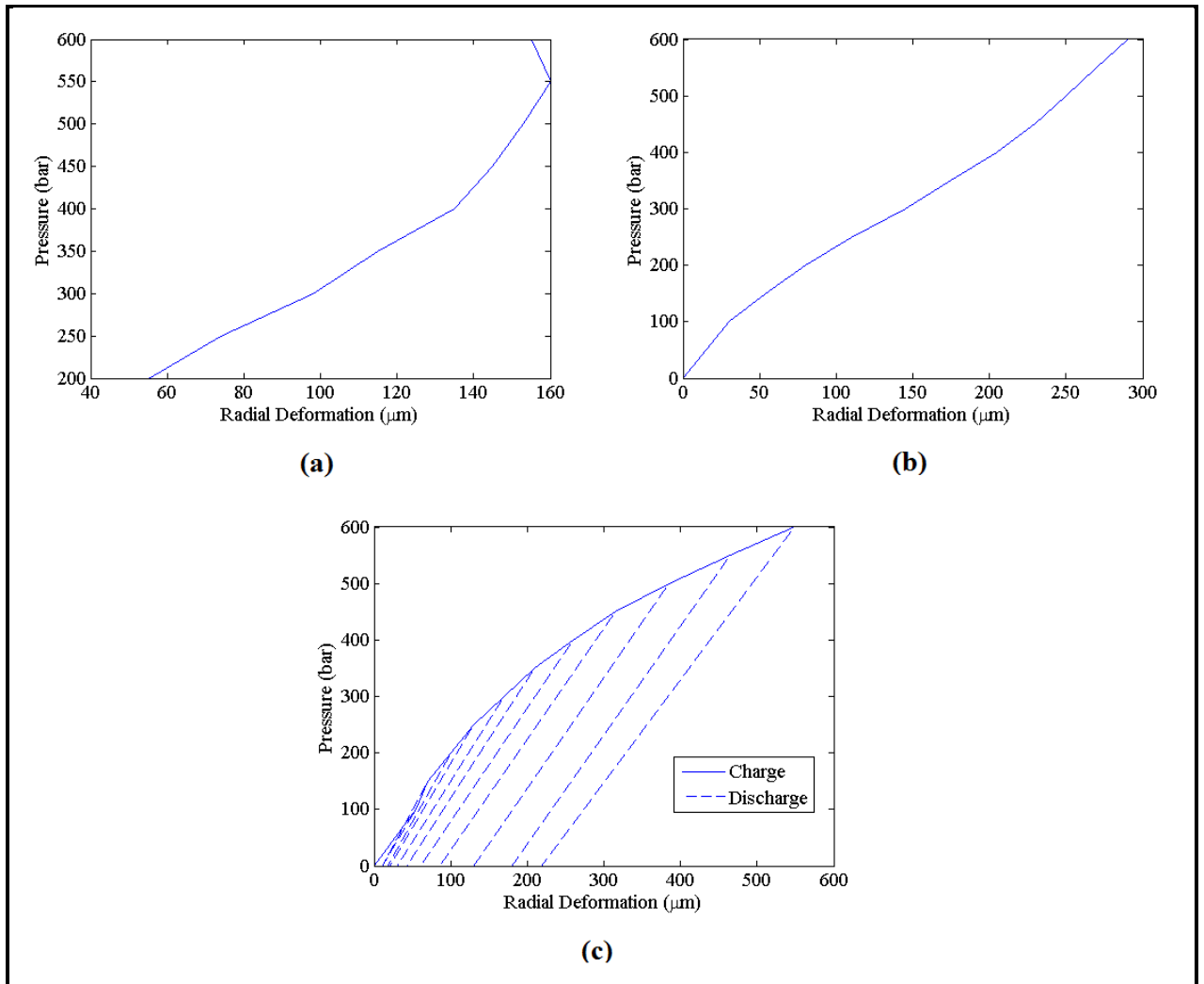


Figure A.II 10. Pressure vs Measured radial deformation. (a) Test N°1, (b) Test N°2, (c) Test N°3

II.5 External and Internal Winding Comparison

Most available magneto-rheological dampers have a typical bobbin distribution, which is winding the coil around the piston inside the damper. This configuration will be named as “internal winding” for our purposes. The damper designed in this research belongs to an atypical configuration, where the coils are wound around a cylinder external to the piston. This set up will be named as “external winding”. The main objective of this study is to show the advantages that the external winding configuration has over the internal winding. Therefore, two comparative analyses between the designed configuration and its alternative in an internal winding set up are done.

In the first comparative analysis, an internal winding configuration is taken, having similar size and total force than the finally manufactured design, with the aim to evaluate its stroke. The stroke of a damper is crucial to define the needs that it can satisfy when in service. A damper with a great stroke is more versatile than a damper with a small stroke, because it can take more displacement in a structure. When subjected to high scale seismic deformations, a damper with an insufficient stroke can require greater displacements than its designed limit, introducing undesirable loading to the global system.

The models contrasted in this analysis have the same active pole length of the fluid (i.e. same length of fluid affected by the magnetic field, which implies similar controllable forces) but their strokes are different.

In Figure A.II 11 we can see the external winding configuration, consisting of a piston (1), an internal steel cylinder (2), a bi-metallic external cylinder composed by bronze and steel rings (3), four coils wound up around the external cylinder bronze rings (4), an exterior steel layer (5), two steel head plates (6) and two bronze guides between the head plates and the piston rod (7). The rest of the space is filled with magneto-rheological fluid. Its detailed geometry is fully explained in Appendix I.

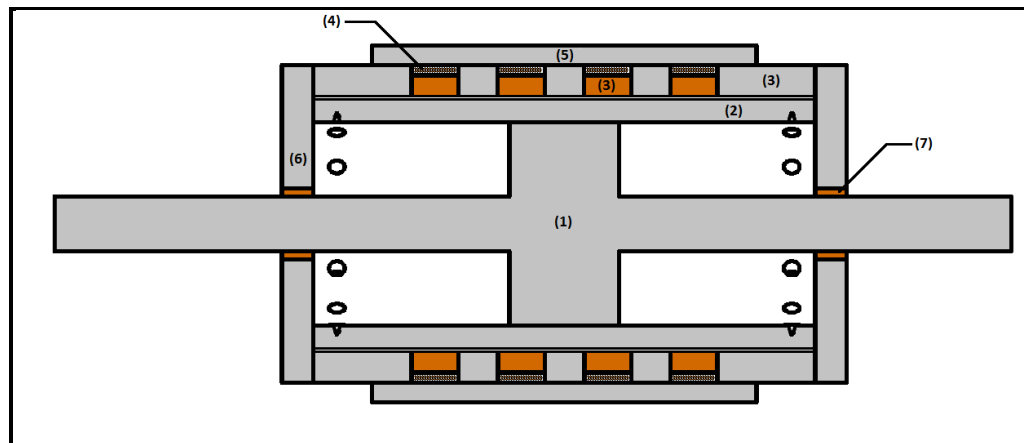


Figure A.II 11. External winding configuration geometry

By contrast, in Figure A.II 12 the most typical internal winding configuration can be visualized, and it consists of a piston (1), a cylinder (2), two steel head plates (3), four coils around the piston (4) and two bronze guides between the head plates and the piston rod (5). The empty space is filled with MR-fluid. There can be clearly noticed that the need of keeping the active pole length in the configuration of Figure A.II 12 forces a radical reduction of its stroke, which limits its usefulness on service.

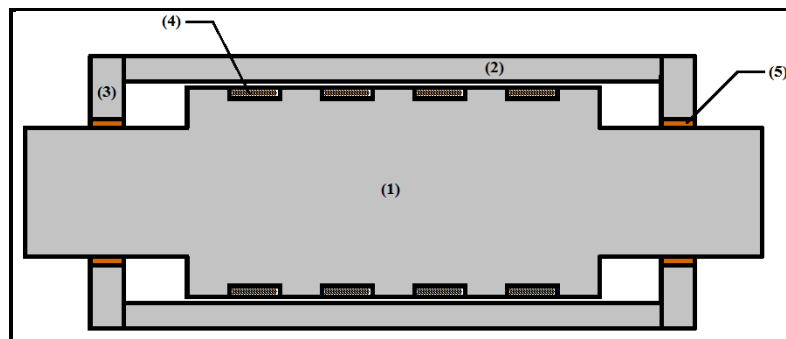


Figure A.II 12. Internal winding configuration geometry

To make both models comparable, they have the same piston area, as well as the same amount of coils, wire turns, fluid gap and radius. All cylinders have the same length, which implies that the active pole length cannot be equal in both cases, because otherwise the piston could not have any movement and its stroke would decrease to zero.

The mesh and the model are done with the same set up than the one explained in chapter 2 and in Appendix I. For the external configuration case, it consists of 923,054 nodes and 404,882 elements; while for the internal winding set up, it has 647,371 nodes and 426,841 elements.

Magnetic flux for the external configuration follows the paths shown in Figure A.II 13. The bronze guides avoid the magnetic flux from choosing a path through the head plates; therefore it runs around the coils, crossing through the fluid gap.

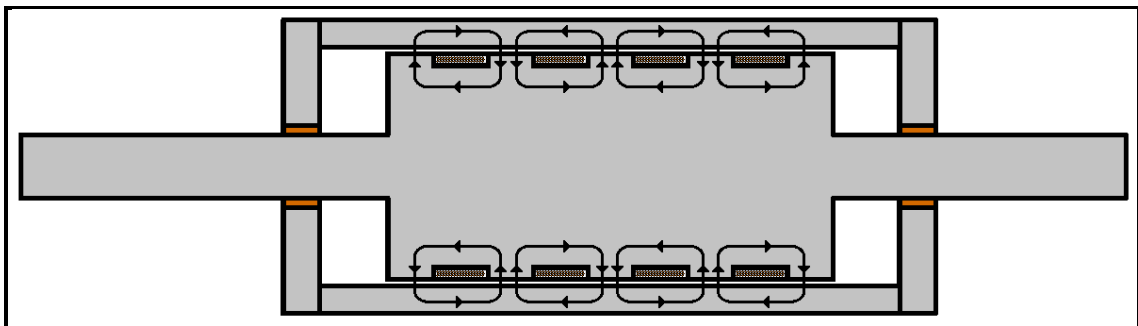


Figure A.II 13. Magnetic flux paths for external winding configuration

Results for external winding configuration can be seen in chapter 2 and in Appendix I. Magnetic flux density for internal winding configuration can be seen in Figure A.II 14, through an arrows diagram that shows also the direction of the flux. Its maximum values reach 1.3 [T] in the cylinder steel, and 1.28 [T] in the fluid gap domain. It can also be seen that the bronze guides avoid the magnetic flux from passing through the

head plates. Magnetic field strength for internal winding configuration obtained in the fluid domain can be seen in Figure A.II 15. Its maximum value is 499 [kA/m], which allows the fluid to reach yield stresses up to 48.32 [kPa].

Now, in order to compare both models, previously Eq. (7) will be used. As well as in other analyses, an average yield stress representing the active pole length of the fluid has also been obtained with the aid of Matlab software, taking into account gap regions which are not located directly above coils positions. In the case of internal winding configuration, active pole length is given by 0.25 [m] and the average yield stress $\bar{\tau}_0 = 37.86$ [kPa]. Therefore, controllable force for this model is $F_\tau = 74.53$ [ton]. Making a comparison with the results for the external winding model, the difference between both configurations can be seen on Table A.II 14. A force 13.4 % greater than the external winding model is obtained

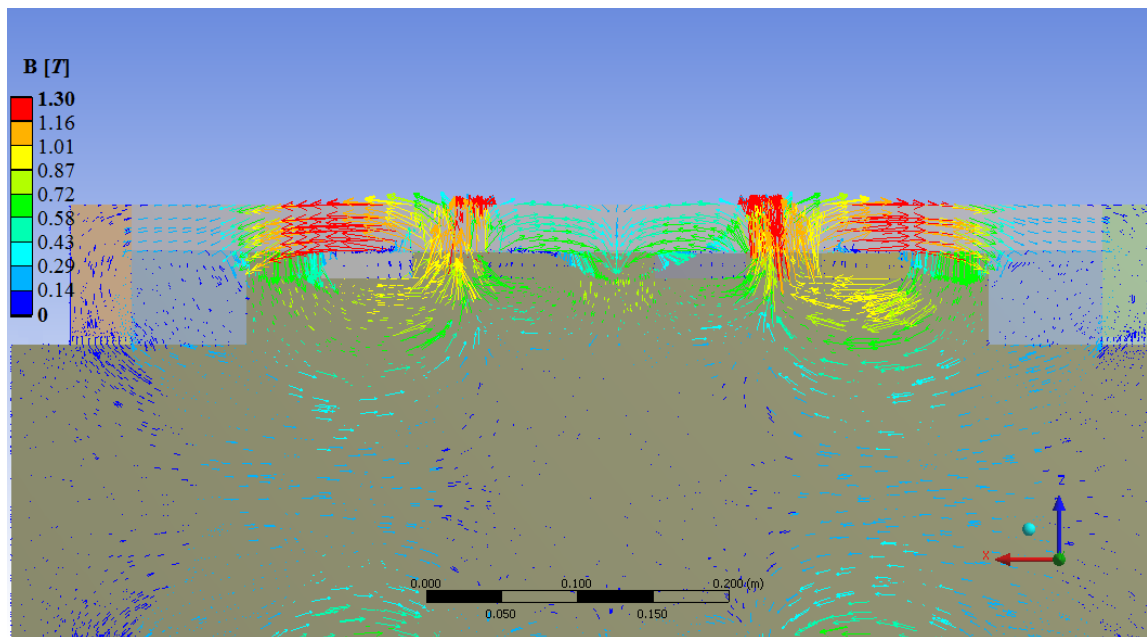


Figure A.II 14. Magnetic flux density, internal winding

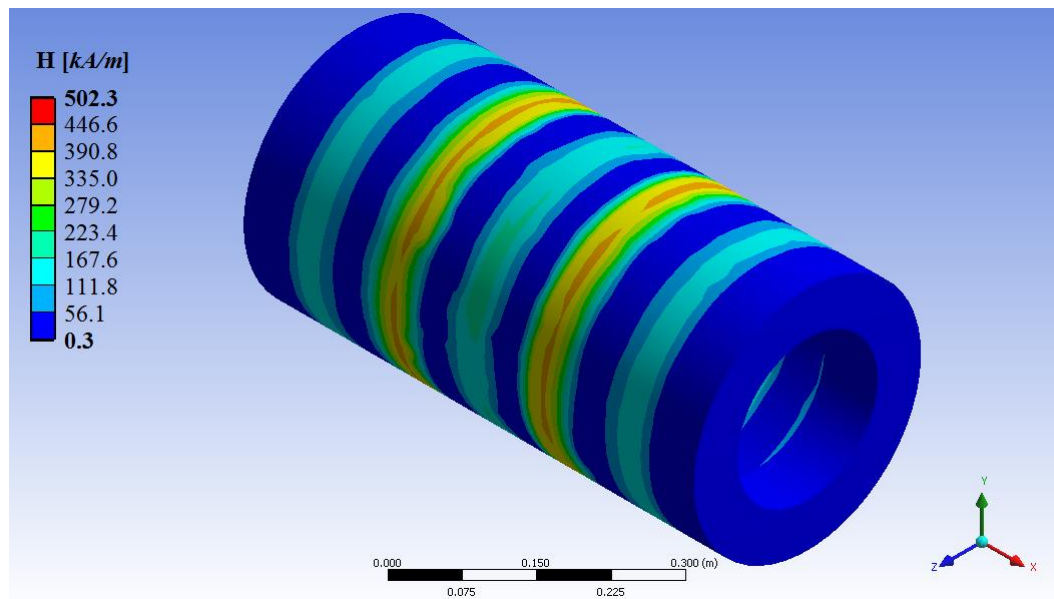


Figure A.II 15. Magnetic field strength, internal winding

Table A.II 14. Controllable force comparison between both models.

Configuration	F_{τ} [ton]
Internal Winding	74.37
External Winding	65.58

Now, when paying attention to the strokes, the external winding configuration has a stroke of ± 200 [mm], which corresponds to the moving capacity of the piston inside the damper. On the other hand, the stroke of the internal winding set up is only ± 90 [mm]. In other words, while the force increases in 13.4%, the stroke decreases in a 55 %.

The second comparative analysis takes our designed configuration and compares it with an internal winding set up having the same stroke, in order to evaluate the

reduction in its total force. The stroke is ± 200 [mm]. To do that, its geometry equals its piston length with the one from our initial configuration. This implies that only one coil can be used. It can be seen in Figure A.II 16, and it consists of a piston (1), a cylinder (2), two steel head plates (3), a coil (4) and two bronze guides (5). The empty space is filled with magneto-rheological fluid.

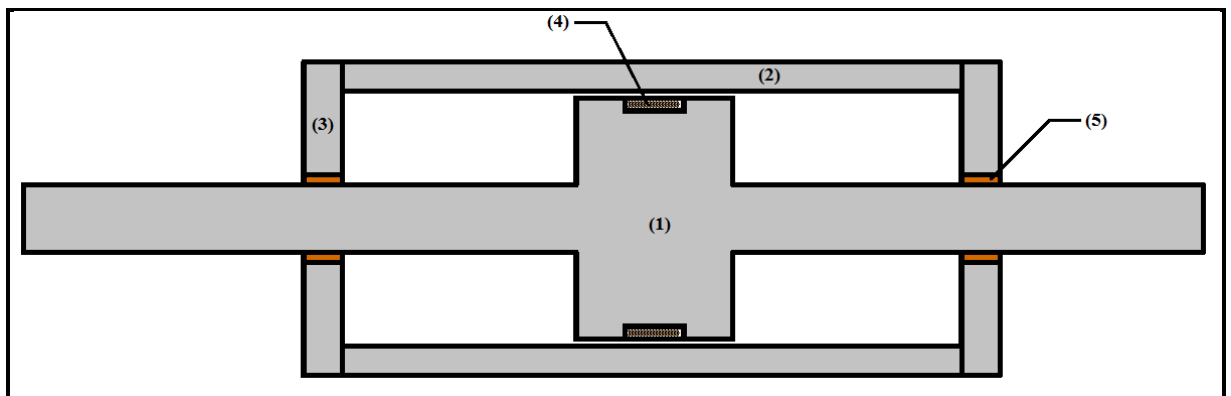


Figure A.II 16. Geometry of the alternative for internal winding with equal stroke

For this configuration, the resultant mesh is composed by 406,361 elements and 614,562 nodes. Boundary conditions are naturally the same as in every model. Magnetic flux density and its path can be seen in Figure A.II 17. The maximum value reaches 1.56 [T] in the steel cylinder, while fluid obtains up to 1.05 [T], which translates into 322 [kA/m] of magnetic field strength (Figure A.II 2). This allows the fluid to achieve its maximum yield stresses, namely 48.32 [kPa].

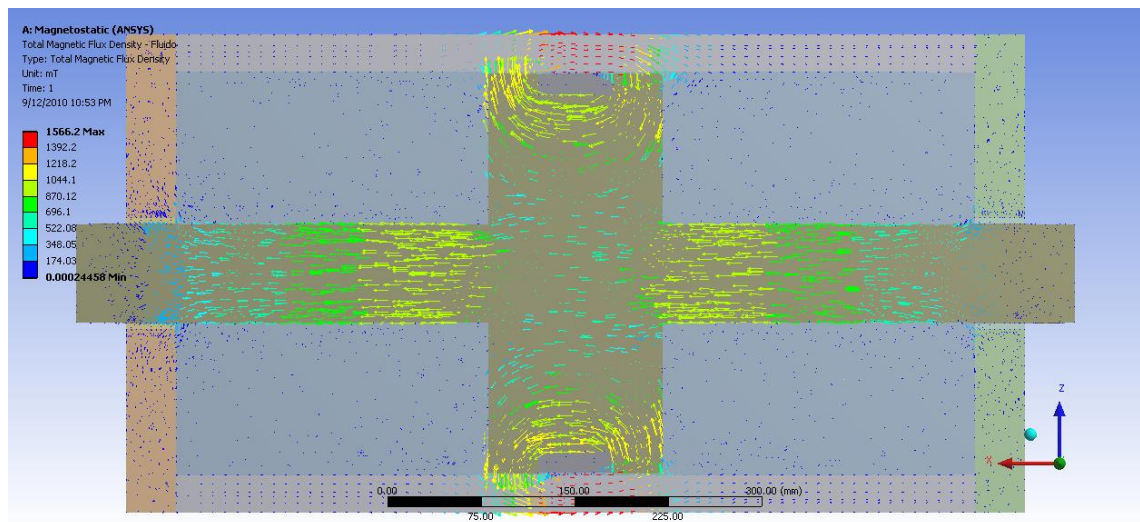


Figure A.II 17. Magnetic flux density, internal winding with equal stroke

After Eq. (7), and taking into account that the only parameters that vary with respect to the last configuration are the active pole length $L = 8$ [cm] and the average fluid yield stress $\bar{\tau}_0 = 36.66$ [kPa], the predicted controllable force is $F_\tau = 23.16$ [ton]. Table A.II 15 presents a comparison between this force and the force obtained for the external winding configuration, which has the same size and stroke. Values exhibit a decrease in a 64.7% of the controllable force.

Table A.II 15. Controllable force comparison between configurations with equal stroke

Configuration	F_τ [ton]
External Winding	65.58
Internal Winding	23.16

Other advantages that the external winding model has over the internal winding configuration are: (i) It is easier to disassemble in case of a modification or maintenance of the electrical circuit is needed; (ii) it simplifies modeling; (iii) the probability of generating a short circuit is reduced; and (iv) less fluid can be used for the same capacity. There is no need to disarm the whole damper, avoiding then possible fluid losses and saving a great amount of time. Electric maintenance, though it is unlikely to be needed, can be done in service location. Modeling gets simplified, because bobbins are not winded around a moving part of the damper, and therefore a dynamic simulation of the magnetic field, which would imply great computational efforts, is not needed. And, since the bobbins do not move, they are unlikely to wear out and, therefore, generate a short circuit, which allows for more time between maintenance periods. Finally less fluid is needed for the same capacity since the external passage for the fluid can be as long as it is needed. In order to increase capacity, the first option must be to extend the length of the external passage and to control the spacing between coils, before attempting to design pistons with greater areas which can result more expensive.

II.6 Odd number of Coils

The analysis of two *Magnetostatic* models, with three and five coils each, is presented in this study. The distribution of the magnetic field strength is obtained and an average yield stress is calculated in order to check if an odd number of coils affects the symmetry of the magnetic field. Both models have the same dimensions than the finally designed configuration except for the steel casing's length, which needs to accommodate to the space occupied by the coils, and it has to be noticed that there is no variation in the coils width and in the spacing between each other. The geometries of these models are compared in Figure A.II 18.

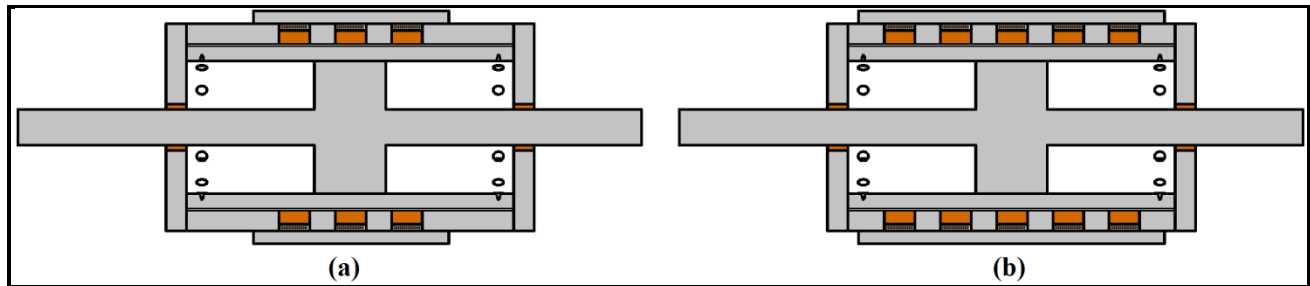


Figure A.II 18. Geometry comparison for both models. (a) Three coils configuration, (b) Five coils configuration

The mesh for both models, which can be seen in Figure A.II 19, is done in the same way as the model presented in chapter 2, with *solid117* Ansys element. For the configuration with three external coils, the mesh consists of 843,891 nodes and 366,986 elements, while the mesh for the damper with five coils has 992,432 nodes and 432,395 elements. Boundary conditions are the same as for every other *Magnetostatic* model.

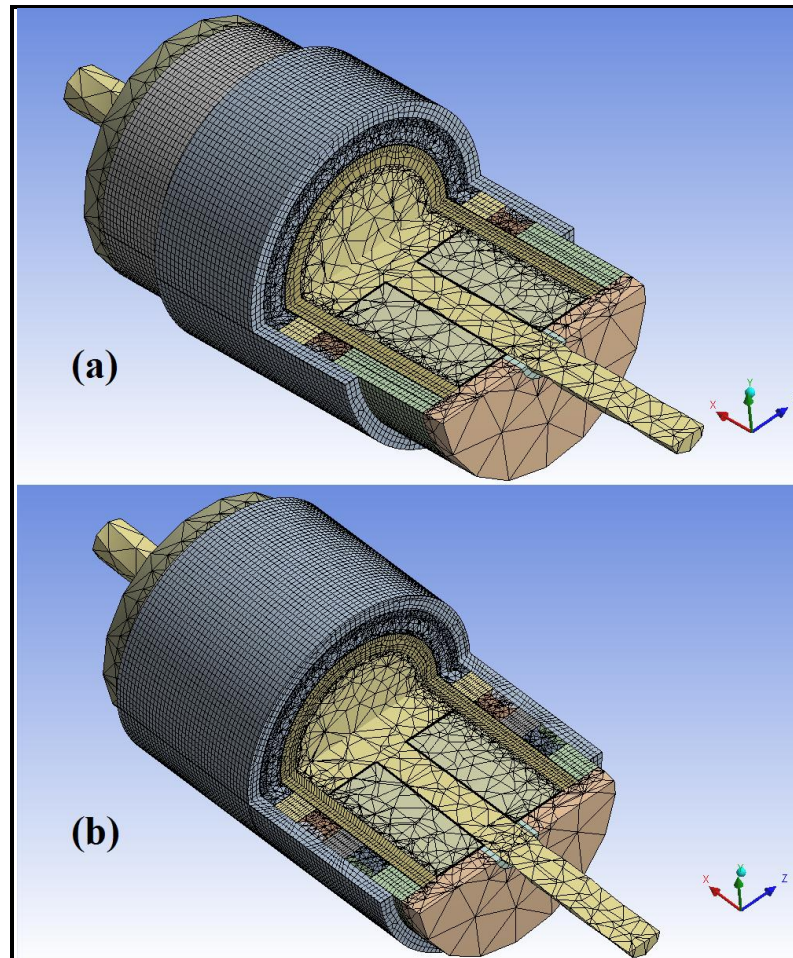


Figure A.II 19. Views of the meshing for the models with an odd number of coils.

(a) Three coils (b) Five coils

Resulting yield stress distribution for both configurations is shown in Figure A.II 20, which have been derived from the magnetic field strength obtained by the *Magnetostatic* models. A trend towards symmetry can be observed, which is clearer for the second model. Maximum value of H is given by 279 [kA/m] (three coils) and 342 [kA/m] (five coils). Maximum yield stress in the first model is obtained at the center, in the region below the steel parts between coils, and it almost reaches saturation. In the

second model maximum yield stress is obtained in the four regions between the coils, and hence they are all saturated.

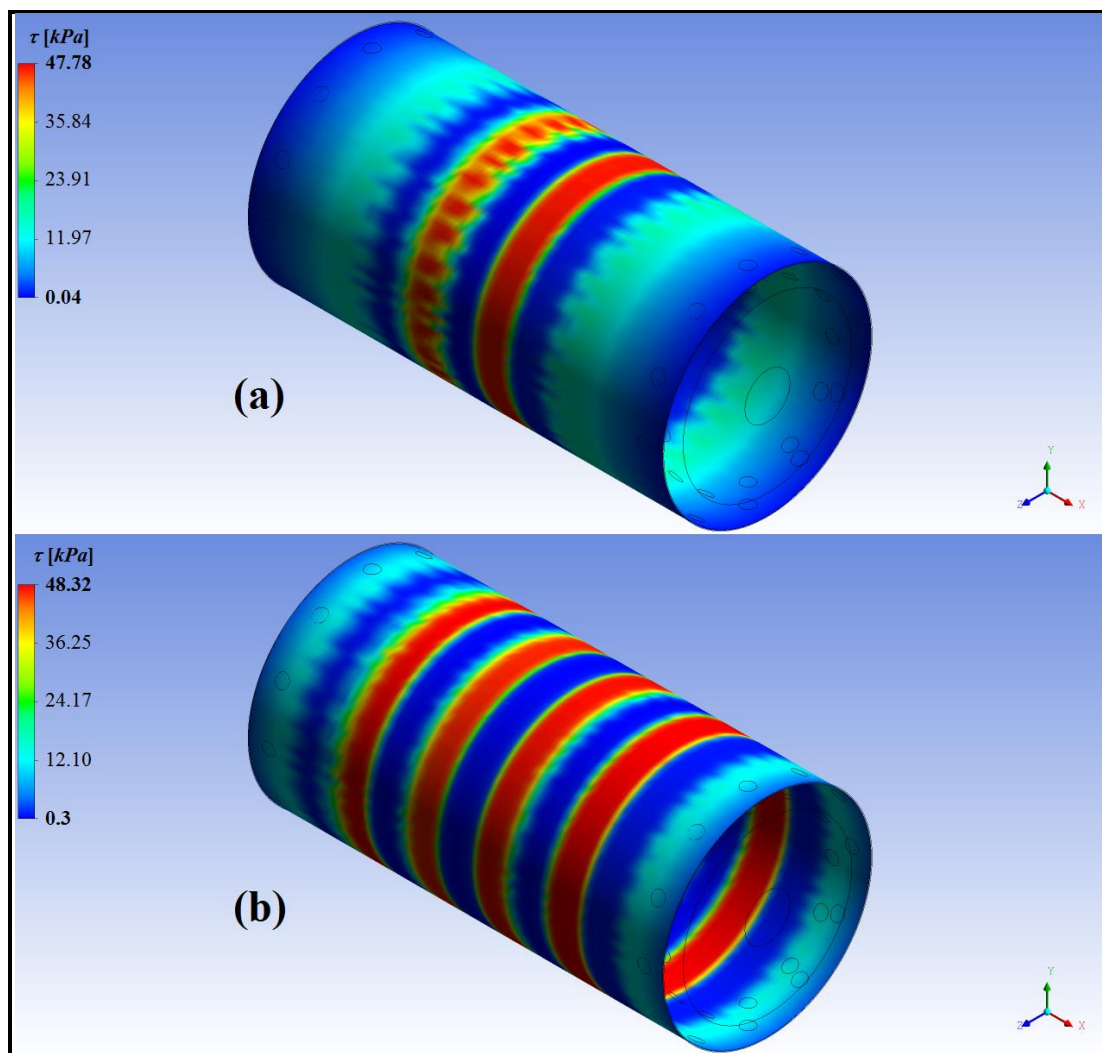


Figure A.II 20. Fluid yield stress, τ_0 . (a) Three coils (b) Five coils

A *CFX* model for each configuration is used for controllable force estimation, following the same method as explained in section 2. Results for both models are shown in Table A.II 16. An average yield stress value has been obtained as well, which is larger in the model with five coils, mainly because of its smaller active pole length, with respect to the other analyzed model. Naturally, the controllable force is also larger, which is an expected result since more coils generate a stronger magnetic field under the same magnetic conditions (number of turns, current intensity and radius of the coils).

Table A.II 16. Summary of results for both models

Stripe Location	Three coils	Five coils
$L[m]$	0.4 [m]	0.28 [m]
$\bar{\tau}_0 [kPa]$	17.75 [kPa]	34.41 [kPa]
$F_\tau (CFX)$	91.98 [ton]	120.37 [ton]

To evaluate symmetry, a percentage-based evaluation is made. For the model with three coils, average values of the stripes in the middle of the domain differ in 9.7%. Border stripes values of τ_0 differ in 11.6%. On the other hand, following the same analysis for the five coils configuration, average yield stresses of middle stripes differ in 2.85% for the middle-left and middle-right stripes and in 7.81% for the second pair of middle stripes. It must be noticed that local maximums are not obtained in center stripes, but in the second group, just as it happens in models with four coils. Values for yield stresses in the border side stripes have a difference of 8.5%. These results show that there is a trend towards symmetry in this model.

II.7 Influence of the radius of a coil in its magnetic field

A parametric analysis of a coil is described herein, where the parameter to be varied corresponds to its radius. The coil has the dimensions of a coil from the damper of *Fujitani* (Fujitani et al., 2001). The objective of this analysis is to prove that the magnetic field depends on the radius of a coil and that, as the radius increases, magnetic field quantities will also increase on the MR fluid domain. Relevant values to be obtained are magnetic flux density \mathbf{B} and magnetic field strength \mathbf{H} .

Therefore, two different models have been done. The first one has a core composed only by steel, and the second has a core that includes both a steel component and magneto-rheological fluid. The geometry of both models can be seen in Figure A.II 21. The first model geometry corresponds to a cylindrical fluid passage with a 2 [mm] gap between the steel core and the steel cylinder. The geometry of the second model is similar to the latter, but its steel core is hollow and filled with MR fluid. This idea is similar to the case of an MR-damper with external coils, where the core is not composed only by steel. When the radius increases its size, the steel core thickness is kept constant. The radius has been varied from 33 to 130 [mm] in both cases.

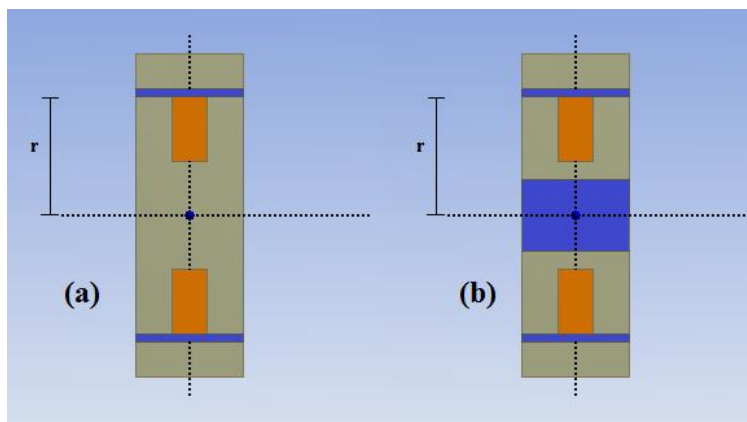


Figure A.II 21 Geometry, (a) Steel core only; (b) Steel + MR fluid core

For each radius value, maximum magnetic flux density in the MR fluid gap domain, $B_{\max,f}$, as well as the maximum value of the magnetic field strength, $H_{\max,f}$, are computed. The output $B_{\max,f}$ for both configurations is shown in Figure A.II 22, where it is clear that it increases as r increases, tending to an asymptote approximately after $r = 100$ [mm].

Field strength $H_{\max,f}$ can be seen in Figure A.II 23. This quantity is directly related with B by the B-H curve given by the manufacturer, and thus the behavior of both variables is similar. It is apparent that the design radius $r_d = 33$ [mm] is not efficient, according to the total force that the damper can develop. The inclusion of the fluid region in the core of the coil does not have a significant influence in our magnetic variables, but it shows an unstable behavior as the radius increases.

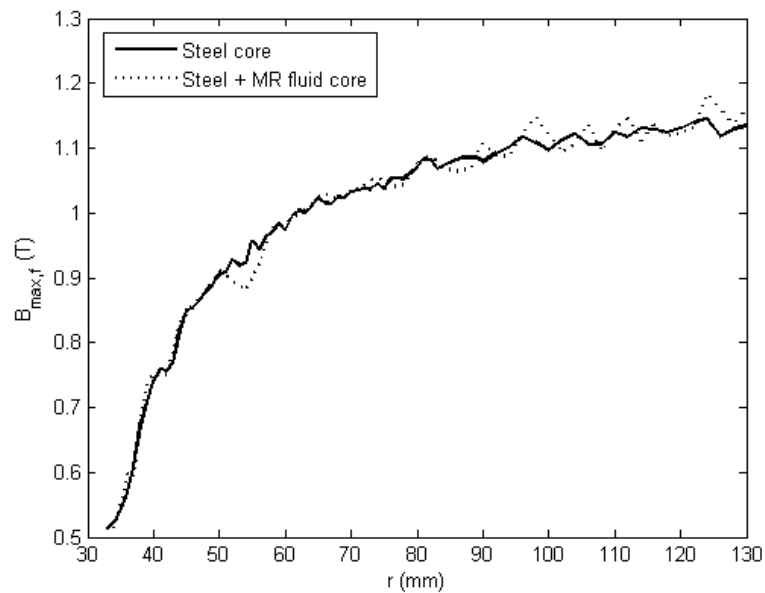


Figure A.II 22. Maximum magnetic flux density in the fluid gap domain

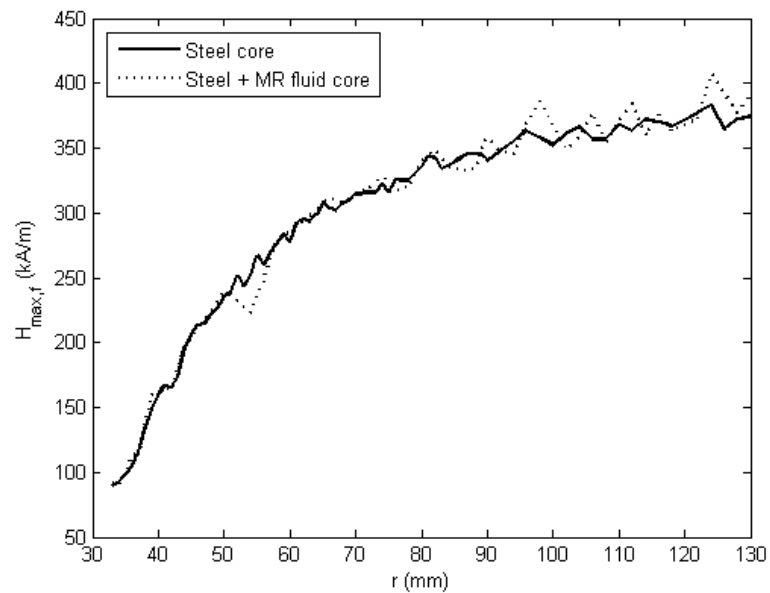


Figure A.II 23. Maximum magnetic field strength in the fluid gap domain, steel core

Magnetic field strength and flux density values have proven to depend on the coil radius. The higher the radius, the larger the controllable force of the damper, limited by an asymptote. Under this concept, *Fujitani's* radius could have been doubled to improve its total force, before the fluid reaches saturation.

APPENDIX III: PARAMETRIC ANALYSES

The variation of four different parameters was done. These parameters are: (i) the spacing between coils b ; (ii) the current intensity i ; (iii) the maximum velocity of the sinusoidal excitation v_0 ; and (iv) the gap size h . The details of each one of the analyses are explained below.

III. 1 Spacing between Coils

The spacing between coils is designated by b and is shown in Figure A.III 1. When b varies, the length of the steel casing that covers the coils, $L_{SL}(b)$, varies too. Every other geometric parameter of the configuration has been kept constant for values of b up to 64 [mm], which is the maximum value that b can take having the cylinders length fixed at 640 [mm], and subtracting the length that involves the lateral holes. For greater values of b , the length of the cylinders must be varied in order to keep the width of the coils, L_b , constant at 60 [mm]. Minimum value chosen for b in this analysis is 45 [mm]. The detail of the parameter values taken into account are summarized in Table A.III 1. The length of the steel layer depends on b following the expression $L_{SL}(b) = 5b + 240$ [mm].

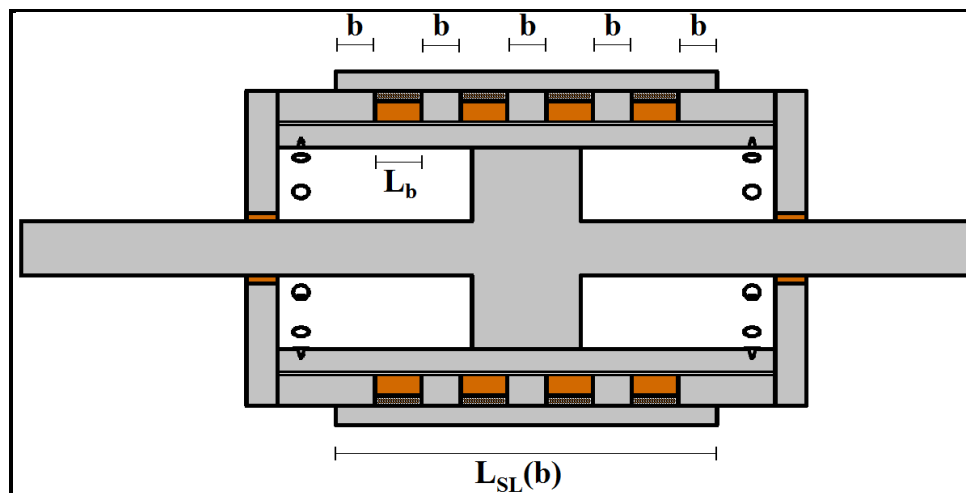
Figure A.III 1. Schematic view of the parameter b

Table A.III 1. Values of each parameter.

Model	1	2	3	4	5	6	7	8	9	10	11
b [mm]	45	46	47	48	49	50	51	52	53	54	55
$L_{SL}(b)$ [mm]	465	470	475	480	485	490	495	500	505	510	515
Model	12	13	14	15	16	17	18	19	20	21	22
b [mm]	56	58	59	60	61	62	63	64	65	70	80
$L_{SL}(b)$ [mm]	520	530	535	540	545	550	555	560	565	590	640
Model	23	24	25	26	27	28	29	30	31	32	33
b [mm]	90	100	110	115	120	130	135	140	150	170	200
$L_{SL}(b)$ [mm]	690	740	790	815	840	890	915	940	990	1090	1240

For each model, magnetic field strength was obtained using *Magnetostatic* application of Ansys 12.0, and exported to Matlab to obtain the yield stress values on the fluid domain. This output is used as an input of a *CFX* model, just as it was explained on Appendix I, and a constitutive relationship F - V for each configuration is

obtained. From this curves, the maximum value is extracted to estimate the controllable force F_τ , which is shown in Figure A.III 2. The value of F_τ increases with the spacing between coils. But it is not as obvious as it seems. As b increases, magnetic field strength values decrease, because the magnetic flux is less concentrated since it has more space to be spread out. A first impression says that this should lead to a decrease on the fluid yield stress, but this does not happen. Lord fluid saturates for strength values above $250 [kA/m]$, which means that the yield stress τ_0 for those values of H corresponds to the maximum value, $48.32 [kPa]$. In every model, this quantity is exceeded in two regions between the coils, thus having maximum yield stress in those zones. Then, even though the values of H do decrease, they do not do it at values under the saturation.

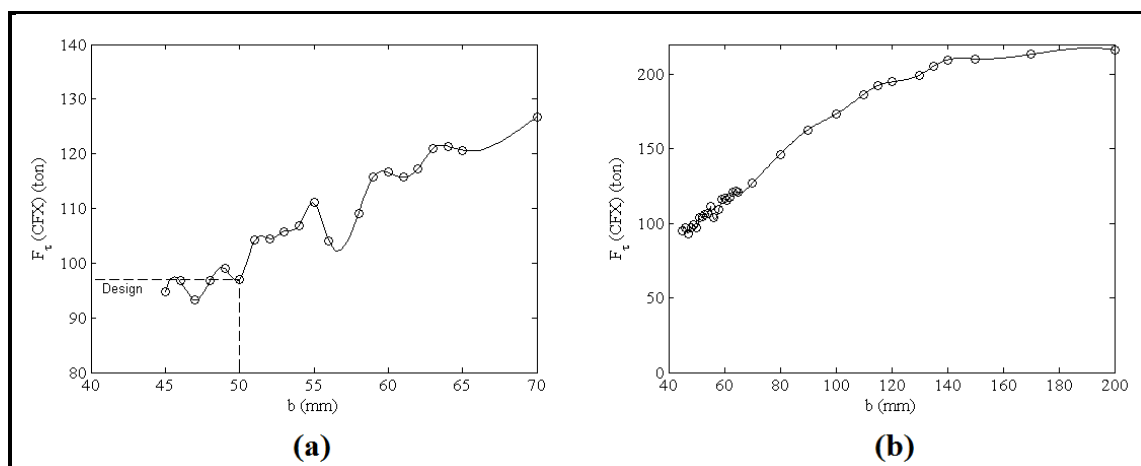


Figure A.III 2. F_t versus b . (a) Interval $b = [45, 70]$; (b) Interval $b = [45, 200]$

III.2 Current Intensity

The objective of this analysis is to study saturation of the fluid. It is expected that it saturates after electric current value of 3[A], which is the designed value. With this analysis, the efficiency of the designed damper can be checked.

Every geometric parameter of the configuration has been kept constant. The only parameter to be varied is the electric current, which takes values from 0 to 6 [A], in intervals of 0.3 [A]. The model of the damper was simulated in *Magnetostatic* application of Ansys 12.0, relating each current value with a determined time-step, using a time interval of 0.01 [s].

As in the previously explained parametric analysis, the Appendix I and in chapter 2, for each time-step, the output of H was obtained and a *CFX* model was performed with $\tau_0(H)$ as an input. Constitutive relationship F - V was obtained for each simulation and the maximum value was extracted as the estimated F_τ . The results are presented in Figure A.III 3. The rate of change of F_τ decreases as the current increases, tending to saturation after 5 [A]. The chosen 3 [A] current intensity can be then raised to 5.1 [A] in order to obtain a F_τ 17.7% higher, but it has a higher power requirement, which cannot be achieved with available power supplies.

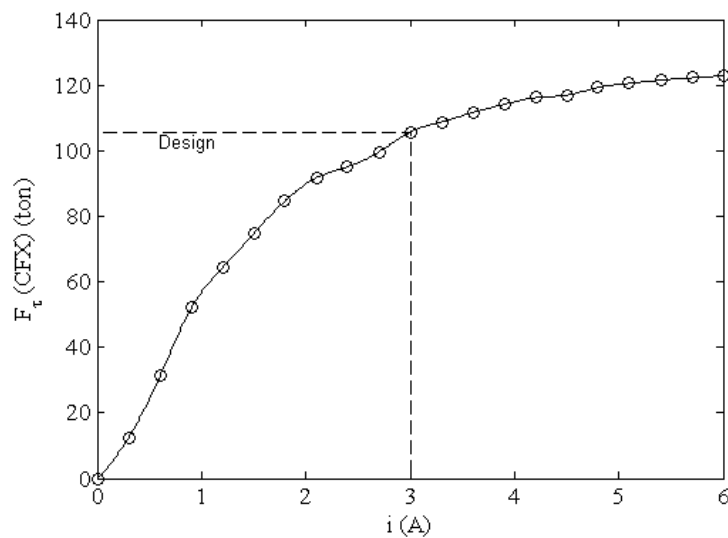


Figure A.III 3. F_τ vs i

III.3 Maximum Velocity

This parametric analysis consists on the simulation of the proposed damper, varying only the maximum velocity of the piston, whose movement is given by:

$$x(t) = x_0(1 - \cos(\omega t)) \quad (13)$$

Therefore, velocity results

$$v(t) = v_0 \sin(\omega t) \quad (14)$$

where $\omega = 10$ [rad/s] and $v_0 = [17, 20, 23, 25, 28, 31, 34, 37, 40, 43, 46]$ [cm/s] are the chosen values for each parameter. The need of this analysis relies on the fact that the

service velocities differ from the velocities that can actually be tested in the laboratory. Therefore, values for v_0 have been chosen taking into account the actuator maximum velocity and service conditions. The *MTS 244.15 Hydraulic Actuator* can reach a maximum velocity of 17 [cm/s]. In service, the worst condition predicts a maximum velocity of 46 [cm/s].

Instead of actually move the piston, a sinusoidal flow is imposed as an input, as explained in the Appendix I, with the velocity profile given by Eq. (2) at the inlet of the domain. The reason behind choosing the frequency at 10 [rad/s] is that the greater the frequency, the shorter the period and then, the shorter the computational time required for the simulation. It has been assumed that maximum capacity of the damper does not depend on frequency in this range, since it actually depends on the maximum velocity, which is a combination of displacement amplitude and frequency.

The *CFX* application of Ansys 12.1 was used. For each model, F - V curves are obtained and their maximum value is compared, in order to see how the maximum velocity affects the damper's capacity. In this analysis, as well as in the previous analysis, F - V curves have been approximated by a regression because of the 'noise' given by convergence issues. This noise occurs when the time-step is not small enough. In this particular case, a time-step of 1×10^{-4} [s] has been used. A time-step of 1×10^{-6} [s] would eliminate the noise, but it has an enormous computational cost. This regression is explained and justified in the chapter *Fitting curves for CFX Output* from Appendix I.

Maximum force obtained in the simulations, after the regression, can be seen in Figure A.III 4 for each maximum velocity of the sinusoidal excitation, v_0 . The maximum force increases linearly, but not significantly, with a rate of change of 0.91 [ton·s/cm].

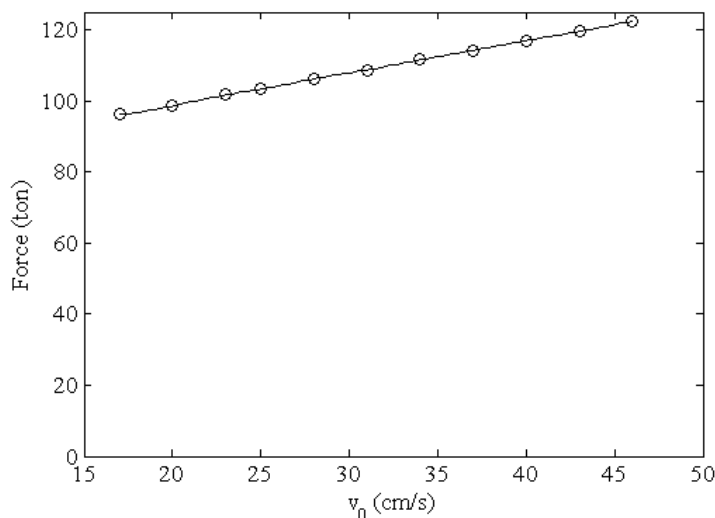


Figure A.III 4. Maximum force obtained for each model, after the linear fitting

It can be concluded that the maximum force of the damper F_τ increases with the maximum velocity of the excitation. This dependence is practically linear and it is not really significant for design purposes. This means that, having only two maximum velocities modeled to obtain a design force value, capacities for any other maximum velocity value can be fairly obtained by linear interpolation.

III.4 Gap Size

The gap size is a relevant variable when calculating the dynamic range D in a typical magneto-rheological damper, because it directly affects the viscous force F_η . In our case, F_η is also affected by the 24 holes in the internal cylinder. The objective of this analysis is then to identify the behavior of the dynamic range and the total capacity of the damper by varying only the gap size. Values taken for the gap size are: $h =$

0.9: 0.1: 5 [mm]. This parameter can be seen in Figure A.III 5, along with the modeled geometry.

This analysis is done as follows. In a first step, the magnetic field for each of the models is calculated by using Ansys 12.1 *Magnetostatic* application. Then the results are processed in Matlab and the controllable force F_z is obtained with Yang's formula. Yang's formula is used since a change in the gap implies a change in the mesh, i.e. for every model a new mesh to the *CFX* model must be developed, which consumes great computational time. Viscous force can be obtained with a *CFX* model, since it does not need a refined mesh.

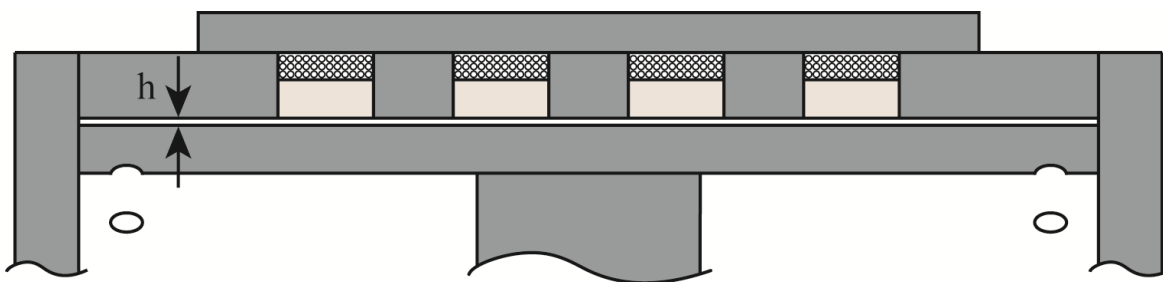


Figure A.III 5. Geometry modeled for maximum velocity analysis

The *Magnetostatic* model was done in the same way as explained in Appendix I, but adding the ability of the software for including parameter analyses. The gap size is then parameterized and the magnetic analysis is done for each of the values that it takes. Results are exported to '.xlsx' files and processed using Matlab, where the controllable force is obtained. On the other hand, an Ansys 12.1 *CFX* model for obtaining F_η is done in the same way as explained in the mentioned appendix, for each value of h , and applying the linear fitting scheme. Again, this analysis is done with the parametric option of Ansys Workbench. The output of these models is exported to a '.txt' file and

read in Matlab, where the maximum value of the viscous force for each value of h is extracted, so F_η and D can be obtained.

When looking at Yang's formula for the controllable force F_τ it is clear that, if every other parameter is kept constant, F_τ diminishes when the gap size increases, although not linearly. In this case, every other parameter is kept constant except for the yield stress representing the active pole length, τ_0 . Therefore it is interesting to see how it changes when changing the gap size before analyzing what happens with F_τ , which is shown in Figure A.III 6. The yield stress in the fluid decreases almost linearly as the gap increases its size. Then, no assumption can be made about the behavior of the controllable force. Since gap values rarely exceed 2 [mm] there is no need to worry about the behavior of F_τ after that value. The design value for τ_0 is 23.42 [kPa].

Now, keeping into account that the diameter of the holes in the internal cylinder has been kept constant through this process, the viscous force, depending only on the gap size, has been evaluated using Ansys 12.1 CFX software. Its maximum value related to h is shown on Figure A.III 7, where can be deducted that both F_η decreases as h increases, approaching to an asymptote, and tending to infinity as h decreases. Design value for F_η is 3.75 [ton].

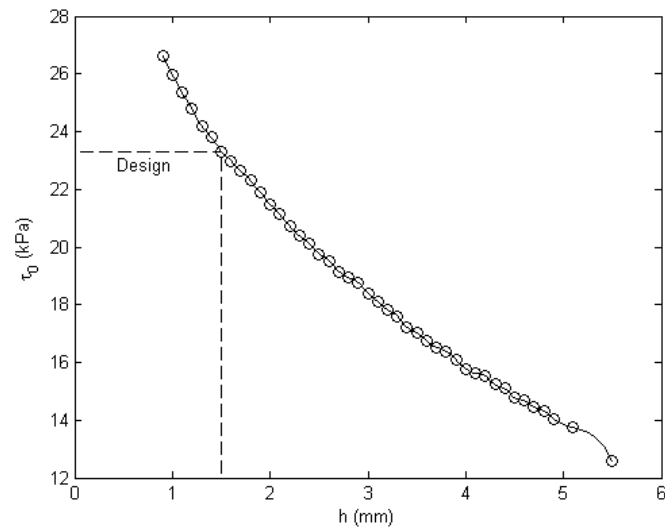


Figure A.III 6. Representative average yield stress τ_{av} in the fluid gap domain versus the gap size

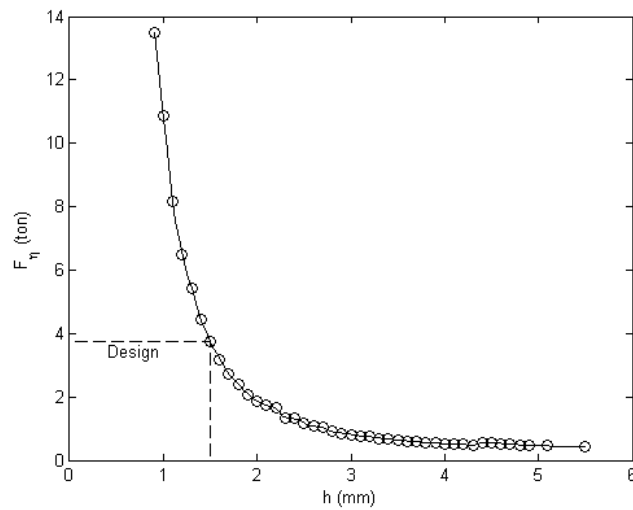


Figure A.III 7. Viscous force vs gap size, obtained with Ansys 12.1 *CFX* software

The dynamic range is then obtained by simply dividing F_τ by F_η , and its outcome is presented in Figure A.III 8. There is a maximum for a value of h above the expected. Maximum dynamic range $D_{max} = 29.22$ is obtained when $h=3.1$ [mm], but the value of the controllable force when it occurs is 22.25 [ton], which is not satisfactory with our design. The dynamic range considering our design parameters ($h = 1.5$ [mm]) is $D_{design} = 17.4$.

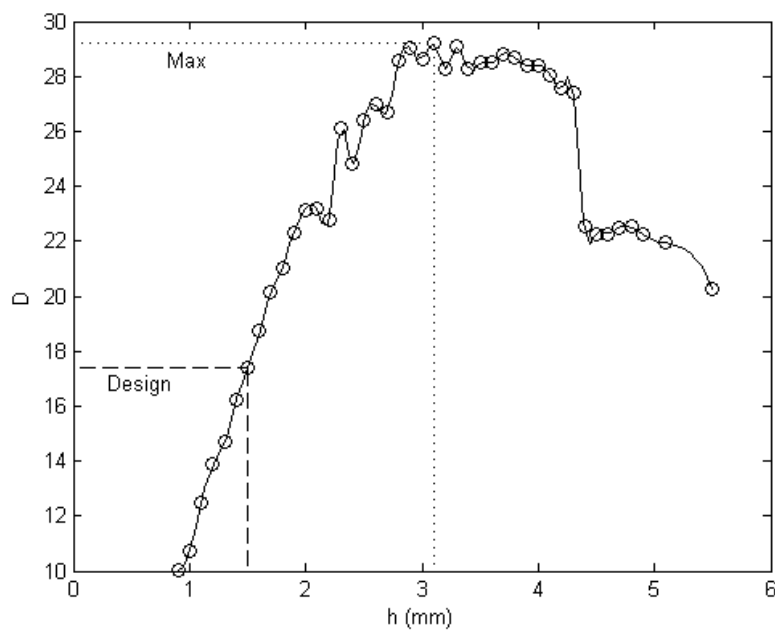


Figure A.III 8. Dynamic range vs gap size